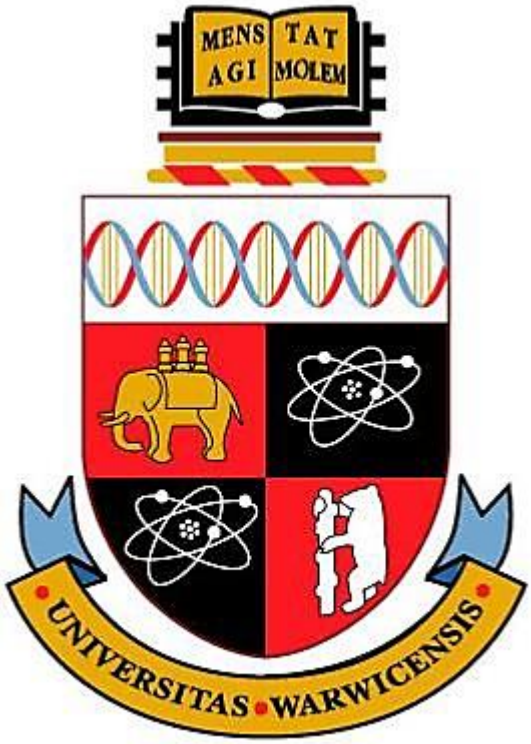

An experimental study on the entry of spheres into a two-layer system of immiscible liquids

BENEDICT CHUAN-WEI TAN

A thesis submitted in partial fulfilment of the requirements for the degree of Doctor of Philosophy in Engineering

April 2016

School of Engineering

University of Warwick

To God Be The Glory!

Table of Contents

Table of Figures

Acknowledgement

I would like to express my deepest gratitude to the Almighty God and to our Lord Jesus Christ for the completion of this doctoral research and thesis.

I would also like to express my sincere gratitude to the School of Engineering for the Departmental Scholarship, to my supervisor Prof. Peter J. Thomas and also to all whom God has through His Grace, provided to assist me during my doctoral studies.

To the Almighty God and to our Lord and Saviour Jesus Christ be all Glory now and for ever. Amen.

Declaration

This thesis is submitted to the University of Warwick in support of my application for the degree of Doctor of Philosophy. It has been composed by myself and has not been submitted in any previous application for any degree.

The work presented (including data generated and data analysis) was carried out by the author and the following is a list of publications that have arisen from the work of this thesis as of April 2016:

Journal paper:

- **B. C.-W. Tan**, J. H. A. Vlaskamp, P. Denissenko and P. J. Thomas, 'Cavity formation in the wake of falling spheres submerging into a stratified two-layer system of immiscible liquids', *J. Fluid Mech.* **790**, 33-56 (2016)

Conference papers:

- **B. C.-W. Tan**, J. H. A. Vlaskamp and P. J. Thomas, 'The entry of steel spheres into a stratified two-layer system of immiscible liquids', Book of Abstracts of 58th British Applied Mathematics Colloquium, University of Oxford, UK, Pg. 140 (2016)
- **B. C.-W. Tan**, J. H. A. Vlaskamp, P. Denissenko and P. J. Thomas, 'New phenomena observed following the entry of rigid spheres into a two-layer system of immiscible liquids', Book of Abstracts of XXXV Dynamics Days Europe 2015, University of Exeter, UK, Pg. 203 (2015)
- **B. C.-W. Tan** and P. J. Thomas, 'Cavity formation behind steel spheres impinging on a two-layer stratified system of immiscible liquids', Book of Abstracts of 4th Joint British Mathematical Colloquium & British Applied Mathematics Colloquium, University of Cambridge, UK, Pg. 73 (2015)

Abstract

The phenomena, cavity formations and dynamics associated with rigid spheres entering into stratified, two-layer, oil-water systems were experimentally studied. The results were compared with available data for the corresponding type of cavities formed by spheres entering into single-phase, homogeneous liquids. The discussion and data analysis showed that the oil coating acquired by the spheres while passing through the oil layer, significantly modified the qualitative and quantitative aspects of the dynamics associated with cavity formation. In particular, ripple-like structures were discovered forming along the cavity walls, and such phenomenon was not known to exist when spheres entered into homogeneous liquids. The data analysis also showed that the ripples formed as a result of a two-dimensional instability, arising due to the shear between the oil layer coating the spheres and the surrounding water. Meanwhile, phenomena not consistent with present understanding were observed during entries of steel spheres into sunflower oil and the two-layer, sunflower oil-water system. Further experiments suggested that such phenomena arose as a result of the surface conditions of the spheres, thereby highlighting the substantial influence the surface conditions of a body could potentially have on cavity dynamics.

Chapter 1: Introduction

''In the beginning was the Word, and the Word was with God, and the Word was God.''

------ St John 1:1, KJV

1.1. Motivation

The entries of solid bodies into water and their associated phenomena have fascinated mankind over the centuries. During these entries, well-known and characteristic splash patterns are generated by the impacting body while complex flow structures will develop in the wake of the same body after it is fully submerged in water.

Modern systematic and scientific studies on liquid entries by solid bodies originate from the pioneering studies of Prof. A. M. Worthington in the 19th century [1-3]. The fundamental nature and wide application of the subject in addition to its importance, benefits and potential to the military have led to extensive studies up to this very day. Meanwhile, water and sphere have remained the most popular and widely used liquid and solid body, respectively due to the relative ease of modelling them and their wide availability.

In the classic scenario, a solid body that possesses sufficient velocity will generate a significant cavity at its wake as it enters into a pool of liquid. This cavity will initially expand and thenceforth collapses rapidly, resulting in remarkable phenomena such as the ejection of a liquid jet and the production of a 'pop' sound. Due to the popularity of the subject and over a century of scientific investigations, the

cavity and impact dynamics associated with solid bodies entering single-phase and homogeneous liquids have already been widely documented and well understood.

However, a review of the literature available at the point of writing reveals that the same level of knowledge and understanding is not present for corresponding studies that involve entries of solid bodies into stratified, two-layer systems of immiscible liquids. Meanwhile, the stilling of water waves by means of pouring in small quantities of oil was observed by Benjamin Franklin [5] in the 18^{th} century. Franklin's observation has shown the potentially significant influence an oil layer can have on the dynamics of the water directly underneath it. Hence the potential of an entire new area of research has become the motivation for the scientific studies of this thesis.

1.2. Objectives

In this thesis, the phenomena, cavity formations and dynamics associated with rigid spheres entering into two-layer, oil-water systems were experimentally studied. The oil-water system comprised of a relatively thin oil layer resting on the surface of a deep pool of water.

The results obtained in the experiments will be analysed and compared with corresponding results from single-phase, homogeneous liquids that are available at the point of writing. In addition, unique phenomena observed during the experiments will be identified and quantified while provision of reasonable hypothesis for their occurrence will also be endeavoured.

1.3. Main discoveries in the thesis

The experimental investigations documented in this thesis revealed the occurrence of unique phenomena that are neither previously observed nor known to exist during entries of solid bodies into single-phase and homogeneous liquids. The main example is the formation of ripple-like structures along the otherwise smooth cavity walls at the wake of the rigid spheres. In total, four general distinct phenomena that can arise subsequent to rigid spheres entering into two-layer liquid systems have been identified and classified. Meanwhile, it has also been found that the presence of an oil layer will have significant influence on both the dynamics of cavity sealing and the drag experienced by the spheres.

In addition to the main discoveries, phenomena not consistent with present understanding were observed subsequent to steel spheres entering into sunflower oil and the two-layer, sunflower oil-water system. These phenomena highlight the substantial influences that both the surface conditions of a body and the upper layer liquid in a two-layer liquid system can potentially have on cavity dynamics.

1.4. Organisation of the thesis

Chapter 2 will review present literature on liquid entries by solid bodies. These include the pioneering works of Worthington, early experimental investigations done by others after him and the observations and results obtained by scientists in the late 20^{th} and early 21^{st} centuries.

Chapter 3 presents the general set-up for the experimental investigations of this thesis. The equipment and conditions during these investigations will also be described in details.

Chapter 4 classifies and describes the four general phenomena that can potentially arise subsequent to rigid spheres entering and submerging in stratified two-layer systems of immiscible liquids. The conditions required by the impacting spheres to generate each phenomenon will also be studied.

Chapter 5 presents the observation of unusual phenomena that are not consistent with the present literature and current understandings. These phenomena were observed subsequent to steel spheres entering into a deep pool of sunflower oil and the two-layer, sunflower oil-water system.

In Chapters 6 and 7, the dynamics of the spheres and their associated cavities after entries into two-layer systems of immiscible liquids will be studied. The results will be compared with corresponding data for sphere entries into water that are available from the present literature. This procedure will highlight the influence that a thin viscous oil layer has on the dynamics associated with solid-liquid impacts.

Chapter 8 provides a systematic study on the dynamics and origin of the unique ripple-like structures that form along the cavity walls at the wakes of the spheres. In particular, the growth of these ripples will be measured and analysed.

Chapter 9 will present a conclusion for the experimental investigations of this thesis.

Chapter 2: Literature Review

''The fear of the LORD is the beginning of knowledge.....''

------ Proverbs 1:7, KJV

2.1. Worthington's pioneering studies

Prof. Arthur Mason Worthington, CB, FRS (1852-1916) is credited as being the pioneer of modern systematic and scientific studies of impacts on liquid surfaces by both solid bodies and liquid drops. His experimental works were published as early as 1882 [1]. For reasons of historical interest, examples of his sketches that present the shapes of splashes and cavities formed from solid-liquid impacts are being shown in Figures 1 to 3.

As illustrated in the three figures, Worthington discovered and highlighted that the magnitude of the disturbance created on the liquid surface was dependent on the surface conditions of the impacting solid sphere. He observed that despite having the same impact velocity, a polished and perfectly dry sphere caused only slight disturbances upon the liquid surface in contrast to the relatively larger and more violent disturbances generated by its rough or wet counterparts. This observation would be mentioned again in his later studies [2-4] and investigated seventy years later by May [8].

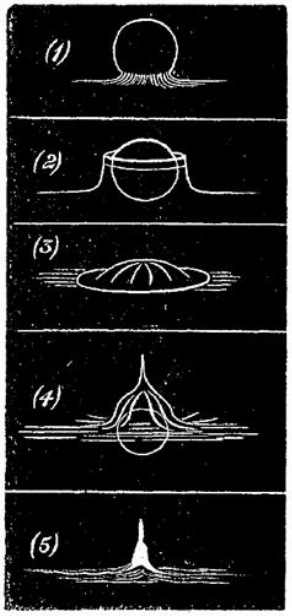

Figure 1: Sketches from Worthington [1] illustrating the phenomenon following the water entry of a polished marble sphere with a diameter of 1.28cm and a drop height of 62cm.

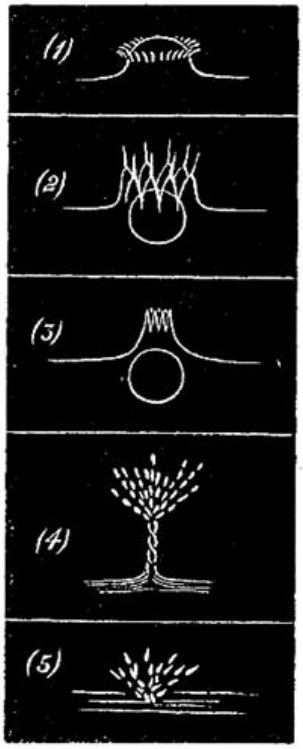

Figure 2: Sketches from Worthington [1] illustrating the phenomenon following water entry of a marble sphere with same dimensions and impact velocity as shown in Figure 1 but with an imperfect drying or polishing of the sphere.

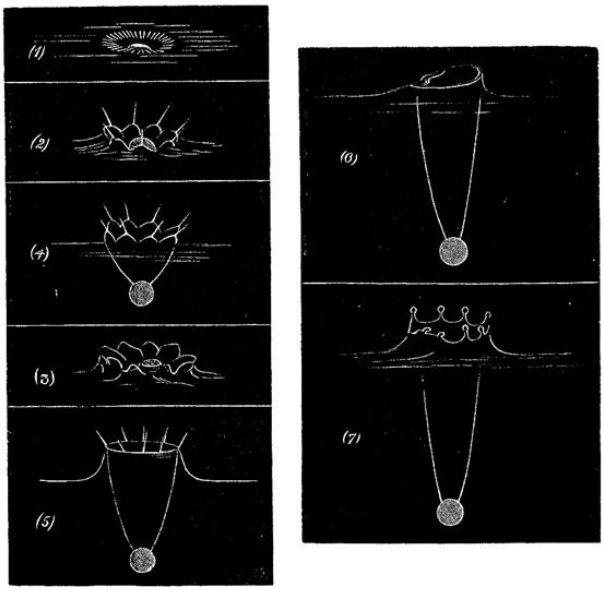

Figure 3: Sketches from Worthington [1] illustrating the phenomenon following water entry of a marble sphere with same dimensions and impact velocity as Figure 1 but the sphere was being roughened with sand paper or left wet.

The principal reason causing the differences in disturbances and splashes is the generation of air cavities at the wake of the impinging body as it submerges in the liquid. Whereas the rough or wet spheres (Figure 3) generated a cavity at its wake, little or no such cavity was observed to be formed behind the polished or dry spheres (Figures 1 and 2). Cavity generation is dependent on the rate of wetting of the submerging body, hence a polished or dry sphere wets more rapidly than its rough or wet counterparts. As shown in Figures 1 and 2, the water quickly enveloped the spheres and reached their apexes, forming upward jets in contrast to that shown in Figure 3 where the sphere did not wet completely.

In addition, Worthington also noted the existence of a transition velocity between the two types of disturbances and splashes (Figures 2 and 3). This transition velocity itself is also dependent on the surface conditions of the impacting body and its value will be different for bodies that have different rates of wetting. Hence even a

very well-polished, dry and clean sphere will generate a cavity at its wake should its impact velocity exceed its transition velocity. It can also be concluded from Figures 1 to 3 that the transition velocity of a smooth sphere is higher than that of its rough counterpart despite both spheres being made of the same material and having the same dimensions while falling into the same type of liquid.

More than a decade later, with the aid of instantaneous photography, Worthington succeeded in obtaining the first high-speed photographs of the impact dynamics associated with both liquid droplets and solid spheres [2]. Thus he was able to study the formations of cavities and jets subsequent to such impacts with high visual accuracy, providing many pioneering photographs in the subject [2-4]. Examples of his early photographs are shown in Figures 4 to 6. Meanwhile, his discovery and studies of the jet that emerges from the liquid surface following impact has led to it being named ‘Worthington jet’ in his honour. A picture of a Worthington jet taken by Worthington himself is shown in Figure 7.

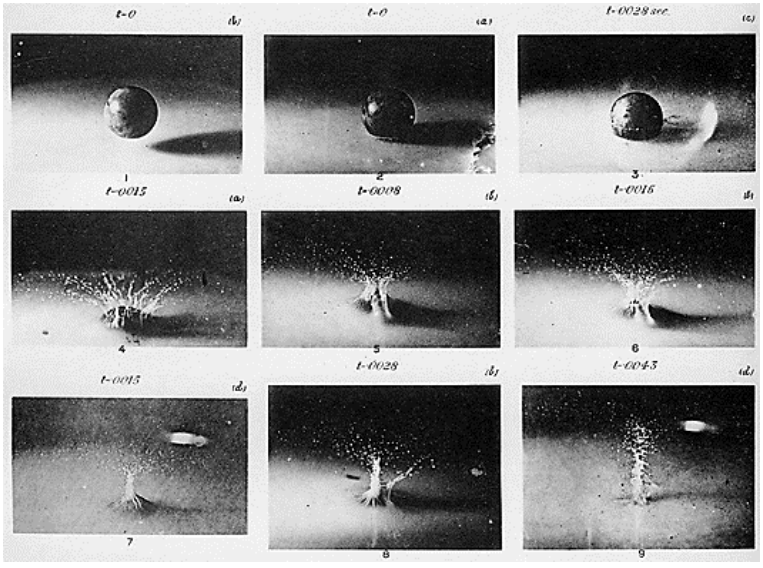

Figure 4: Figure from Worthington & Cole [2] which shows splashes following the entry of a well-polished ivory sphere with diameter of 1.9cm and dropping from a height of 60cm into water mixed with milk. This is very similar to the sketches shown in Figures 1 and 2 [1].

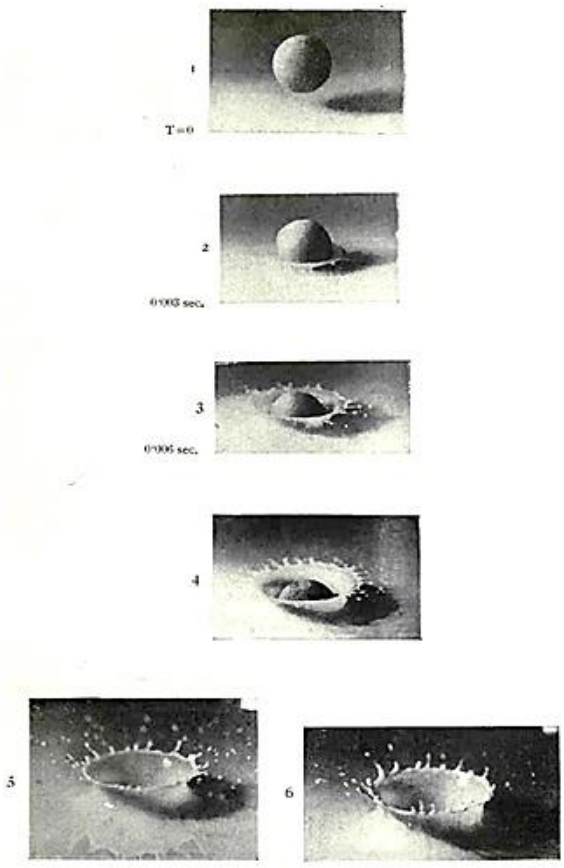

Figure 5: Figure from Worthington [4] which shows the splash following the water entry of a rough sphere of diameter 1.5cm and dropped from a height of 15cm. Milk had been added into water for clearness in the photographs. This is very similar to the sketches of Figure 3 [1].

Figure 6: Figure from Worthington [4] which shows the cavity formation at the wake of a rough sphere following its water entry. The sphere had a diameter of 1.5cm and was released from a height of 15cm.

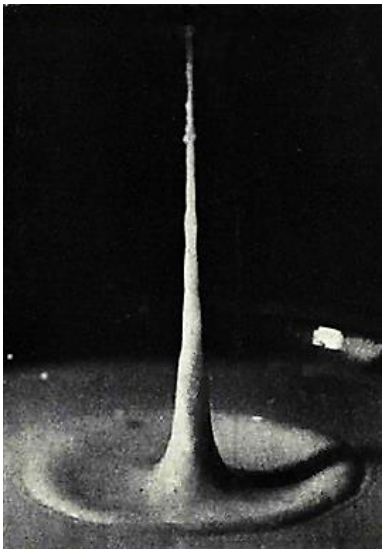

Figure 7: Figure from Worthington [4] which shows the formation of Worthington jet after water entry of a rough sphere. The water had been mixed with milk.

Worthington also conducted and described further experiments identifying the influences of for instance, liquid nature, temperature, the presence of a flame and the presence dust had on the impact dynamics and the aforementioned transition velocity [3]. The pioneering photographs contained in all his studies together with his publication *A Study of Splashes* [4] remain the foundation of modern studies in the subject.

2.2. Early studies following Worthington's works

In the years that followed Worthington's works, Mallock [6] and Bell [52] provided some qualitative explanation for cavity shapes and sphere motions in the liquid. Mallock [6] deduced a simple mathematical theory of the cavity shape at any given time. However, according to Bell [52], Mallock's theory did not exactly match experimental results as he had not taken into account certain contributing factors such as the surface tension of the liquid. Meanwhile, Bell [52] himself conducted further

experiments and showed that the cavity shape was also dependent on the viscosity of the liquid.

Interests in the subject resumed during and after the Second World War when its potential importance and benefits to the military were being appreciated and explored. May, while working for the Naval Ordnance Laboratory in the USA, conducted a series of research involving the entries of projectiles (which he called missiles) into water during the 1950s [8-10]. He further explored the effects of surface conditions on splashes and cavity formations subsequent to solid-liquid impacts [8] that were first noticed and documented by Worthington more than half a century previously [1-4]. In addition, May also experimentally studied the virtual mass of a sphere in water [9], the generations of different types of cavity closures following entries of solid spheres into water [10] and the motion of the cavity wall [10].

Similar works had also been done by Gilbarg & Anderson [11], Birkhoff & Caywood [12] and Richardson [13] during the same period. Gilbarg & Anderson [11] explored the influence of atmospheric pressure on cavity formations and phenomena associated with water entry by spheres while Birkhoff & Caywood [12] presented a new photographic technique for observing velocity fields in water, induced by the entry of solid missiles. In England, Richardson [13] did a mathematical study on the impact of a solid on a liquid surface where the shape of the air cavity formed was explained in terms of potential flow. Richardson [13] also measured the resistance experienced by spheres moving in liquids and found that the values of drag coefficient, C_D for spheres with cavities '*are less than those commonly associated with fully immersed spheres*' at the same values of Reynolds number.

The decrease in pressure within the cavity prior to its surface closure was also a subject of interest. Abelson [14] showed from his experiments that the pressure drop was much higher than the frequently stated assumption of his time, $p=\frac{1}{2}\rho_a u_i^2$ (where ρ_a and u_i are the air density and projectile impact velocity respectively). Abelson [14] further demonstrated that the entry angle of the projectile had an impact on the total pressure drop while the minimum cavity pressure will decrease linearly with increases in impact velocities.

2.3. Contemporary studies

The advances in science and technology enable modern scientists and engineers to study the dynamics associated with solid-liquid impacts both computationally and experimentally with ever greater details and accuracy. Modern state-of-the-art visualisations showing details of the developing flow patterns and reviews of existing literature on the subject are contained in, for instance, Truscott & Techet [15, 16], Truscott *et al.* [17, 18], Thoroddsen *et al.* [19], Thoroddsen [20] and Aristoff & Bush [21].

Meanwhile, computational studies can be found in, for instance, Howison *et al.* [22], Lee *et al.* [23], Gekle *et al.* [24-27], Gordillo & Gekle [28] and Peters *et al.* [29]. The usage of visualisation experiments with smoke particles and multiscale simulations by Gekle *et al.* [26] has shown that high speed air jets that have the potential to reach supersonic speeds can be ejected from cavities that are formed from solid-liquid impacts.

Investigations of the influences of surface conditions on cavity formations by solid bodies submerging in water previously highlighted by Worthington [1-4] and studied by May [8], have continued to be experimentally studied to this day. In recent

works, these impacting solid bodies were commonly classified as either hydrophilic or hydrophobic [15-19, 30-33]. The hydrophilicity or hydrophobicity of a body is determined by its surface wettability or wetting angle. It is understood from Duclaux *et al.* [30] that minimal difference exists between the shapes of cavities formed behind similar hydrophilic and hydrophobic spheres should their impact velocities exceed their respective transition velocities.

Impacts involving solid bodies striking granular materials will generate phenomena that have identical features to those observed following solid-liquid impacts. The similarities can be seen in the existence of a void collapse and the formation of a granular jet [34, 35] that resembles the Worthington jet mentioned earlier and shown in Figure 7.

Despite the popularity of spheres, objects such as disks [24-27, 36-39] and cylinders [30, 32] were also being used. In addition, cavity and impact dynamics involving Leidenfrost spheres (spheres that have temperatures higher than the boiling point of the liquid in which they are submerging) [40] , viscous liquids [41] and non-newtonian liquids such as a viscoelastic miscellar fluid mentioned by Akers *et al.* [42] were also studied.

Marston *et al.* [40] observed that following liquid entry by a Leidenfrost sphere, a vapour layer will envelop the sphere, preventing any physical contact between the sphere and the liquid. Hence a non-wetting scenario will be generated which in turn results in the production of very smooth cavity walls.

Meanwhile, it is also worth noting that it is possible for non-axisymmetric impacts to create cavities of ‘interesting’ shapes. Enriquez *et al.* [37, 38] presented

pictures showing pineapple-shaped cavities created by a round disc with a superimposed mode-20 azimuthal disturbance.

2.4. Conditions for cavity formations

Both Worthington [1-4] and May [8] have noted that water entry of solid bodies do not necessarily result in cavity formation. According to Truscott *et al.* [17], the key parameters affecting the dynamics associated with water entry are the geometry (characterised by maximum diameter, D), wettability (characterised by wetting angle, θ), density ρ_s, location of the centre of mass, impact velocity u_i, impact angle α_o and the spin or rotation Ω of the solid body in question.

From these parameters, Truscott *et al.* [17] formed the capillary number, $Ca=\mu u_i/\sigma$ where μ and σ are the dynamic viscosity and surface tension of water respectively. They concluded that the formation of cavity will be determined by the capillary number, wetting angle and the geometry of the impacting body.

Meanwhile, a solid body submerging in water is considered to be hydrophilic when $\theta < 90^o$ and is hydrophobic when $\theta > 90^o$. A reference to the illustration shown in Figure 2 (d) of Truscott *et al.* [17] shows the water clinging more readily to the hydrophilic surface, resulting in a higher rate of wetting compared to the hydrophobic surface. In the case where the rate of wetting is sufficiently high, the water will reach the apex of the body, completely preventing the formation of an air cavity as shown by the sketches from Worthington [1] and presented as Figures 1 and 2 in this thesis.

Truscott *et al.* [17] also presented a regime diagram which summarised the relationship between the capillary number and the wetting angle in relation to cavity formation during water entry by a sphere. The critical capillary number marks the

transition between spheres with and without cavity generation. According to Truscott *et al.* [17], the critical capillary number and consequently the transition velocity will remain constant for any hydrophilicity in the range $0^o \leq \theta < 90^o$ and become a decreasing function of θ when the sphere was hydrophobic ($\theta > 90^o$). Towards the extreme end, a superhydrphobic sphere ($\theta = 180^o$) will generate a cavity at any impact velocity. Meanwhile, Truscott *et al.* [17] also suggested that the geometry and density of the solid body do not determine if a cavity will be generated.

2.5. Classifications of cavity sealing

Cavity sealing is a phenomenon where the cavity formed at the wake of a body closes and pinches off as a consequence of factors including but not limited to capillary effects, aerodynamic pressure and static liquid pressure. There are in general, four types of cavity sealing, namely, deep seal, surface seal, quasi-static seal and shallow seal.

A reference to Figure 8 of Aristoff & Bush [21] shows a regime diagram that presents the four different cavity sealing phenomena observed following water entries by spheres with respect to their Bond number, $Bo = \rho g R_o^2 / \sigma$ and their Weber number, $We = \rho u_i^2 R_o / \sigma$. The symbol R_o represents sphere radius and if was to be kept constant, one can interpret from the aforementioned regime diagram that the following phenomena will be generated in order of increasing impact velocity: quasi-static, shallow seal, deep seal and surface seal.

2.6. Deep seal

In the classic scenario, a solid body with sufficient velocity and appropriate surface conditions will generate a significant cavity at its wake while submerging in

water. The cavity will continue to expand, connecting the body to the water surface until the combined influence of hydrostatic pressure, aerodynamic pressure and surface tension forces a pinch-off to occur. This pinch-off is typically known as deep seal to differentiate it from other forms of cavity closure described later. Two distinct cavities will form following the pinch-off – the upper cavity that continues to connect to the surface and the lower cavity that remains at the wake of the body.

The lower cavity can undergo further smaller-scale pinch-offs that will result in the formation of multiple smaller cavities while the upper cavity rapidly collapses towards the surface. During pinch-offs, an upward jet in the upper cavity and a downward jet in the lower cavity are being generated. An example of the downward jet can be seen in, for instance, Figure 3 of Grumstrup *et al.* [43]. Meanwhile, the upward jet will accompany the closure of the upper cavity and is subsequently ejected from the surface as a Worthington jet.

A phenomenon observed following deep seal is the formation of ripples along the cavity walls. Figures 1 and 3 of Grumstrup *et al.* [43] presented this phenomenon observed along the lower cavity. However, it should be noted that the ripples described here are of an entirely different nature to the ripples described in Chapters 4, 5 and 8 of this thesis.

Grumpstrup *et al.* [43] concluded that such ripple formation is simultaneous with acoustic emission and independent of surface tension. They also observed that the product of the acoustic frequency and the ripple wavelength was approximately equal to the speeds of the projectiles they used, independent of the shape and density of the projectile. They furthermore claimed that to their knowledge, these ripples have

only been mentioned twice in literature prior to their works, namely Worthington [4] and Mallock [6].

The dynamics of deep seal have been thoroughly studied and are mainly focused on the depth and time to pinch-off for various types of projectiles. Glasheen *et al.* [36] proposed non-dimensionalising the time to deep seal, t_{ds} to a single value, $\tau = t_{ds}(2g/D)^{0.5}$. The results obtained by Truscott & Techet [15] for spheres entering into water was τ = 1.726 +/- 0.0688, similar to the value of 1.74 which they claimed to have been reported by Gilbarg & Anderson [11]. The deep seal time varies with the geometry of the impacting body and disks have a non-dimensional time, τ = 2.285 +/- 0.0653, stated by Glasheen *et al.* [36] to be 31% greater than the corresponding value for spheres.

Meanwhile, Truscott & Techet [15] also utilised another regime to non-dimensionalise the deep seal time in their study of water entry of spinning spheres. The dimensionless deep seal time they used was $t_{ds}^* = u_i\, t_{ds} / D$ and the data was plotted against the Froude number, $Fr = u_i\, (gD)^{-0.5}$ for spheres of various mass ratio, $m^* = m_{sphere}/m_{fluid}$.

According to Figure 13 (a) of Truscott & Techet [15], the data for the dimensionless deep seal time, t^* for all mass ratios, spin rates and diameters collapsed into one line, forming a linear relationship with the Froude number as $t_{ds}^* = 5/4\ Fr$. Therefore, it can be understood that the deep seal time is only dependent on the diameter of the spheres while being independent of their initial velocity, rotation and density.

Truscott & Techet [15] continued to study the deep seal depths – the location of the sphere with respect to the water surface at the instant of deep seal. They non-dimensionalised the deep seal depth by making it a ratio to the sphere diameter. A reference to Figure 13 (c) of Truscott & Techet [15] shows that the deep seal depth is dependent on the sphere density as the data for spheres of different mass ratios diverged with increases in Froude number. The data in the figure included spinning and non-spinning cases, indicating minimal effect of spin on deep seal. Meanwhile, Figure 13 (d) of Truscott & Techet [15] shows that the data for the dimensionless deep seal depth would collapse as a linear function of the product of Froude number and the square root of mass ratio.

The pinch-off depth, in contrast to the deep seal depth, is the actual location of the cavity pinch-off with respect to the surface of the liquid. Duclaux *et al.* [30] used a mathematical theory to demonstrate the ratio of pinch-off depth to deep seal depth for spheres ranges between 1/3 and 1/2 for all Froude numbers. In addition, the results for the same ratio obtained by Marston *et al.* [40] involving Leidenfrost spheres also showed that the ratio was between 0.34 and 0.47 for their experiments.

2.7. Surface seal

A high-speed solid body generates another phenomenon in addition to the deep seal subsequent to its water entry. Following its impact on the water surface, a combination of aerodynamic pressure and curvature pressure, forces the splash crown to dome above the cavity, effectively sealing it [21]. The dome becomes an obstruction to the ejection of the Worthington jet from the surface, resulting in a reduced height accomplished by the jet.

Following surface seal, the cavity continues to expand and is pulled downwards under the surface and into the liquid. As the body continues its downward motion, either a single significant deep seal or multiple pinch-offs may occur to the cavity that is still connected to it, resulting in the formation of smaller cavities.

The transition from deep seal to surface seal for solid bodies with the same densities and dimensions occurs at a higher impact velocity and hence at higher Froude number. Hence the main factors governing the occurrence of surface seal are gravity and inertia [17]. Gilbarg & Anderson [11] showed that a decrease in atmospheric pressure would consequently lead to an increase in impact velocity required for the occurrence of surface seal.

2.8. Quasi-static pinch-off

Quasi-static pinch-off occurs when a relatively small solid body enters into a liquid at a relatively low velocity. As presented by Figure 4 of Aristoff & Bush [21], air entrainment at the wake of the sphere is minimal and only a tiny bubble attaches to the sphere following the pinch-off. Both the vertical and radial extents of the cavity are of the order of the capillary length, $l_c = (\sigma/\rho g)^{0.5}$. The dominant balance will be between gravity and surface tension as for a static meniscus and the depth of the sphere at the moment of pinch-off can be significantly less than the capillary length.

2.9. Shallow seal

Shallow seal occurs when the cavity simply pinches off relatively close to the liquid surface as shown in Figure 5 of Aristoff & Bush [21]. The main difference between shallow seal and deep seal is that the former is a consequence of capillary instability. Despite the difference in the dynamics of cavity closures, both shallow seal

and deep seal are similar in appearance. According to Truscott *et al.* [17], a jet will also be formed during shallow seal.

Although typically occurring at low speed entry as shown by Aristoff & Bush [21], surface conditions of the impacting body can still result in similar pinch-offs at relatively higher impact velocities. This unusual phenomenon will be described in Chapter 5.

2.10. Summary

The literature review has identified the phenomena, cavity formations and dynamics associated with water entries by solid bodies. However, at the point of writing, corresponding entries into two-layer systems of immiscible liquids was not previously studied in detail, and in particular, cavity formations during these entries were never studied before. Therefore, it would be of scientific interest to fill this gap in knowledge and thenceforth identify practical and engineering applications.

Chapter 3: Experimental set-up

''And whatsoever ye do in word or deed, do all in the name of the Lord Jesus, giving thanks to God and the Father by him.''

------ Colossians 3:17, KJV

The experimental set-up in general is illustrated in Figure 8. It consisted of a tank filled with a stratified, two-layer system of immiscible liquids where a shallow layer of oil rested above a deep pool of water prior to impacts of the free-falling spheres. It should be noted that for all experiments, the depth of the water underneath the oil layer and the width of the tank were always more than 20 times the diameter of the largest sphere used in the experiments. This was an endeavour to minimise wall effects on subsequent cavity dynamics.

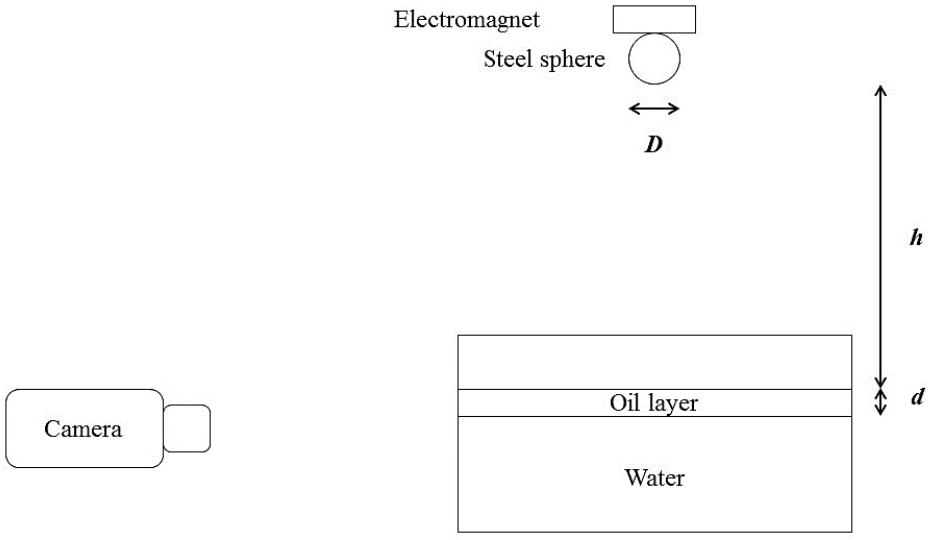

Figure 8: Graphical representation of the general experimental set-up (not drawn to scale). *D, h* and *d* represent the sphere diameter, release height and oil layer thickness respectively.

Unless explicitly stated otherwise, the spheres used in the experiments were AISI Chrome 52100 stainless steel spheres with density, ρ_s = 7,800kg/m^3 and diameters, 2.9mm $\leq D \leq$ 14.3mm. With the exception of a few test experiments which will be clearly indicated later, all steel spheres were immersed in acetone ($(CH_3)_2CO$) and dried using a clean paper tissue prior to each experiment. The objectives of this procedure were to ensure common surface conditions for all the spheres while simultaneously removing any contamination, such as grease, from the sphere surfaces.

Steel spheres were used in the experimental investigations as they have symmetrical shapes and relatively high densities compared to the liquids involved. Spheres represent the most fundamental geometric objects for a first investigation into the aspects explored in the present study. Meanwhile, the relatively high density of steel will minimise the effects of drag, buoyancy and surface tension on the spheres as they move in the liquids.

The main oils used in the experiments were either silicone oil or sunflower oil. The silicone oil was Allcosil 200/1000, a polydimethylsiloxane silicone oil with kinematic viscosity, ν_o = 1000mm^2/s and density, ρ_o = 970kg/m^3. According to the supplier, there would only be little change in physical properties of this silicone oil over a wide temperature range. The sunflower oil used in the experiments had kinematic viscosity, ν_o = 54.4mm^2/s and density, $\rho_o \approx$ 920kg/m^3. The water used was British tap water which had kinematic viscosity, ν_w = 1mm^2/s and density, ρ_w= 1000kg/m^3.

The thickness of the oil layer, d was varied between 5mm and 15mm. Hence the ratio of the sphere diameter to the oil layer thickness was in the range 0.19 $\leq D/d \leq$ 2.86. The minimum layer thickness of 5mm was close to the critical depth for which

a uniform coverage of the water surface could be established without surface tension resulting in disconnected oil patches. The purpose of the oil atop the water was to envelop the spheres with an oil film as they passed through it.

In addition to the sunflower and silicone oils, a few other liquids, namely rapeseed oil, grapeseed oil and methanol were also used for test experiments. A few types of plastic airsoft pellets commonly known as BB balls were also used to investigate the influence of sphere density on the type of phenomenon generated subsequent to spheres entering into two-layer liquid systems.

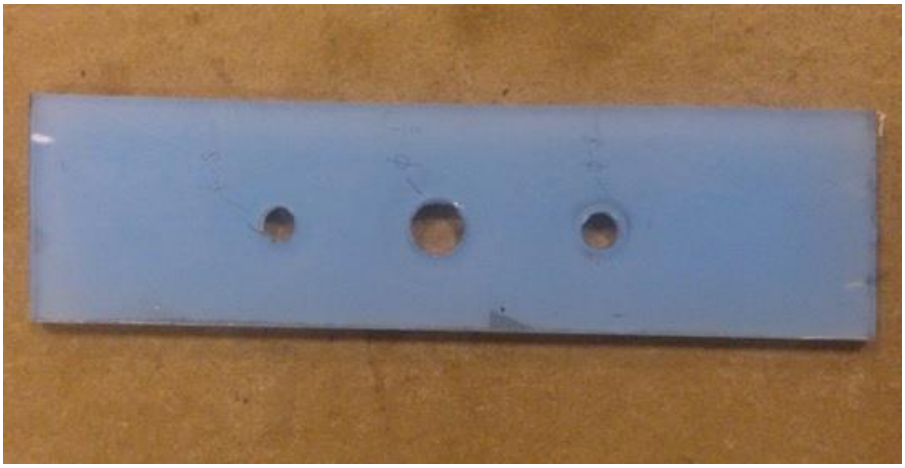

Figure 9: A plastic piece used to hold the spheres in place prior to their release. The centre hole was the place where spheres were placed and had the same diameter as the spheres. The two smaller holes at either side of the centre hole was used for the screws to attach the plastic piece to the electromagnet.

In an endeavour to obtain well-defined initial conditions, the spheres were held in place at their release position by a simple electromagnetic mechanism prior to their release. A piece of plastic as shown in Figure 9, was attached to the electromagnet to minimise the tendency of the spheres acquiring angular velocities at the moment they were released. The sphere would be positioned in the centre hole which had the same

diameter as the sphere itself while the two holes at either side of the centre hole were used for screws attaching the plastic piece to the electromagnet. Plastic pieces with different centre holes diameters were used for spheres of different sizes.

The electromagnet was placed on an adjustable stand in order to release the stationary spheres from various heights, $0.1\text{m} \leq h \leq 1.8\text{m}$ and hence impact velocities in the range $1.4\text{m/s} \leq u_i \leq 6\text{m/s}$ had been generated. The heights, h were measured from the bottom tip of the spheres to the surface of the liquids. However, due to errors associated with manual adjustments of the electromagnet vertically along the adjustable stand, uncertainty of h arose and was estimated to be E_h = +/- 0.01m. Therefore, the uncertainty of u_i at h = 0.1m is about +/- 5%. As the ratio E_h/h decreases with increases in h, the uncertainty of u_i will gradually become more insignificant to an extent that it can be neglected completely. Meanwhile, the Froude number, $Fr=u_i(gD)^{-0.5}$ in the experiments was in the range $3.7 \leq Fr \leq 35.6$.

A high speed camera (Phantom 5.2) was positioned directly at the front of the tank to record entire sphere entry processes. Video recordings of up to 2,900 frames per second from the high speed camera were analysed and measured using ImageJ, an image processing software developed at the National Institutes of Health, USA. In an endeavour to make very accurate measurements from the video recordings and simultaneously minimise parallax errors, laminated grid papers were placed in the same vertical plane as the sphere movements and photographed by the same camera prior to the experiments. These pictures would act as references for the subsequent measurements.

Throughout the experiments, room temperature was kept constant at 21^{o}C (294K) by an air conditioner to minimise temperature-induced viscosity variations in the liquids involved.

Chapter 4: General phenomena following sphere entries into two-layer liquid systems

''Open thou mine eyes, that I may behold wondrous things out of thy law.''

------ Psalm 119:18, KJV

4.1. Introduction

Four qualitatively different phenomena were observed subsequent to rigid spheres submerging in stratified two-layer, oil-water systems. The occurrence of any of the phenomena is dependent on impact conditions defined by the impact velocities, u_i and densities, ρ_b of the spheres in addition to the densities and surface tensions of the two liquids involved. The ratio D/d of sphere diameter to the oil layer thickness will have increased significance if d is sufficiently large to alter u_i significantly prior to the sphere entering into the deep pool of water directly underneath the oil layer.

The four general phenomena will be referred to as 'interface-trapped', 'tailing', 'transition' and 'rippling' and are shown, respectively, from left to right in Figure 10. 'Interface-trapped' occurs when the sphere becomes trapped at the oil-water interface, 'tailing' occurs when the sphere drags an 'oil tail' at its wake while falling into the water underneath the oil layer without the presence of a cavity. 'Rippling' occurs when the sphere generates a significant cavity at its wake while distinct ripples form along its cavity walls. 'Transition' is the phenomenon where physical features of both 'tailing' and 'rippling' occur simultaneously.

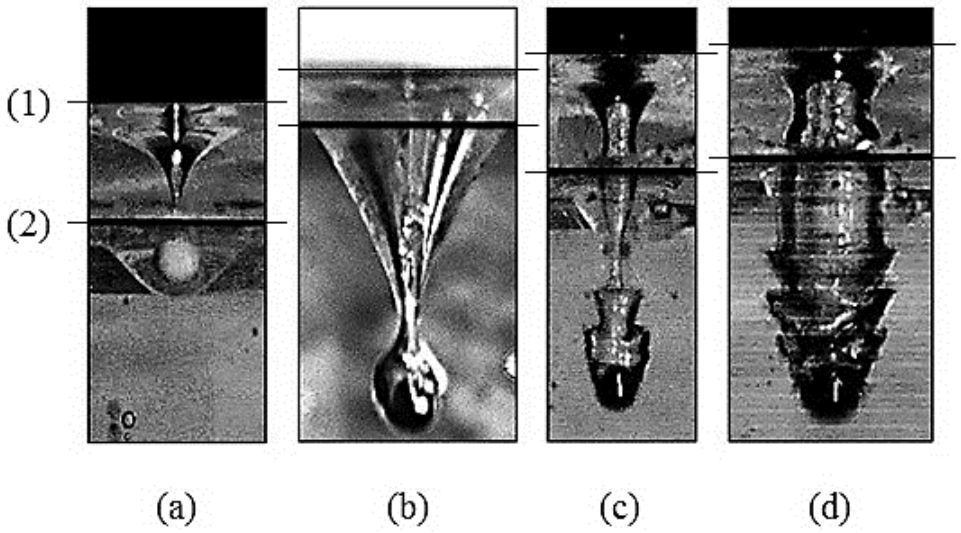

Figure 10: The four general phenomena observed following the entries of rigid spheres into a stratified two-layer system of immiscible liquids. (a): 'interface-trapped', (b): 'tailing', (c): 'transition' and (d): 'rippling'. The upper horizontal lines (1) indicate the surface of the two-layer, oil-water systems while the lower horizontal lines (2) mark the oil-water interface. Figure from Tan *et al.* [7], reprinted with permission. © Cambridge University Press 2016.

4.2. The 'Interface-trapped' and 'Tailing' phenomena

A rigid sphere that has a relatively low inertia because of its low density or low impact velocity, will generate either the 'interface-trapped' or 'tailing' phenomenon subsequent to its entry into a two-layer, oil-water system. These phenomena are shown in Figures 11 and 12, respectively.

During 'interface-trapped', the sphere enters into the oil layer and generates a relatively tiny cavity at its wake which quickly pinches off in a process identical to the quasi-static pinch-off. As the combined force of oil-water interfacial tension and buoyancy is greater than the weight of the sphere, the sphere becomes trapped and settles at the interface as illustrated in Figure 11.

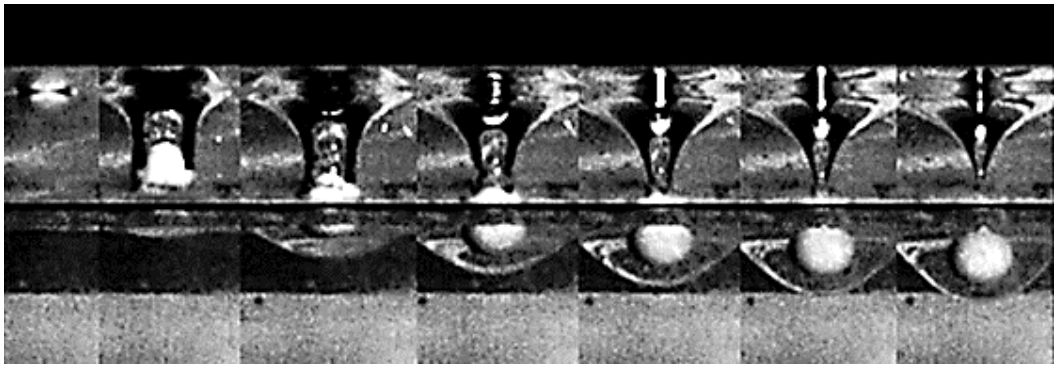

Figure 11: The ‘interface-trapped’ phenomenon occurring after a plastic airsoft pellet (BB ball) of density, ρ_b = 2,400kg/m^3, diameter, D = 6mm and impact velocity, u_i = 1.98m/s entered into a two-layer, silicone oil-water system. The silicone oil layer had thickness, d = 12.5mm and kinematic viscosity, ν_o = 1000mm^2/s. The time difference between each successive image is 10ms.

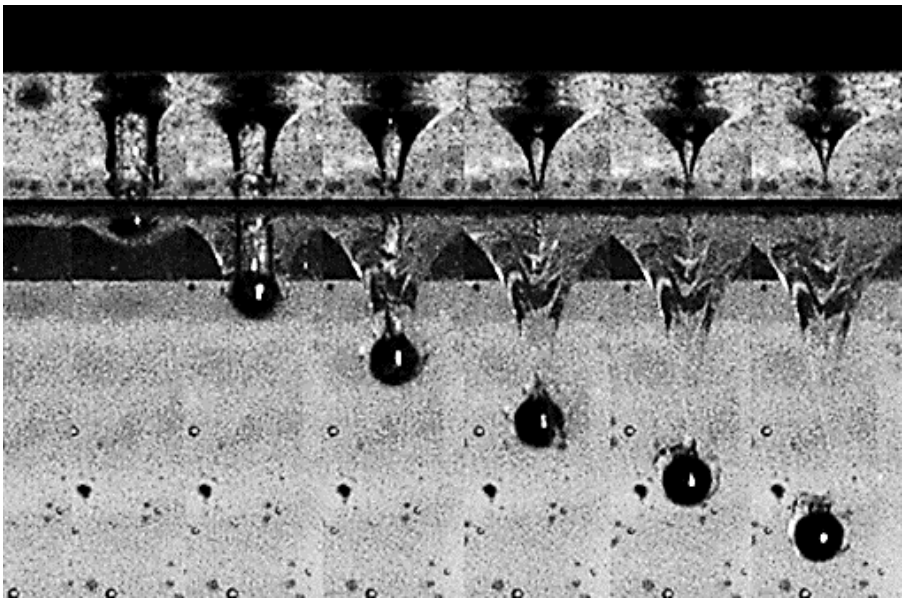

Figure 12: The ‘tailing’ phenomenon occurring after a steel sphere (D = 5mm) entered into a two-layer, silicone oil-water system with an impact velocity, u_i = 1.98m/s. The silicone oil layer had thickness, d = 12.5mm and kinematic viscosity, ν_o = 1000mm^2/s. As the sphere moved in the water, an ‘oil tail’ continued to connect it to the oil layer. The time difference between each successive image is 10ms.

The ‘tailing’ phenomenon will occur should a rigid sphere possess a slightly higher inertia relative to ‘interface-trapped’, and its weight is greater than the total oil-water interfacial tension and buoyancy forces. During ‘tailing’, the sphere generates a small cavity at its wake which will also quickly pinch off in processes that are similar to quasi-static pinch-off and shallow seal. However, in contrast to ‘interface-trapped’, the sphere passes through the oil-water interface and enters into the deep pool of water with a relatively low velocity, dragging an ‘oil tail’ which continues to connect the sphere to the oil layer.

The mathematics and numerical simulations of the ‘interface-trapped’ and ‘tailing’ phenomena can be found in, for instance, Hartland [44, 45], Hartland & Robinson [46], Maru *et al.* [47] and Geller *et al.* [48]. However, it should be noted that the focus of those studies was on the motion of the solid spheres at the liquid-liquid interface without the presence of any cavity.

It was observed that occasionally, a relatively small and light sphere might experience both ‘interface-trapped’ and ‘tailing’. After passing through the oil-water interface, the sphere dragged an ‘oil tail’ into water and ‘tailing’ was observed. However, the ‘oil tail’ would subsequently pull the sphere back to the oil-water interface where the sphere eventually settled, resulting in ‘interface-trapped’ being observed. During this process, the sphere might also oscillate vertically in and out of the oil layer. Nevertheless such phenomenon is not the focus of the present study.

4.3. The ‘Rippling’ phenomenon

A rigid sphere that possesses sufficient impact velocity will generate a significant cavity at its wake after entering into a two-layer, oil-water system. This is identical to the process that will occur during corresponding entries into single-phase homogeneous liquids. Similarly, the cavity generated at the wake of the sphere will expand as the sphere continues its downward movement simultaneously before it experiences deep seal.

However, unique physical features have been observed forming on the cavities generated by spheres that entered into two-layer, oil-water systems. These features are neither previously observed nor known to exist during corresponding entries into single-phase homogeneous liquids.

When rigid spheres enter into a homogeneous environment of single-phase liquid such as water or oil, the walls of the cavities formed at their wakes have been observed to be smooth, as illustrated in Figures 13 and 14. This observation is supported by photographs contained in numerous publications, for instance, May [10], Truscott & Techet [15, 16], Truscott *et al.* [17, 18], Aristoff & Bush [21] and Duclaux *et al.* [30] for water and Reynolds numbers up to the order of several hundred thousand and in Le Goff *et al.* [41] for silicone oil and Reynolds numbers up to around 100.

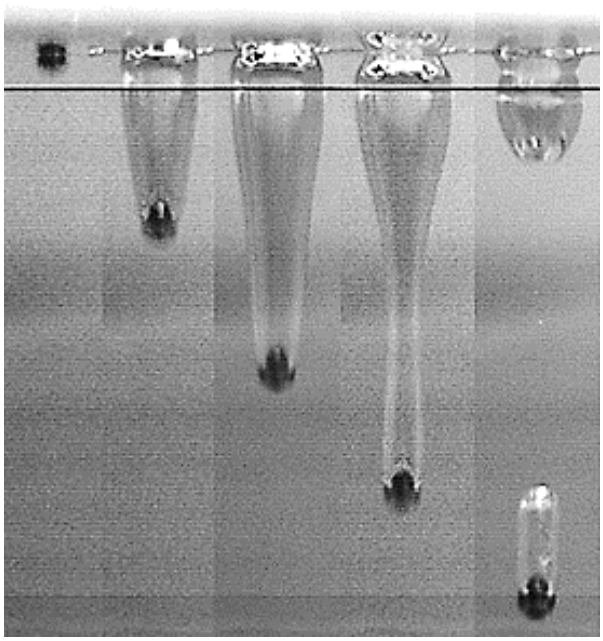

Figure 13: Cavity formation following the entry of a steel sphere (D = 6mm) into pure sunflower oil (ν_o = 54.4mm^2/s) at impact velocity, u_i = 3.1m/s. The time difference between each successive image is 10ms. Figure from Tan *et al.* [7], reprinted with permission. © Cambridge University Press 2016.

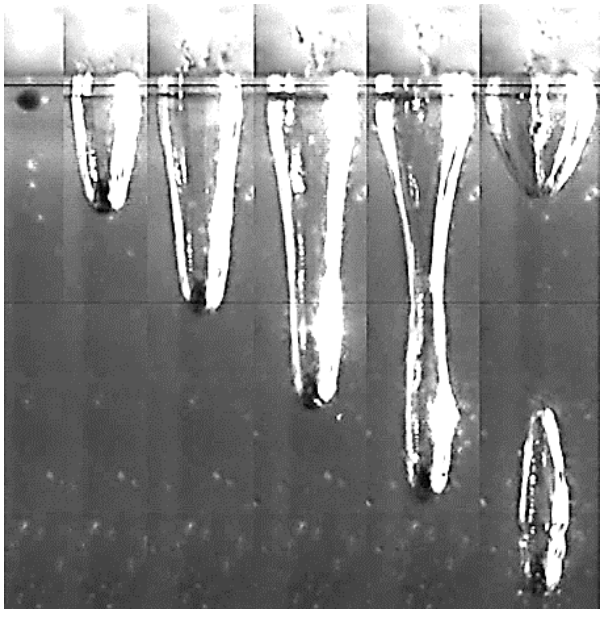

Figure 14: Cavity formation following water entry of a steel sphere (D = 10mm) at u_i = 3.1m/s. The time difference between each successive image is 10ms.

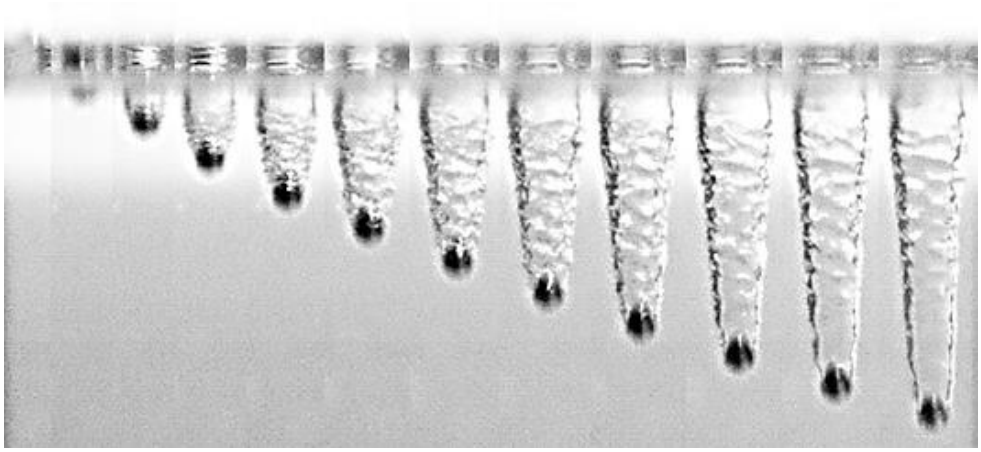

Figure 15: Cavity formation at the wake of a steel sphere (D = 6mm) that entered into a two-layer system of sunflower oil-water at u_i = 3.7m/s. The sunflower oil layer had thickness, d = 5mm and kinematic viscosity, ν_o = 54.4mm^2/s. Ripples can be observed forming along the cavity walls below the oil-water interface. The time difference between each successive image is 2ms.

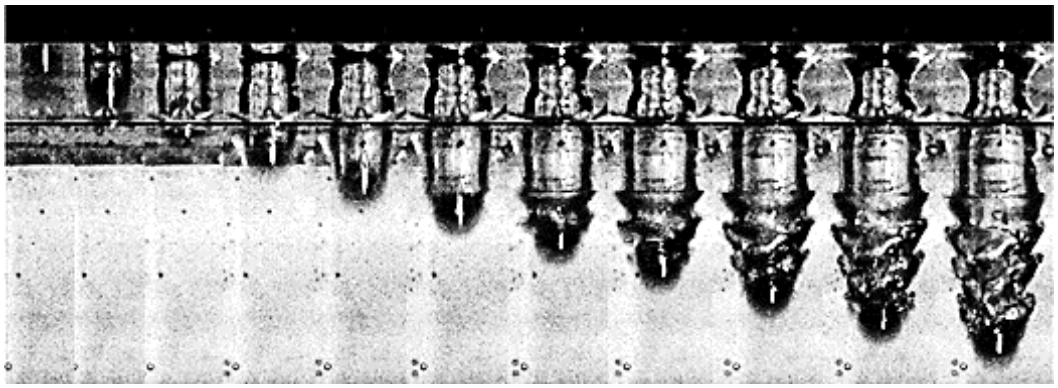

Figure 16: Cavity formation following entry of a steel sphere (D = 8mm) into a two-layer, silicone oil-water system at u_i = 3.43m/s. The silicone oil layer had thickness, d = 12.5mm and kinematic viscosity, ν_o = 1000mm^2/s. The ripples are more quantifiable and obvious as compared to those shown in Figure 15. The time difference between each successive image is 2ms.

However, both the formation and appearance of the air cavity will be substantially modified should the spheres pass through an oil layer immediately before entering into the water directly underneath the oil layer. A striking observation is that the boundary between the air cavity and the ambient liquid will no longer be completely smooth but wave-like instability patterns or ripples will develop along the cavity walls as illustrated in Figures 15 and 16. These ripples will only begin to form at a depth below the oil-water interface and appear to be stationary with respect to the vertical plane, suggesting it to be an instability perpendicular to the sphere movements. It can also be observed that these ripples will become more obvious, quantifiable and well-defined for increased viscosities of the oil layer.

As a result of the formation of ripples along the cavity walls, this phenomenon is referred to as ‘rippling’ and the ripples will be the subject of study in Chapter 8 of this thesis.

4.4. The ‘Transition’ phenomenon

As described earlier in Chapter 4.1, it is possible for physical features of both ‘tailing’ and ‘rippling’ to occur simultaneously. This phenomenon is given the name ‘transition’ and occurs at impact velocities between those required for ‘tailing’ and ‘rippling’ as shown by the regime diagrams (Figures 19 and 20) in Chapter 4.5.

As illustrated in Figure 17, a cavity is generated at the wake of the sphere and instead of undergoing deep seal, it experiences shallow seal. A small cavity remains attached to the sphere following shallow seal while an ‘oil tail’ connects the sphere and the remaining air cavity to the oil-water interface.

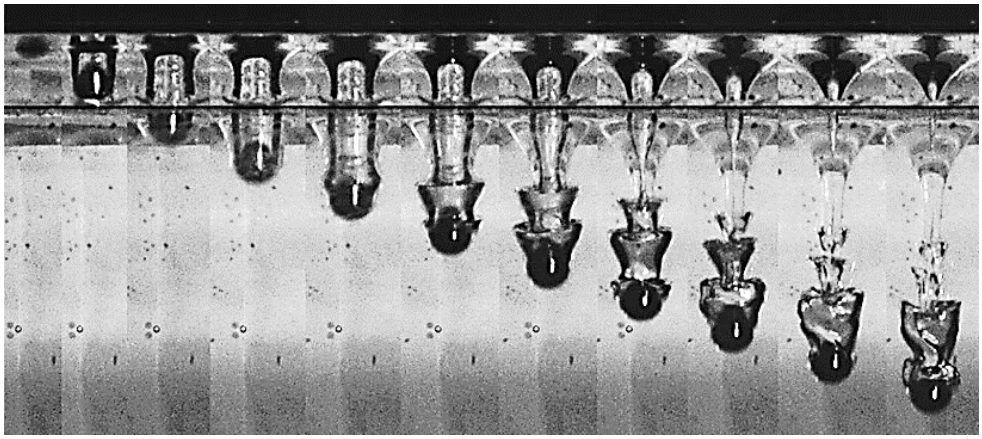

Figure 17: The ‘transition’ phenomenon occurring after a steel sphere (D = 8mm) entered into a two-layer, silicone oil-water system at u_i = 1.98m/s. The silicone oil layer had thickness, d = 12.5mm and kinematic viscosity, ν_o = 1000mm^2/s. The time difference between each successive image is 5ms.

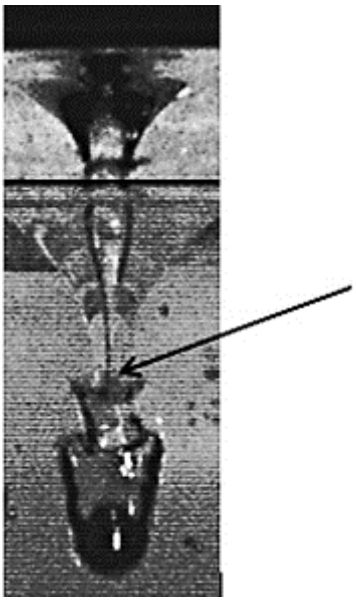

Figure 18: Cavity sealing during 'transition': the black arrow indicates the location of the sealing. The sphere in the image had diameter, D = 7mm and impact velocity, u_i = 2.43m/s while the silicone oil layer that rested on the water surface had a thickness, d = 12.5mm.

The ripples formed during ‘transition’ will also be generated at a depth below the oil-water interface. However, unlike those formed during ‘rippling’, each ripple

has already begun contracting while the ripple directly below it is still expanding. In addition, the distance between each successive ripple is not constant and cavity sealing is observed to take place at the top of the first ripple as shown and indicated by the arrow in Figure 18.

4.5. Phase diagrams

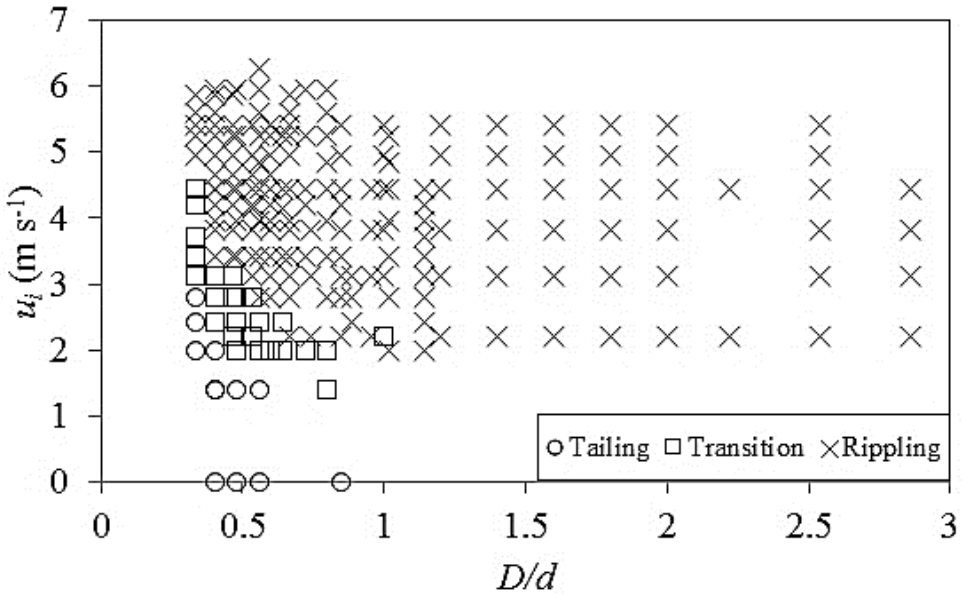

Figure 19: Phase diagram illustrating the parameter regimes where the characteristic entry phenomena were observed, for the two-layer, silicone oil (ν_o = 1000mm^2/s)-water system, for different values of the relative sphere diameter D/d and impact velocity u_i. The silicone oil layer in this system had thickness, d that varied between 5mm and 15mm. Figure from Tan *et al.* [7], reprinted with permission. © Cambridge University Press 2016.

Figure 19 illustrates the three different phenomena that were observed subsequent to steel spheres entering and submerging in the two-layer, silicone oil-water system mainly studied in this thesis. As a consequence of the relatively high density of steel compared to that of the silicone oil (ρ_s/ρ_o = 8.04) and water (ρ_s/ρ_w = 7.8), the phenomenon of 'interface-trapped' was not observed during the experiments.

Meanwhile, the four data points on the abscissa of Figure 19, for which u_i = 0m/s, were obtained by releasing the sphere immediately above the surface of the silicone oil layer.

As one might have expected, Figure 19 illustrates that should the oil layer thickness remain constant, a steel sphere of a given diameter will generate 'tailing', 'transition' and 'rippling' in order of increasing impact velocity.

In an attempt to investigate the influence of sphere densities on the occurrences of the phenomena, BB balls were also used. The BB balls had a common diameter, D = 6mm but consisted of balls of four different densities: 1,070kg/m^3, 1,760kg/m^3, 2,400kg/m^3 and 3,100kg/m^3. They were held stationary by an arm attached to an adjustable stand and released by loosening the aforementioned arm at various heights. As the BB balls were of lower densities compared to steel, the phenomenon of 'interface-trapped' was also observed during these entries.

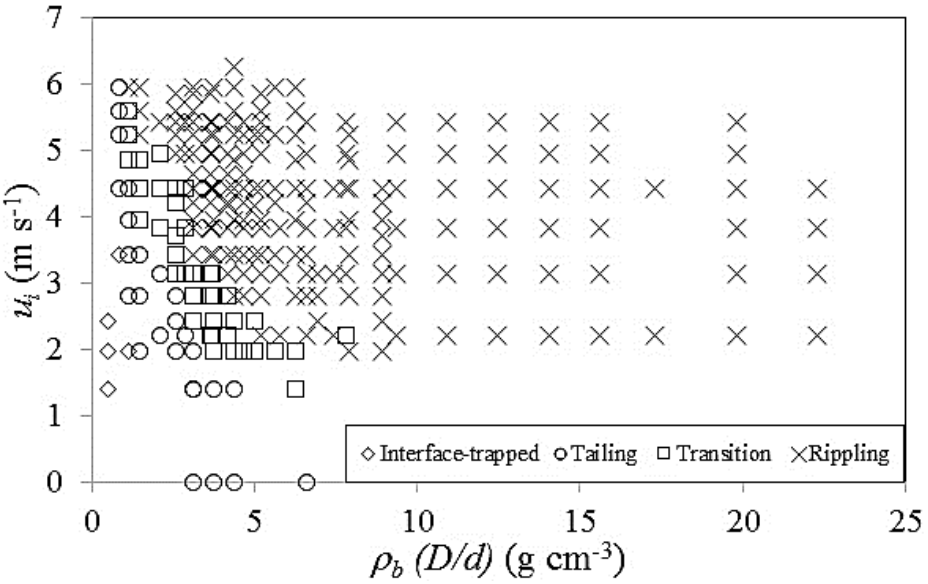

Figure 20: A similar phase diagram as Figure 19 but with BB balls used in addition to the steel spheres. The horizontal axis is now the product of D/d and sphere density, ρ_b.

The observations have been computed in a similar way to that done in Figure 19. However, the horizontal axis for the new regime diagram shown in Figure 20 is now a product of D/d is and sphere density, ρ_b (in g/cm^3). Hence it can be concluded from Figure 20 that a lighter sphere will require a higher impact velocity to generate 'transition' and 'rippling' compared to a heavier sphere of the same diameter.

Chapter 5: Observations following the entry of steel spheres into sunflower oil

''For with God nothing shall be impossible.''

------ St Luke 1:37, KJV

5.1. Introduction

Phenomena that are not consistent with the present literature and current understanding have been observed subsequent to stainless steel spheres entering into sunflower oil and the two-layer, sunflower oil-water system. It has been found that such phenomena arise from the surface conditions of the steel spheres with respect to the sunflower oil, thereby demonstrating the substantial influences both the surface conditions of a body and the upper layer liquid in a two-layer liquid system can potentially have on cavity dynamics.

However, due to the uncertainties and difficulties of effectively quantifying the required experimental conditions, the measurements obtained from the unusual phenomena will not be analysed in further detail. Therefore, only pure experimental observations and results will be presented in this chapter.

5.2. Two-layer, sunflower oil-water experiments

The order of the different cavity sealing phenomena generated with respect to increasing impact velocity can be interpreted from the regime diagram presented by Aristoff & Bush [21]. Hence it is understood that shallow seal occurs at lower impact velocities compared to deep seal.

However, during entries of steel spheres into the two-layer, sunflower oil-water system at relatively high impact velocities, shallow seal was also observed in addition to the deep seal. Further increases in impact velocity even led to the deep seal not occurring completely, resulting in the cavity experiencing only shallow seal. During such scenarios, relatively small cavities were generated and these cavities would leave a trail consisting of a mixture of air bubbles and oil droplets at their wakes as they were being pulled downwards by the spheres to which they were attached.

Figures 21 to 24 present the observations subsequent to steel spheres of the same diameter entering into the two-layer, sunflower oil-water system in order of increasing impact velocity. Meanwhile, video recordings revealed that it was possible for spheres to shed parts of their cavities in the form of vortex clouds that consisted of mixtures of oil droplets and air bubbles. Hence a small region of emulsion could be generated behind the sphere during this process and an example is shown in Figure 24.

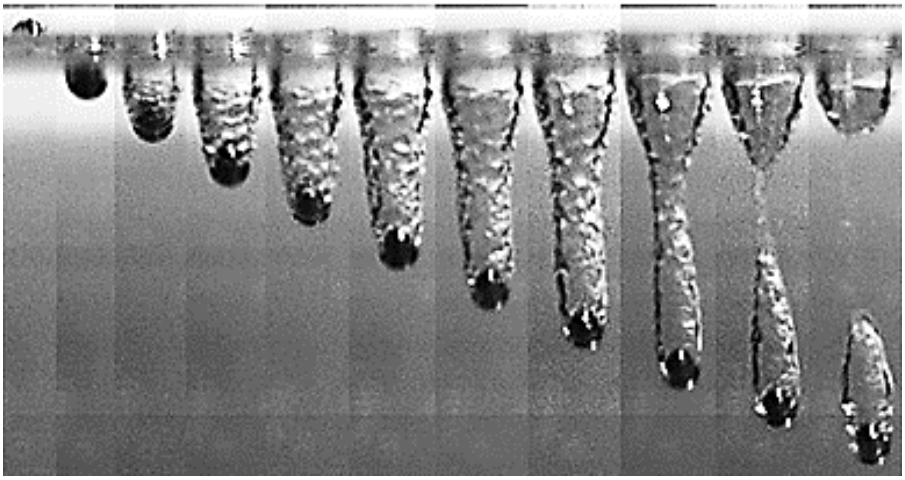

Figure 21: The entry of a steel sphere (D = 10mm and u_i = 2.43m/s) into a deep pool of water filled with a 5mm sunflower oil layer. Only the deep seal has been observed in this figure. The time difference between each successive image is 5ms.

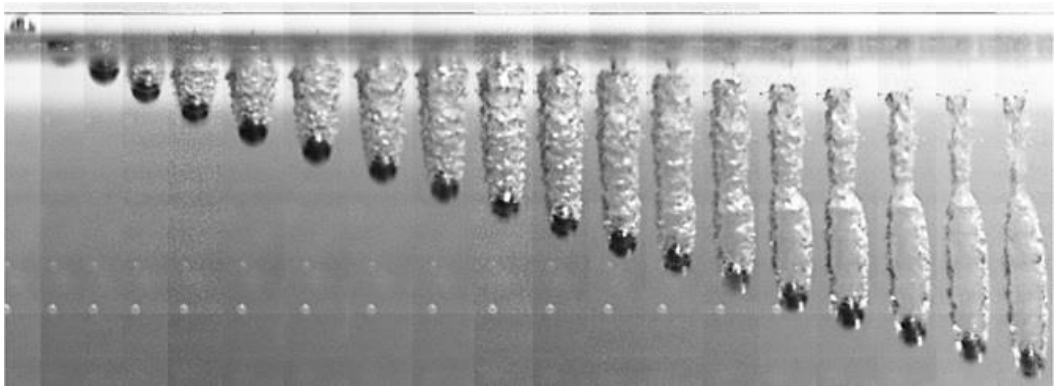

Figure 22: The entry of a steel sphere (D = 10mm and u_i = 3.96m/s) into a deep pool of water filled with a 5mm sunflower oil layer. Shallow seal was observed close to the oil-water interface while deep seal can be seen occurring slightly differently to that shown in Figure 21. The time difference between each successive image is 2ms.

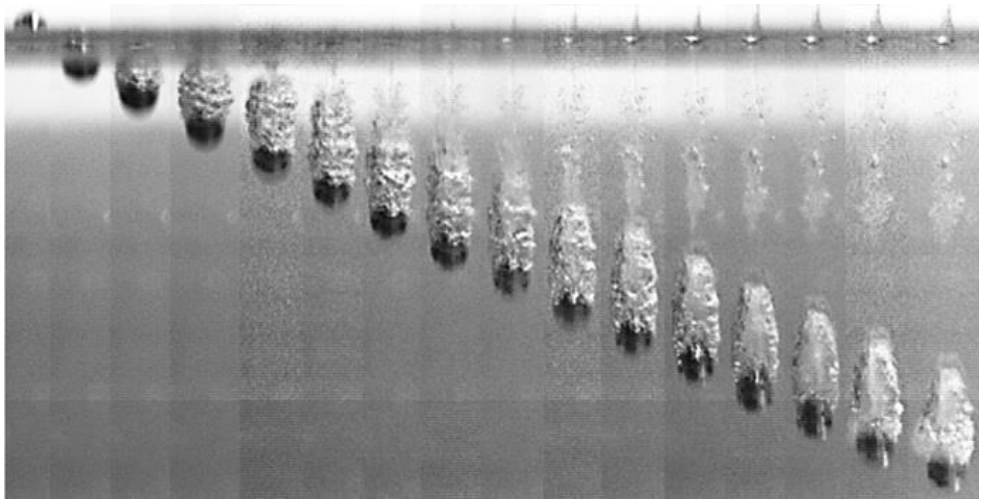

Figure 23: The entry of a steel sphere (D = 10mm and u_i = 4.85m/s) into a deep pool of water covered with a 5mm sunflower oil layer. Shallow seal occurred close to the oil-water interface about 10ms after sphere entry. It was observed that instead of an obvious deep seal as shown in Figure 21, the cavity left a trail of oil at its wake. The time difference between each successive image is 2ms.

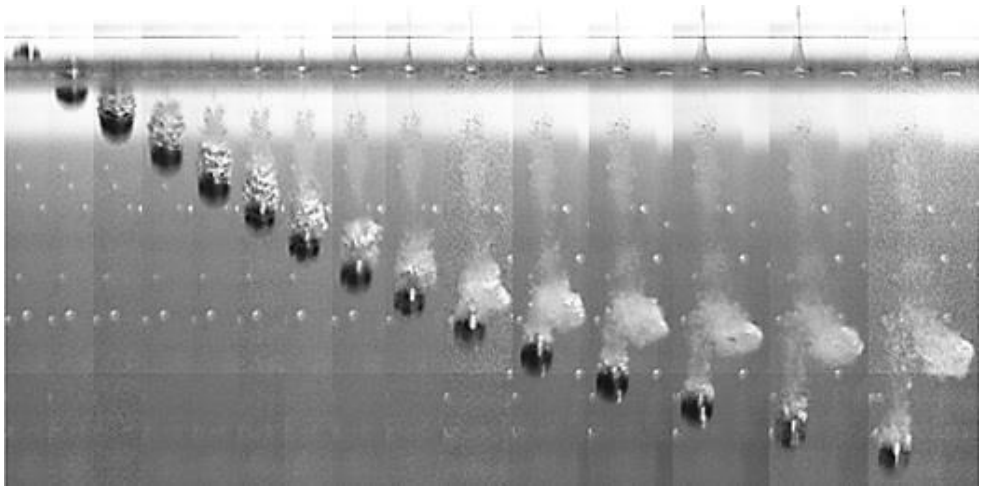

Figure 24: The entry of a steel sphere (D = 10mm and u_i = 5.6m/s) into a deep pool of water covered with a 5mm sunflower oil layer. Deep seal did not occur and a vortex cloud that consisted of a mixture of air-oil bubbles was generated at the wake of the sphere, creating a small region of emulsion. It should be noted that the width of the latter images have been increased to show the vortex cloud. The time difference between each successive image is 2ms.

The shallow seal transition velocity, u_{ss} is defined as the impact velocity of the sphere above which the unusual shallow seal mentioned earlier was observed. Through multiple experiments, it was found that the value of u_{ss} generally decreased with increases in sphere diameters as shown in Figure 25.

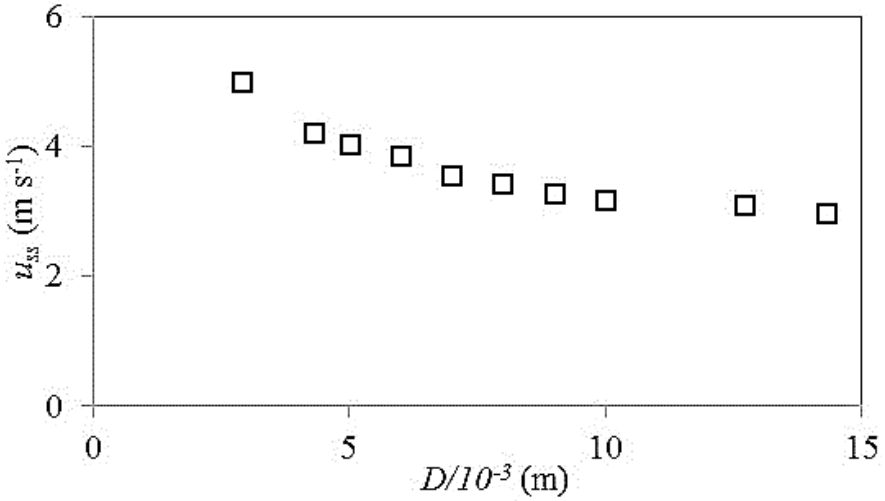

Figure 25: The shallow seal transition velocity, u_{ss} as a function of the diameter, D of the steel spheres in the present study.

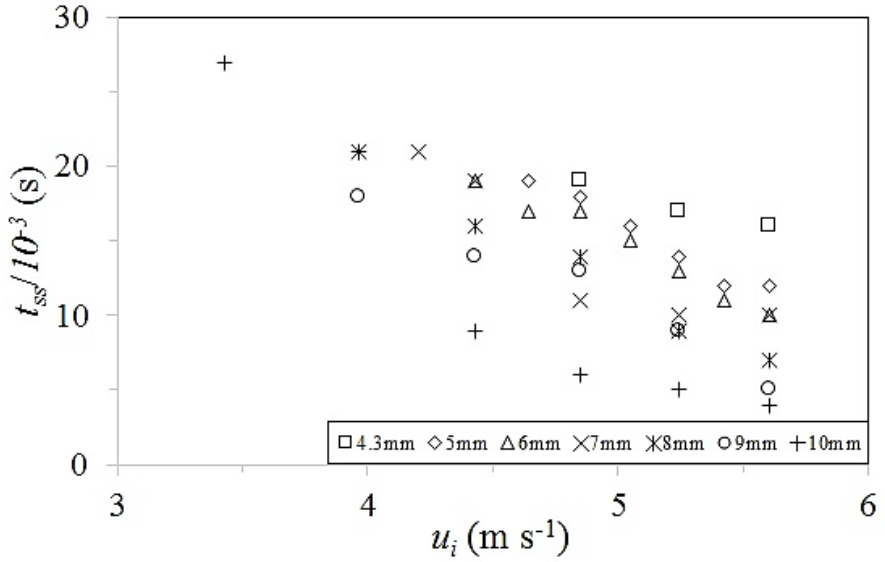

Figure 26: The shallow seal time, t_{ss} as a function of the impact velocities, u_i for spheres of various diameters as indicated in the legend.

The shallow seal time, t_{ss} is defined as the time interval between the instant of sphere entry into the two-layer, sunflower oil-water system and the instant when the unusual shallow seal occurs. Figure 26 presents the data obtained for spheres of different diameters and various impact velocities.

The results from Figure 26 suggest that the cavity collapsed more rapidly for larger spheres and also for spheres that possessed higher impact velocity, u_i. A consequence of the relatively short t_{ss} for larger spheres was the formation of smaller cavities as shown in Figures 23 and 24.

5.3. Sunflower oil experiments

The unusual phenomena mentioned earlier were not observed during corresponding experiments involving the same steel spheres that entered into water and the two-layer, silicone oil-water systems. Hence in an endeavour to identify the origins of these phenomena, experiments involving steel spheres entering into a deep pool of pure sunflower oil were also performed.

The experiment set-up was identical to that described in Chapter 3 and shown in Figure 8. The only difference, however, was instead of the two-layer, oil-water system, the tank was filled completely with pure sunflower oil. In order to minimise wall effects on cavity dynamics, the width of the tank and the depth of the sunflower oil was always more than 20 times the diameter of the largest spheres that were used in the experiments.

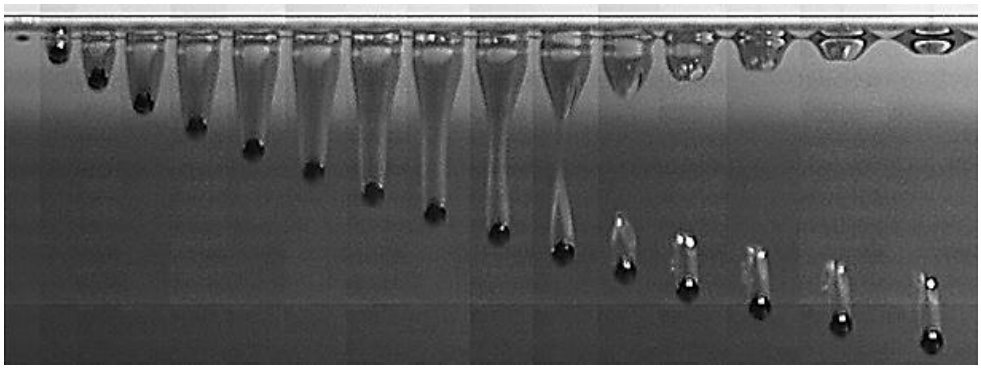

Figure 27: Deep seal observed after a steel sphere (D = 8mm, u_i = 2.8m/s) submerged in a deep pool of sunflower oil. The sphere created a long cavity at its wake which split into two at a depth about half of that of the sphere. An upward jet was being ejected from the surface despite not being visible in the images. The time difference between each successive image is 4ms.

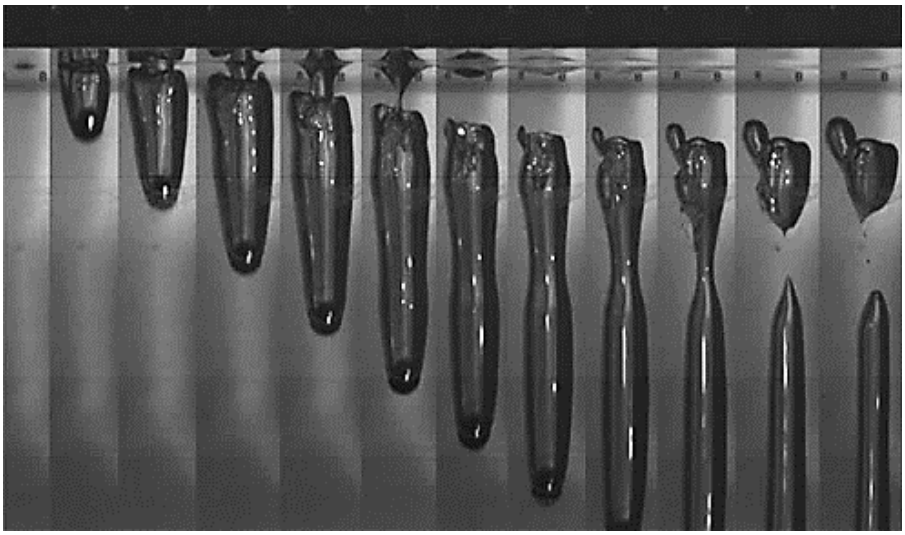

Figure 28: Deep seal and shallow seal observed following the entry of a steel sphere (D = 7mm and u_i = 3.96m/s) into a deep pool of sunflower oil. The sphere created a long cavity which simultaneously expanded and dragged into the oil. The time difference between each successive image is 4ms.

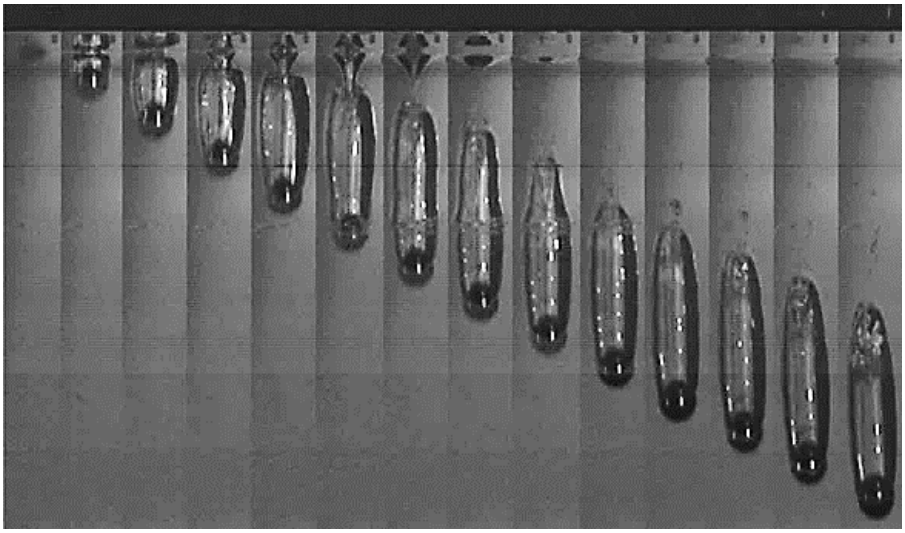

Figure 29: Shallow seal observed following the entry of a steel sphere (D = 8mm, u_i = 4.64m/s) into sunflower oil. The cavity pinched off immediately underneath the surface at about 12ms after sphere entry and resulted in the formation of a relatively small cavity. The time difference between each successive image is 2ms.

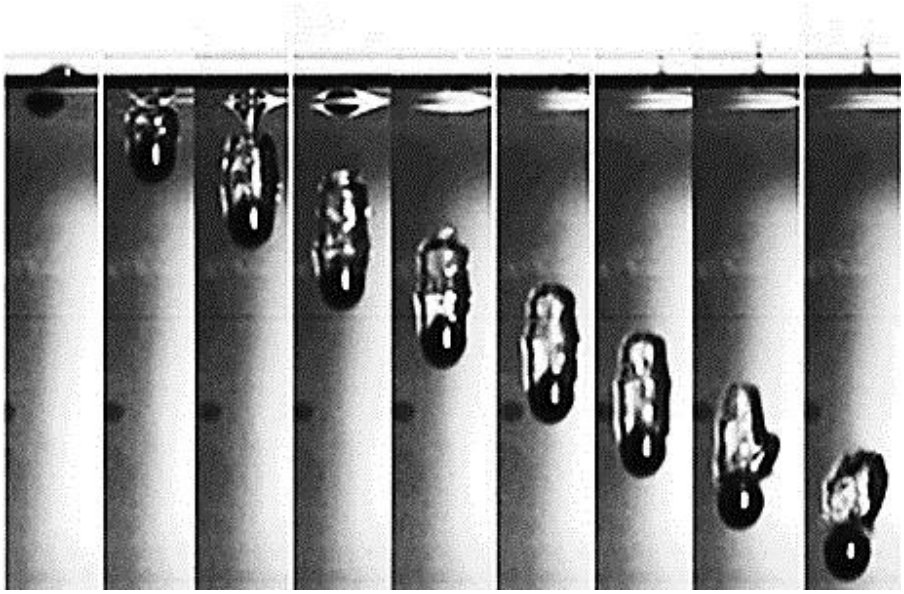

Figure 30: Another example of the shallow seal. The sphere (D = 8mm, u_i = 5.6m/s) created an even smaller cavity than that in Figure 29 but pinched off about 5ms after sphere entry. The time difference between each successive image is 2ms.

During the experiments, phenomena similar to those documented in Chapter 5.2 were observed. Likewise at relatively high impact velocities, the cavity at the wake of the spheres experienced shallow seal, pinching off immediately underneath the surface. Figures 27 to 30 present the general cavity sealing phenomena observed during these entries: Figure 27 shows the cavity experiencing only the classic deep seal, Figure 28 shows the cavity experiencing both deep seal and shallow seal while Figures 29 and 30 show the cavity experiencing only the unusual shallow seal.

As presented in Figures 29 and 30, the appearance of the shallow seal was very similar to that of the classic deep seal. The cavity split into two and the upper cavity would thenceforth collapse rapidly towards the surface, ejecting an upward jet as shown in Figure 30. This upward jet however, would usually be thinner and reach a lower height compared to the jet ejected from the classic deep seal.

Figure 31 presents the regime diagram showing the cavity sealing phenomena observed during the experiments with respect to the diameter, D and impact velocity, u_i of the spheres. It was found that for spheres that had the same diameter, the value of the shallow seal transition velocity, u_{ss} (minimum impact velocity required for the occurrence of shallow seal as defined in Chapter 5.2) for entries into both pure sunflower oil and the two-layer, sunflower oil-water system described in Chapter 5.2 were almost identical. Therefore, the observation supports the hypothesis that the unusual phenomena documented in Chapter 5.2 had originated from the thin sunflower oil layer that was resting on the water surface.

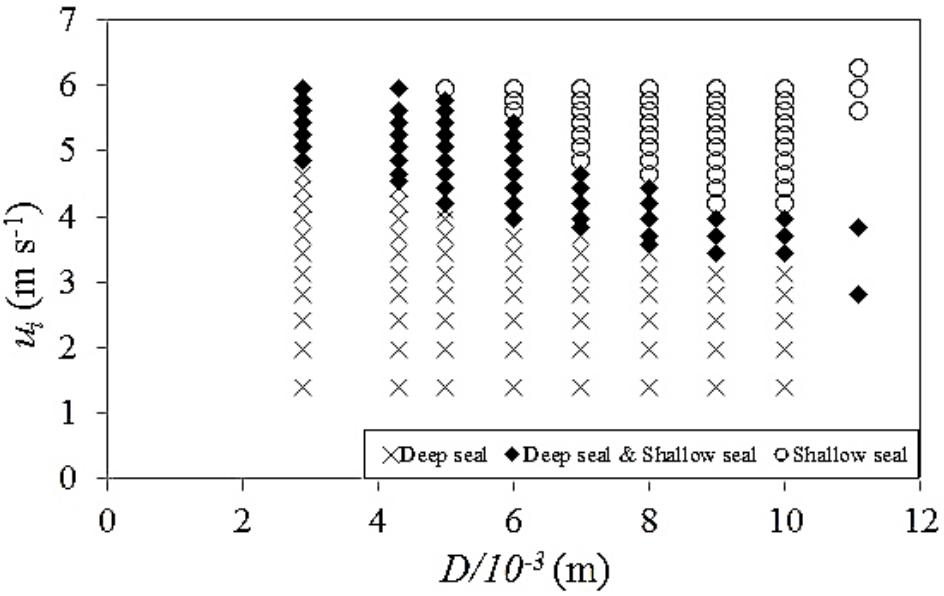

Figure 31: The regime diagram showing the phenomena ('deep seal', 'deep seal & shallow seal' and 'shallow seal') observed during the experiments with respect to the diameter, D and impact velocity, u_i of the spheres that entered into a deep pool of pure sunflower oil.

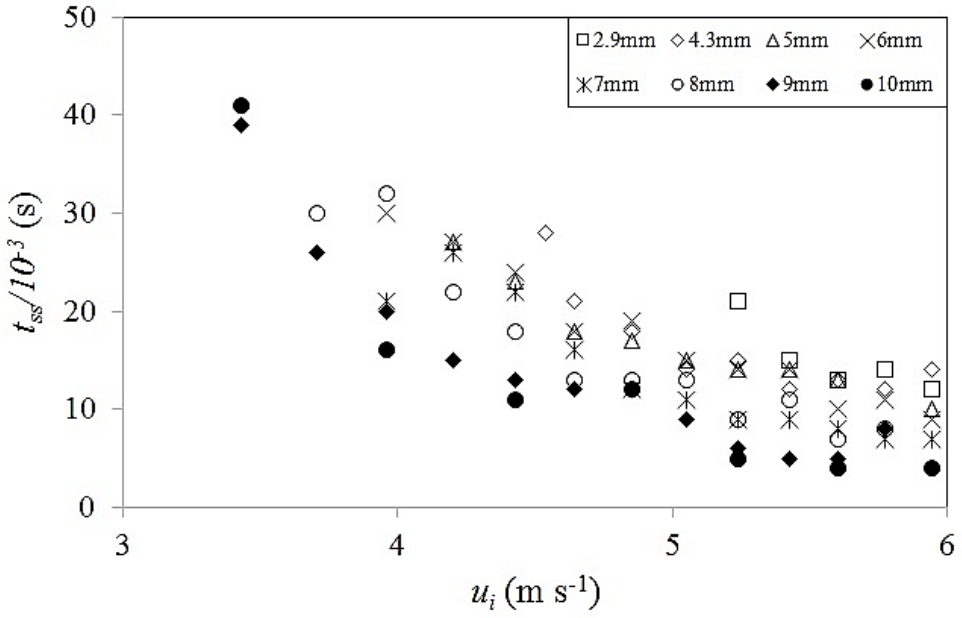

Figure 32: Shallow seal time, t_{ss} as a function of impact velocity, u_i for spheres of different diameters as indicated in the legend.

The shallow seal time, t_{ss}, with the same definition as that in Chapter 5.2 is the time interval between the instant of oil entry and the instant when shallow seal occurs. Likewise, t_{ss} is presented in Figure 32 as a function of impact velocity, u_i for spheres of different diameters.

Similar to during entries into the two-layer, sunflower oil-water system, the cavity collapsed more rapidly for larger spheres and also for spheres that possessed higher impact velocity, u_i. In addition, the relatively short t_{ss} for larger spheres entering sunflower oil at higher velocities also resulted in the generation of relatively small cavities at the wake of these spheres.

5.4. Cavity outlines during shallow seal

Figures 33 to 35 present the plots showing the outlines of the spheres and their cavities that were traced using ImageJ, an image processing software described in Chapter 3. It should be noted that the cavities of these spheres did not experience deep seal. The figures present the horizontal (x) and vertical (y) displacement with reference to the first point of contact the impacting sphere made with the oil surface. Hence x represents the 'width' while y represents the depth despite it being presented upside-down for convenience.

The figures show that the cavity pinch-off points for shallow seal observed in the experiments were at a depth of approximately 5mm below the oil surface for all sphere diameters and impact velocities. The sphere depth is defined as the displacement of the sphere from the oil surface. Figures 33 and 34 appear to suggest that an increase in impact velocity will lead to a decrease in sphere depth at the instant of shallow seal. Meanwhile, Figure 35 apparently suggests that for spheres possessing

the same impact velocity, the sphere depth at the instant of shallow seal decreases with an increase in sphere diameter.

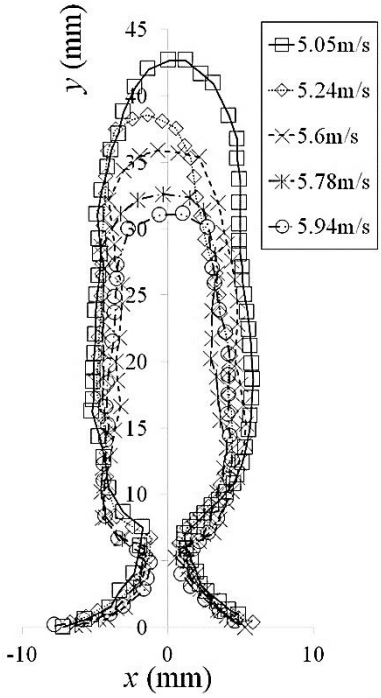

Figure 33: Cavity outlines during shallow seal for 7mm spheres at various impact velocities.

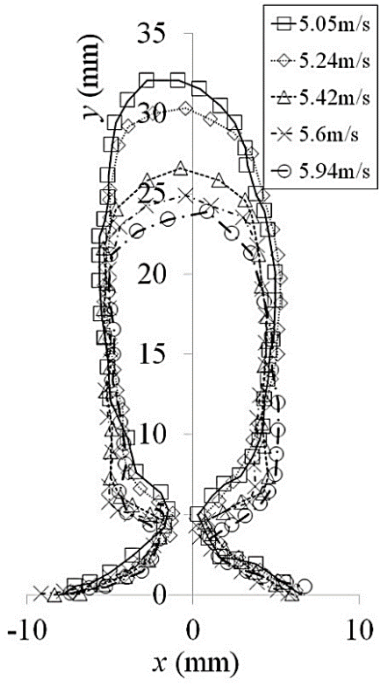

Figure 34: Cavity outlines during shallow seal for 9mm spheres at various impact velocities.

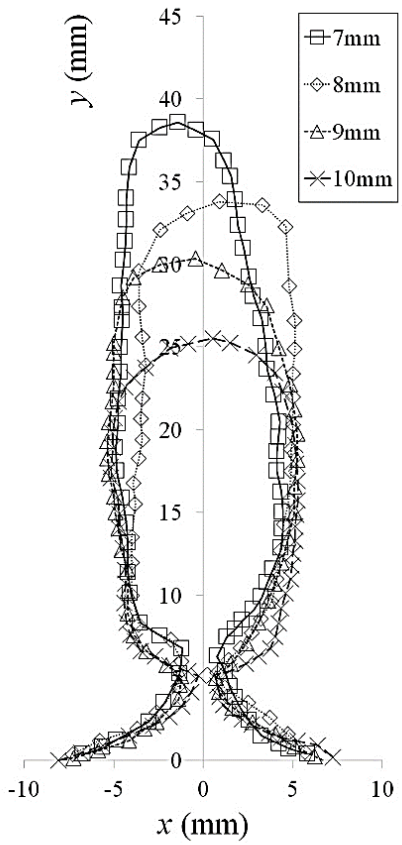

Figure 35: Cavity outlines during shallow seal for spheres of various diameters at impact velocity, u_i = 5.24m/s.

As written in Chapter 5.1, due to the uncertainties and difficulties of effectively quantifying the required experimental conditions, it is not possible to establish any accurate relationship between the relevant physical quantities presented in Figures 33 to 35 without first quantifying the effects of surface conditions. Hence these figures will only present a 'pattern' one can reasonably expect when some of the physical quantities are being varied.

5.5. Experiments using oily spheres and other vegetable oils

It has been hypothesised that the unusual phenomena described in Chapters 5.2 and 5.3 were influenced by the surface conditions of the steel spheres. Therefore, in order to verify this hypothesis, the same sunflower oil-entry experiments documented in Chapter 5.3 were repeated with a different set of spheres. The new spheres were the same type of stainless steel spheres used previously. However, they were immersed in sunflower oil itself and dried using a clean tissue paper prior to each experiment. Therefore, the new set of spheres acquired oily surfaces and are referred to as 'oily spheres'.

In the new set of experiments, surface seal was reproduced and shown in Figure 36. In addition, the order of the different cavity sealing phenomena generated with respect to increasing impact velocities interpreted from the regime diagram presented by Aristoff & Bush [21], was also being reproduced.

The most significant observation in these experiments is that the unusual phenomena, namely the shallow seal occurring at relatively higher impact velocities and the absence of deep seal at even higher velocities, did not occur completely.

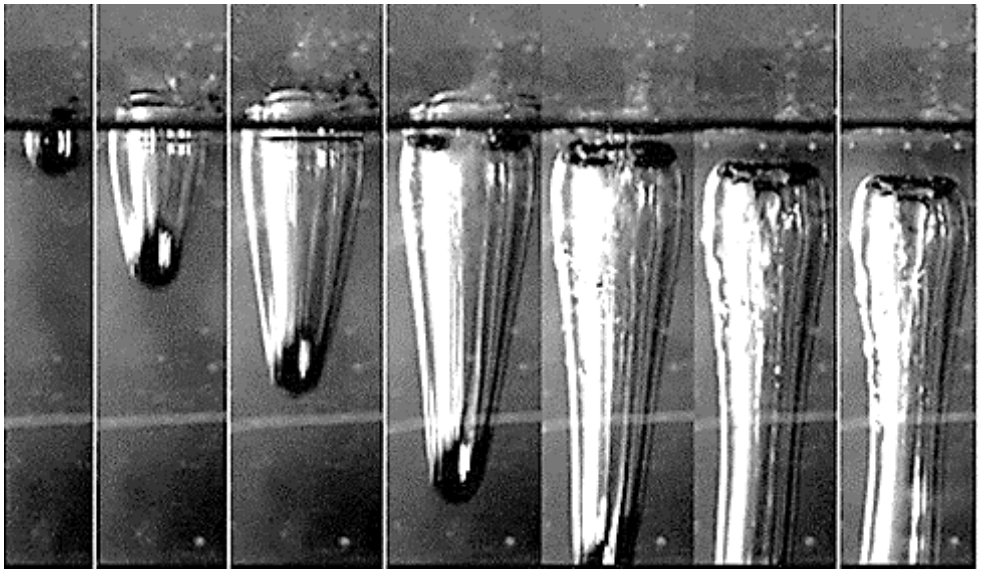

Figure 36: Cavity formation behind a ‘sunflower oil-coated’ steel sphere (D = 10mm, u_i = 5.94m/s) that submerged in sunflower oil. The time difference between each successive image is 4ms. Surface seal occurred about 12ms after sphere entry while the unusual shallow seal did not occur completely.

A noticeable difference can be observed when comparing Figure 36 with Figures 28 to 30. In Figure 36, subsequent to surface seal, a clear layer of oil can be seen separating the top of the cavity from the oil surface while the cavity was being pushed downwards further into the oil. However, in Figures 28 to 30, the top of the main cavity appeared to have a much thinner secondary cavity connecting it to the surface while it was being pulled downwards by the sphere. Shallow seal occurred when these two sections of the same cavity split.

By reproducing phenomena consistent with those documented in existing literature with ‘oily spheres’, it can be concluded that the unusual phenomena documented earlier in this chapter indeed resulted from the surface conditions of the impacting steel spheres.

Similar experiments were also performed using rapeseed oil and grapeseed oil. The unusual phenomena were also observed during these experiments. Therefore, it can be concluded that those phenomena are not unique to sunflower oil.

5.6. Discussion and Conclusion

Worthington [2-4] and May [8] studied the effects and influence of surface conditions of the impacting solid body on cavity formation following liquid entry. It is understood that surface conditions will determine the transition velocity, above which a significant cavity will be generated. Duclaux *et al.* [30] observed that above the transition velocity, no significant difference exists between the shapes of cavities generated by hydrophilic and hydrophobic spheres. Meanwhile, Truscott *et al.* [16] showed that surface conditions have negligible impact on the dynamics of these cavities.

Earlier in this chapter, it is documented that phenomena not consistent with the present literature and current understanding were observed subsequent to steel spheres entering into sunflower oil and the two-layer, sunflower oil-water system. Although the phenomena can be reproduced from experiments performed under the same conditions, due to the uncertainties and difficulties of effectively quantifying the required experimental conditions, the measurements obtained from the unusual phenomena have not been analysed in further detail.

Upon further investigation, it was found that these unusual phenomena were caused by the surface conditions of the impacting spheres since they were not observed when the same experiments were repeated with ‘oily spheres’. The existence of the unusual phenomena, however, demonstrated the substantial influence surface

conditions of a solid body and the upper layer liquid in a two-layer liquid system could have on cavity dynamics that is not previously understood or documented in the present literature.

It goes against intuition that solid bodies with high impact velocities will produce little or no cavity while generating significant cavities at relatively lower velocities. Hence it is hypothesised that the unusual phenomena may be part of a transition phase where significant cavities would be produced once again should the spheres exceed another critical velocity. However, further experiments will be required to verify this hypothesis.

Chapter 6: Deep seal dynamics

''All thy works shall praise thee, O LORD; and thy saints shall bless thee.''

------ Psalm 145:10, KJV

6.1. Introduction

A solid body that has sufficient velocity and appropriate surface conditions, will generate a significant cavity at its wake while submerging in water or any other single-phase, homogeneous liquid. This cavity will initially expand and thenceforth experience deep seal as shown in Figure 37.

Meanwhile, experiments have revealed that deep seal will also occur in qualitatively similar form following entries of solid bodies into two-layer, oil-water systems. In Figure 38, a steel sphere entered into a two-layer, oil-water system which comprised of a thin layer of viscous silicone oil (ν_o = 1000mm^2/s) resting on the surface of a deep pool of water. A cavity was generated a cavity as the sphere passed through the thin oil layer. It continued to expand into water until the instant of deep seal.

However, there are two main differences between the cavities shown in Figures 37 and 38. Firstly, the cavity shown in Figure 38 was enveloped by a thin oil film which was itself dragged into the water by both the sphere and the downward expansion of the cavity. This oil film coating will be visualised and shown in Figure 62 in Chapter 8.2.3 by means of Laser-induced fluorescence (LIF) experiments. Secondly, as documented in Chapter 4.3, ripples were observed to form along the walls

of the cavity shown in Figure 38 such that the cavity walls were no longer smooth. The origins and dynamics of these ripples will be studied and discussed in Chapter 8.

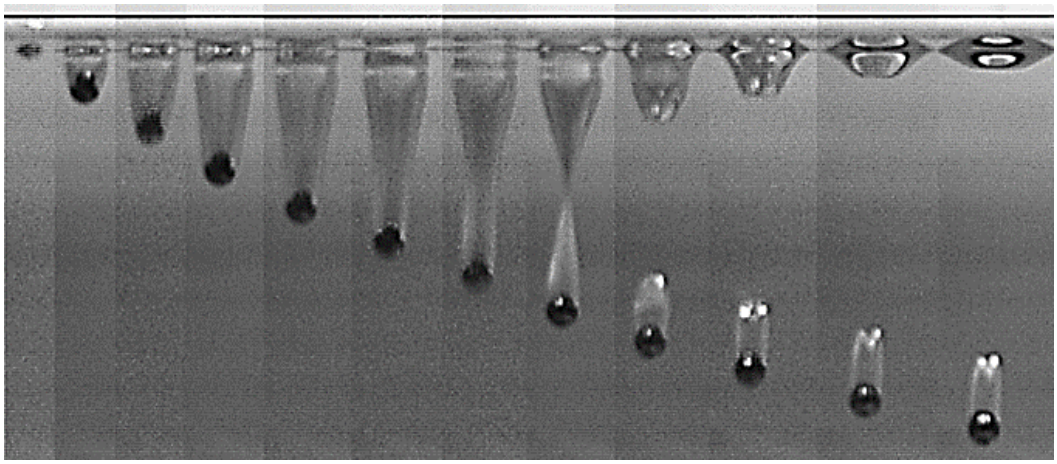

Figure 37: Entry of a steel sphere (D = 7mm and u_i = 2.42m/s) into sunflower oil. The time difference between each successive image is 5ms. A cavity was generated at the wake of the sphere following its liquid entry and deep seal occurred about 35ms after entry.

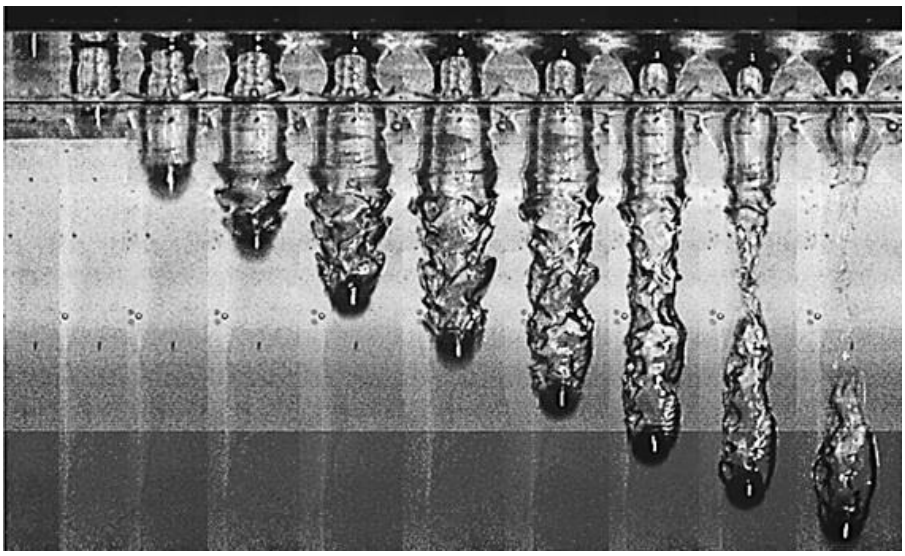

Figure 38: Entry of a steel sphere (D = 8mm, u_i = 3.43m/s) into a two-layer system consisting of a 12.5mm layer of silicone oil (ν_o = 1000mm^2/s) resting on the water surface. The time difference between each successive image is 5ms and deep seal occurred approximately 40ms following sphere entry.

6.2. Definitions of the characteristic quantities associated with deep seal

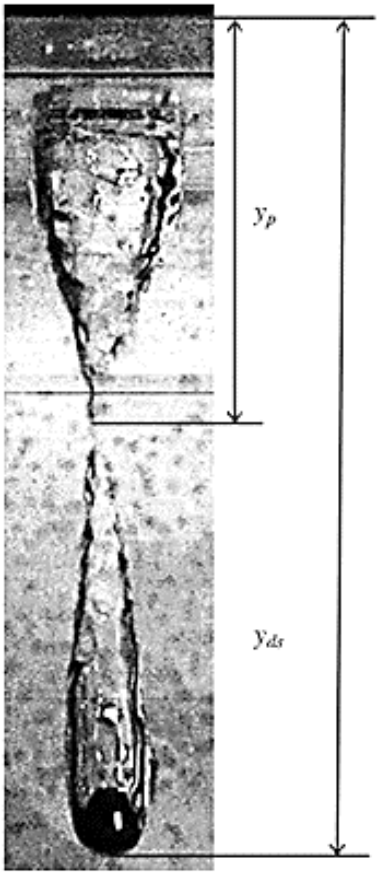

Figure 39: Deep seal: The process whereby the cavity splits in two at a certain depth under the surface. The photo shown is for a 5mm layer of sunflower oil resting on the water surface and the sphere had diameter, D = 8mm and impact velocity, u_i = 2.43m/s. Figure from Tan *et al.* [7], reprinted with permission. © Cambridge University Press 2016.

Figure 39 presents the physical qualities that will be studied in detail in this chapter. The pinch-off depth, y_p, is defined as the displacement from the liquid surface (as opposed to the oil-water interface in the two-layer, oil-water systems) to the point where the cavity split into two. On the other hand, the deep seal depth, y_{ds}, is defined as the displacement from the same liquid surface to the bottom tip of the sphere at the

instant of deep seal. The time interval between the instant when the sphere impinged on the liquid surface and the instant of deep seal is defined as the deep seal time, t_{ds}.

In order to assess experiments involving two-layer liquid systems in the context of studies documented in existing literatures, y_p, y_{ds} and t_{ds} for entries of spheres into single-phase, homogeneous liquids were initially quantified and analysed. Thereafter the study was extended to obtain and analyse corresponding experimental data for spheres entering into stratified two-layer, oil-water systems.

6.3. Deep seal time, t_{ds}

6.3.1. Single-phase homogeneous liquid

Figure 40 presents t_{ds} as a function of u_i obtained from experiments involving steel spheres entering into sunflower oil. It can be observed that for spheres that had the same diameter, t_{ds} remained constant despite an increase in u_i. This observation indicates that t_{ds} did not depend on u_i and was consistent with corresponding water entry results from the present literature [15, 36]. Both t_{ds} and u_i were subsequently non-dimensionalised to form the dimensionless deep seal time, $t_{ds}^* = u_i\, t_{ds}/D$ and the Froude number, $Fr = u_i\, (gD)^{-0.5}$ respectively. Figure 41 presents the relationship between these two dimensionless qualities.

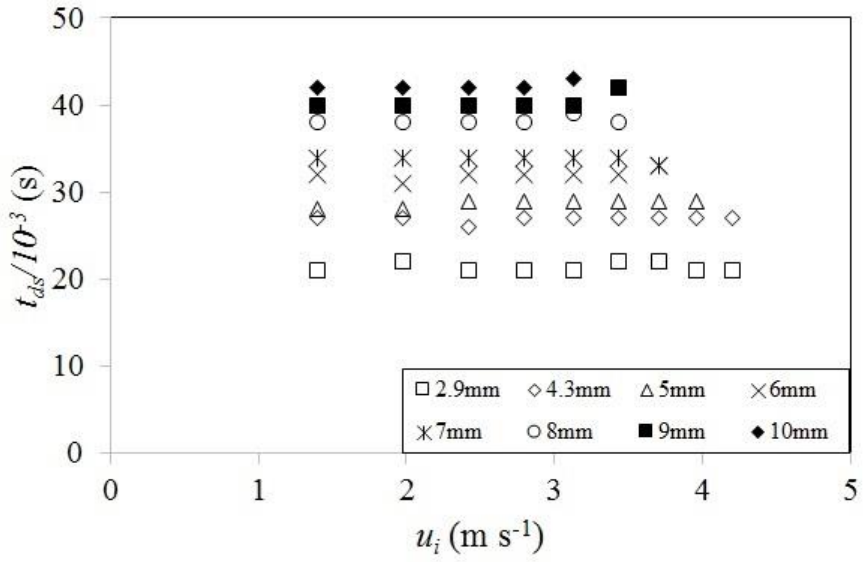

Figure 40: The deep seal time, t_{ds} as a function of impact velocities, u_i for steel spheres of various diameters entering into sunflower oil. It can be observed that t_{ds} is constant for a given diameter of the sphere despite increasing u_i.

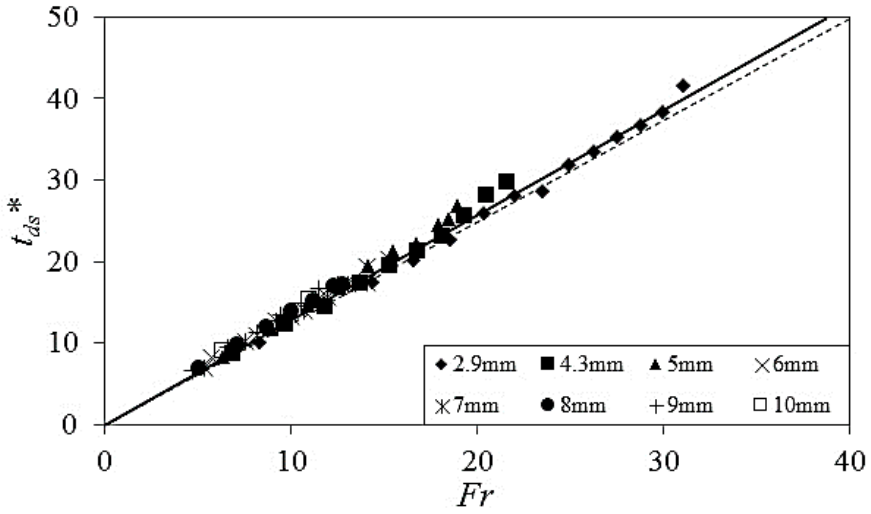

Figure 41: Dimensionless deep seal time, t_{ds}* as a function of the Froude number, Fr, for spheres of different diameter D (see legend). The continuous line present experimental data for sunflower oil, linear best fit, t_{ds}* = 1.27 Fr; while the dashed line present results for water from Truscott & Techet [15], t_{ds}* = 1.25 Fr. Figure from Tan *et al.* [7], reprinted with permission. © Cambridge University Press 2016.

Figure 41 displays a comparison of the dimensionless deep seal time, t_{ds}* as a function of Froude number, *Fr* between the sunflower oil entry results obtained from the present study and the corresponding water entry results documented in Truscott *et al.* [15]. The figure also reveals that the results from Truscott *et al.* [15] can be reproduced for sunflower oil with very high accuracy. The gradients *a* of the linear least-squares fit t_{ds}* = *a Fr* in Figure 41 are *a* = 1.27 (shown by the continuous line) for sunflower oil and *a* = 1.25 (shown by the dashed line) for water [15].

Meanwhile, the corresponding data for t_{ds} obtained from silicone oil (ν_o = 1000mm^2/s) which has a viscosity nearly twenty times that of sunflower oil and a thousand times that of water, produced the gradient *a* = 1.3. Despite the large differences in viscosity, the three values of *a* are approximately equal and the reason for this will be addressed in Chapter 6.8.

Truscott & Techet [15] had shown that the relationship t_{ds}* = 1.25 *Fr* is independent of the rotation, velocity and density of the sphere. The present experiments further showed that the same relationship for spheres entering into single-phase, homogeneous liquids is also independent of the viscosity and surface tension of the liquid.

6.3.2. Two-layer liquid systems

Figure 42 presents the deep seal time, t_{ds} as a function of the impact velocity, u_i for steel spheres of various diameters that entered into a deep pool of water filled with a thin layer of viscous silicone oil (ν_o = 1000mm^2/s). The thickness, *d* of the silicone oil layer varied between 5mm and 15mm.

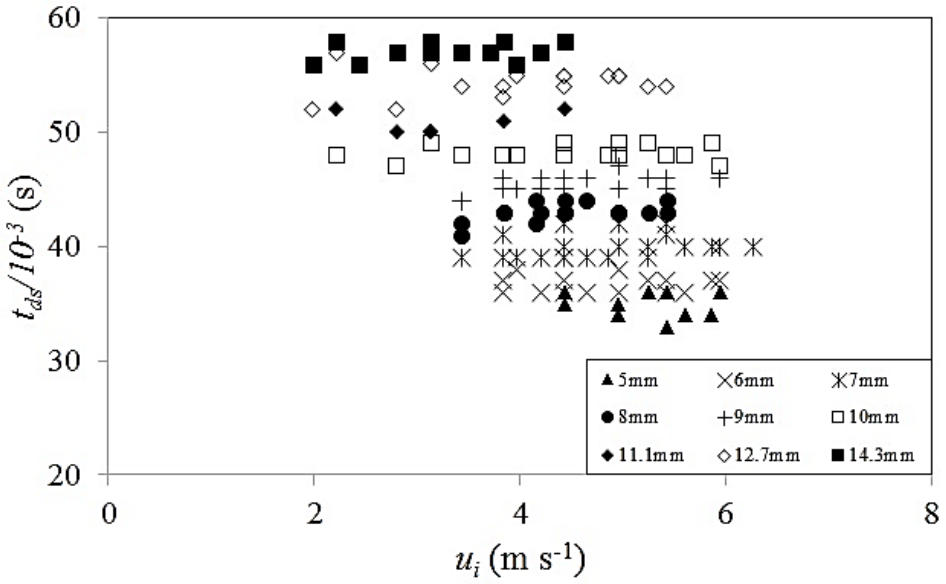

Figure 42: Deep seal time, t_{ds} as a function of the impact velocity, u_i for steel spheres entering into water that had a thin silicone oil ($\nu_o = 1000 mm^2/s$) layer with thickness, d varying between 5mm and 15mm. The diameter of the spheres is shown in the legend.

Despite the presence of a thin layer of silicone oil with thickness, d varying between 5mm and 15mm, Figure 42 shows that for spheres that had the same diameter, the deep seal time, t_{ds} was also independent of u_i and d. Both t_{ds} and u_i were likewise non-dimensionalised to form the dimensionless deep seal time, $t_{ds}^* = u_i t_{ds}/D$ and the Froude number, $Fr = u_i (gD)^{-0.5}$.

Figure 43 compares experimental data points for t_{ds}^* obtained from the two-layer, silicone oil-water system to the results for single-phase, homogeneous liquids from Figure 41.

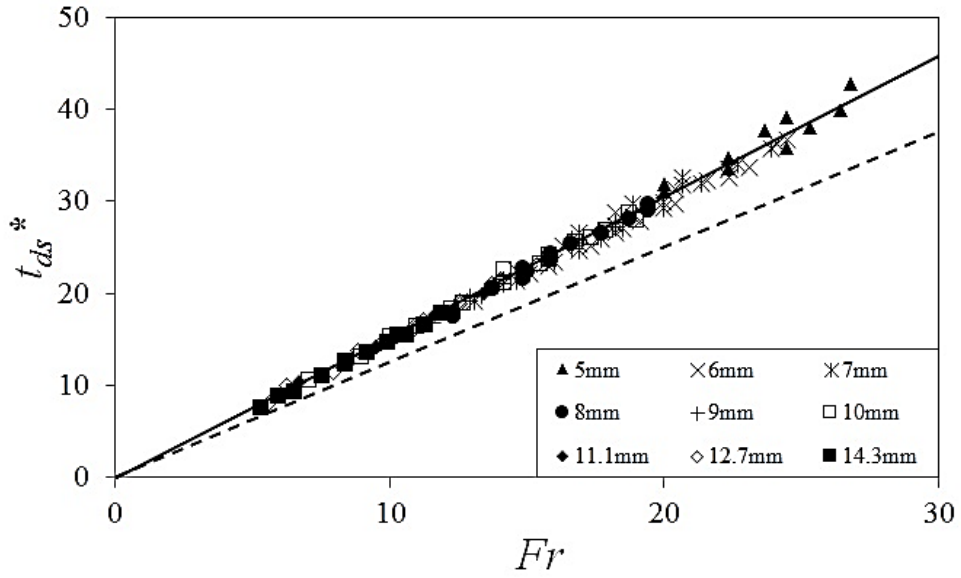

Figure 43: Dimensionless deep seal time, t_{ds}* as a function of the Froude number, *Fr* for steel sphere entry into a two-layer system of silicone oil above water. The thin layer of silicone oil had thickness varying between 5mm and 15mm. The dashed line represents results for water entry from Truscott & Techet [15] from Figure 41 where t_{ds}* = 1.25 *Fr*.

The dashed line in Figure 43 represents the results of Truscott & Techet [15] discussed in the context of Figure 41. The data displayed in the figure reveal that there exists a substantial difference between the data for the single-phase homogeneous liquids and the corresponding data for the two-layer, silicone oil-water system. The line of least-squares fit (solid line) interpolating the data for the two-layer system in Figure 43 reveals a gradient of a = 1.53. Meanwhile, the corresponding result obtained for the two-layer, sunflower oil-water system reveals a gradient of a = 1.55 as shown in Figure 44. It should be noted that for the experiments involving sunflower oil, the thickness of the oil layer was constant at d = 5mm while that for silicone oil included data from a number of different layer thickness between 5mm and 15mm.

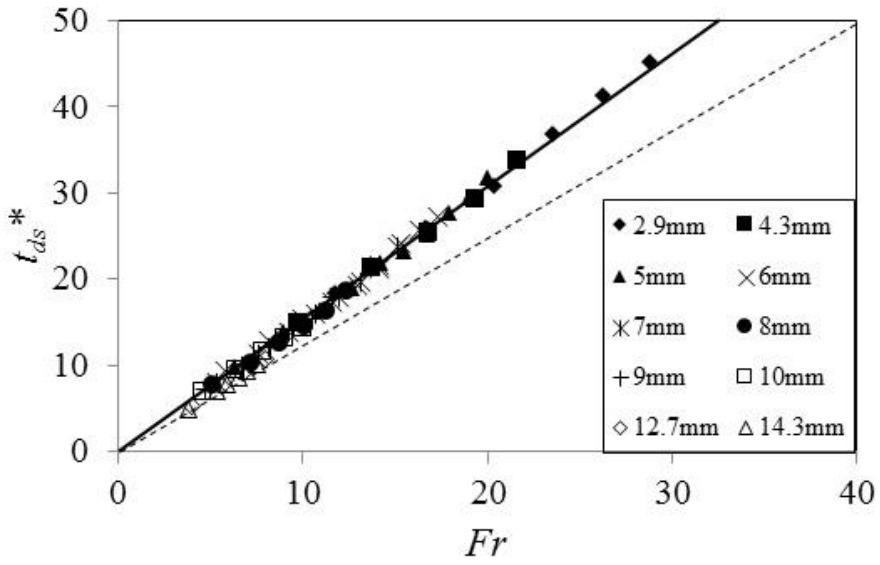

Figure 44: Dimensionless deep seal time, t_{ds}* for spheres entering water that had a 5mm layer of sunflower oil resting on the water surface. The dashed line represents result for water entry from Truscott & Techet [15] where t_{ds}* = 1.25 *Fr*. Figure from Tan *et al.* [7], reprinted with permission. © Cambridge University Press 2016.

As the gradients *a* obtained for both two-layer systems are approximately equal, it can be concluded that the relationship t_{ds}* ≈ 1.54 *Fr* generally exists for two-layer, oil-water systems. The results further suggests that t_{ds} is also independent of the viscosity and surface tension of the thin oil layer and the oil-water interfacial tension.

In summary, the cavity generated by spheres in two-layer liquid systems will remain open for approximately 23% longer than that generated in single-phase, homogeneous liquids. This prolonged opening can be attributed to the presence of the thin oil layer resting atop the water. However, it is worth highlighting that the ratio of the sphere diameter to the oil layer thickness, *D*/*d* was approximately between 0.2 and 3. It is hypothesised that if *D* >> *d*, the relationship between t_{ds}* and *Fr* would be very similar to that of a single-phase, homogeneous liquid. The main argument for this hypothesis is that in such circumstances, the oil layer thickness will be insignificant

compared to the size of the generated cavity, and consequently will have negligible impact on the dynamics of solid-liquid impacts.

6.4. Deep seal depth, y_{ds}

As illustrated in Figure 39 in Chapter 6.2, the deep seal depth, y_{ds} is defined as the displacement of the bottom tip of the sphere with respect to the liquid surface at the instant of deep seal. It should be noted that for measurements related to two-layer, oil-water systems, the point of reference is the surface of the oil and not the oil-water interface.

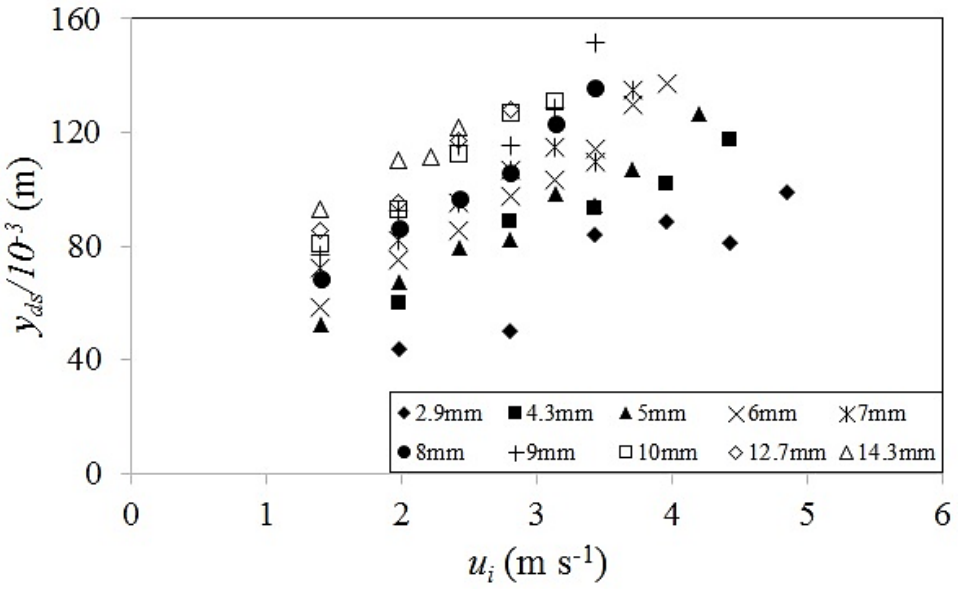

Figure 45: Deep seal depth, y_{ds} as a function of impact velocity, u_i for spheres of various diameters entering a two-layer, sunflower oil-water system. The thickness of the sunflower oil layer was d = 5mm.

Figure 45 presents the measurements of deep seal depths, y_{ds} for entries of steel spheres into a two-layer, oil-water system that consisted of a 5mm sunflower oil layer resting on a deep pool of water. The graph demonstrates the existence of a relationship

between y_{ds}, u_i and the sphere diameter, D. The data for y_{ds} was subsequently non-dimensionalised to form the dimensionless deep seal depth, $y_{ds}^* = y_{ds}/D$ and presented as a function of the Froude number, Fr as shown in Figure 46.

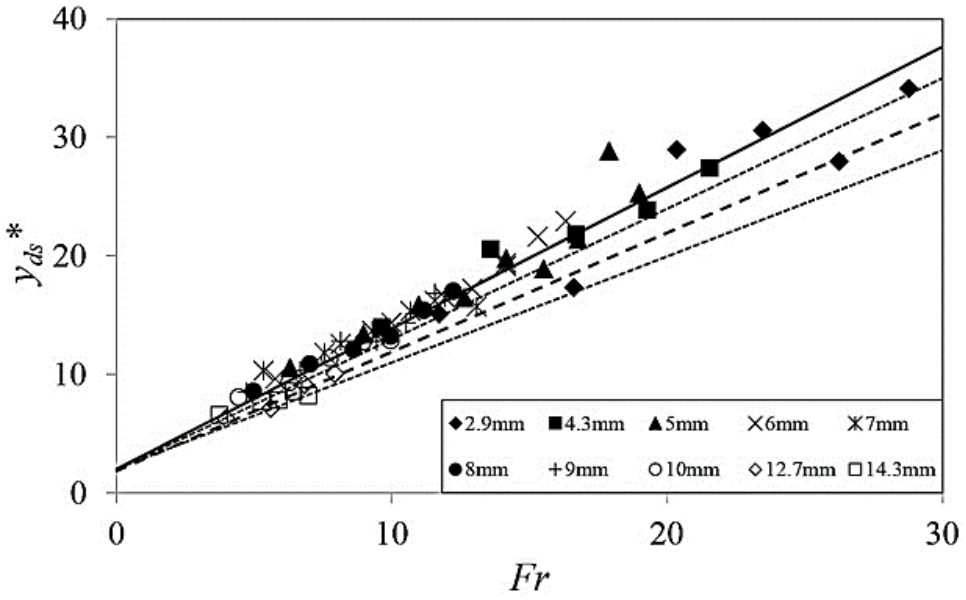

Figure 46: Dimensionless deep seal depth, y_{ds}^* as a function of the Froude number, Fr for spheres of different diameters (see legend). The continuous line and the data points represent the two-layer, sunflower oil-water system where $y_{ds}^*/Fr \approx 1.18$. The dashed line represents data taken from Figure 13 (c) of Truscott & Techet [15] where $y_{ds}^*/Fr \approx 1.0$ while the dotted lines estimated the maximum error bounds from the same data. Figure from Tan *et al.* [7], reprinted with permission. © Cambridge University Press 2016.

Figure 46 displays a comparison between the dimensionless deep seal depth, $y_{ds}^* = y_{ds}/D$ for the same two-layer, sunflower oil-water system and that for water as documented in Truscott & Techet [15]. The lines in Figure 46 representing the data of Truscott & Techet [15] were reproduced for the data points for steel spheres from Figure 13 (c) in their paper and the estimate for the maximum error included reflects the approximate scatter of the data points in that figure.

Figure 46 reveals that, similar to Figure 44, a significant difference exists beyond the extent of the maximum error margin, between the data for the two-layer, oil-water system and that of water (single phase system) of Truscott & Techet [15] for the deep seal depth. A linear least-squares fit $y_{ds}^* = c\,Fr$ revealed a gradient of c = 1.18 for the two-layer system. However, one could obtain from Figure 13 (d) of Truscott & Techet [15], a gradient of approximately c = 1.0 for water. The fitting gradient obtained for the data of the two-layer system which involved a 5mm layer of a much higher viscosity (ν_o = 1000 mm^2/s) of silicone oil on water was c = 0.9.

6.5. Dimensionless deep seal velocity, u_{ds}^*

Using the definitions for the dimensionless deep seal time, t_{ds}^* and the dimensionless deep seal depth, y_{ds}^* in addition to linear data interpolations in Figures 41, 43, 44 and 46, one obtains $c/a = \langle u_{ds} \rangle / u_i$ where $\langle u_{ds} \rangle = y_{ds}/t_{ds}$ is the mean sphere velocity within the liquids to the instant of deep seal. The mean deep seal velocity can be non-dimensionalised to form the dimensionless deep seal velocity, $u_{ds}^* = \langle u_{ds} \rangle / u_i = y_{ds}^*/t_{ds}^* = c/a$. A summary of the results computed in the present study is shown in Figure 47.

Fluid	t_{ds}^*	y_{ds}^*	u_{ds}^*
Water	1.25	1	0.8
5mm Sunflower oil on water	1.55	1.18	0.76
5mm Silicone oil on water	1.53	0.9	0.59
Sunflower oil	1.27	0.62	0.49
Silicone oil	1.3	0.26	0.2

Figure 47: A summary of t_{ds}^*, y_{ds}^* and u_{ds}^* computed for the various fluids in the present study.

In single-phase, homogeneous liquids, the dimensionless deep seal velocity, u_{ds}* decreased with increasing viscosity, suggesting an increase in drag experienced by the spheres. Such observation is consistent with the present theory (drag coefficient curve) which suggests that the drag coefficient will be higher at lower Reynolds number (higher viscosity).

Meanwhile, for the two-layer, oil-water systems, the oil films acquired by the spheres increased the drag forces they experienced while descending within the deep pool of water. Furthermore, the mean deep seal velocity of the spheres also decreased with an increase in viscosity of the oil layer covering them.

6.6. Presence of additional drag & deep seal velocity, u_{ds}

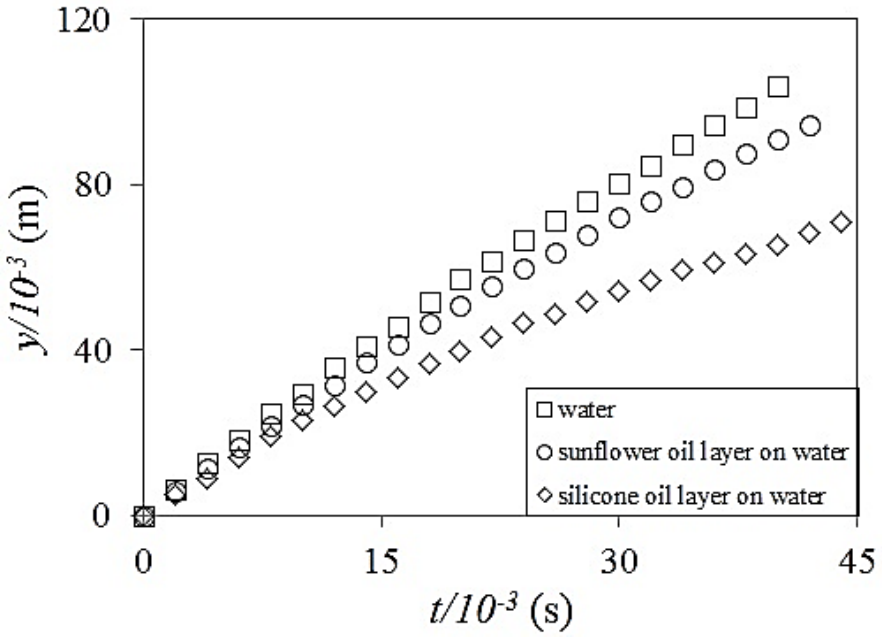

Figure 48: The depth of the steel spheres, y with respect to time, t following their water entry or passage through the oil-water interface (for cases involving two-layer, oil-water systems). The data are for steel spheres with diameter, D = 5mm and impact velocity, u_i = 3.2m/s.

Figure 48 provides a direct verification of the conclusion that the oil film covering the spheres resulted in an increased drag force. The figure presents a comparison of the depths of steel spheres, y with respect to time, t subsequent to the spheres entering into water or passing through the oil-water interface (for cases involving the two-layer, oil-water systems). All the steel spheres had the same diameter, D = 5mm and impact velocity, u_i = 3.2m/s. The two-layer liquid systems were water that had a 5mm layer of either sunflower oil or viscous silicone oil (ν_o = 1000mm^2/s) resting on its surface. It can be observed from the figure that the deviation of the data of '*sunflower oil layer on water*' from those of '*water*' is relatively small compared to the difference between '*silicone oil layer on water*' and '*water*'.

Figure 49 presents a comparison of y between two steel spheres of different diameters (D = 5mm and 14.3mm) with respect to time, t following their entries into water and a two-layer, oil-water system that consisted of a 5mm layer of silicone oil (ν_o = 1000mm^2/s) resting on the water. Similarly as in Figure 48, the points of reference where y = 0 and t = 0 were the water surface and oil-water interface for water entry and two-layer, oil-water system entry data respectively. The steel spheres had the same impact velocity, u_i = 3.2m/s and represented the smallest and largest spheres used in experiments involving the aforementioned viscous silicone oil.

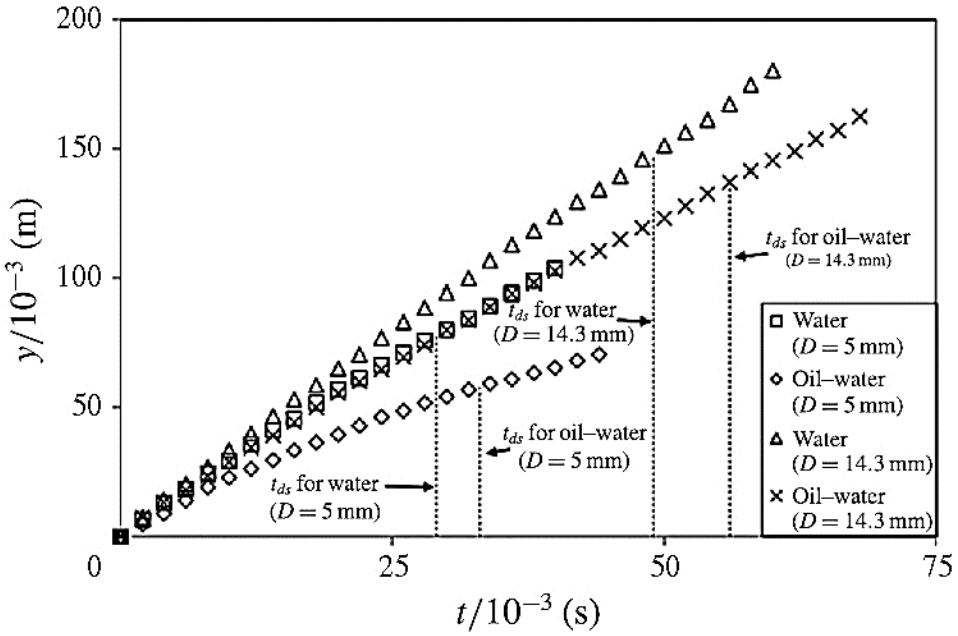

Figure 49: The depth of the steel spheres, y with respect to time following water entry or passage through the oil-water interface, t. The spheres entered the liquids at u_i = 3.2m/s and their diameters could be seen in the legend. The dotted lines represent the deep seal time, t_{ds} for the spheres. Figure from Tan *et al.* [7], reprinted with permission. © Cambridge University Press 2016.

It can be observed from Figure 49 that even in water entry experiments, there existed a difference in y at any given time, t between the smallest and largest spheres despite both having the same impact velocity. This observation demonstrates that the drag force was more significant to the dynamics of the smaller sphere. In addition, this difference in y between the smallest and largest spheres was also significantly larger in the two-layer, oil-water system entry experiments at any given time.

The deep seal velocity, u_{ds} as opposed to the mean deep seal velocity, $<u_{ds}>$ mentioned in Chapter 6.5 is the actual sphere velocity at the instant of deep seal. It can be calculated by taking the average of the rate of change of depth, dy/dt for several points on the figure around the deep seal time, t_{ds}. Therefore, for spheres that entered

into water, one obtains u_{ds} = 2.2m/s for the smallest sphere (D = 5mm) and u_{ds} = 2.82m/s for the largest sphere (D = 14.3mm), representing 69% and 88% of the impact velocity, u_i, respectively. When the same procedure was repeated for spheres that entered into the two-layer, oil-water system, one obtains u_{ds} = 1.15m/s for the smallest sphere and u_{ds} = 2.22m/s for the largest sphere, accounting for 36% and 70% of u_i, respectively. The observation of a decrease in deep seal velocity in the presence of an additional oil layer is consistent with the data of the dimensionless deep seal velocity calculated in Chapter 6.5. The drag coefficients of the four spheres studied by Figure 49 will be quantified in Chapter 7.2.

6.7. Pinch-off depth, y_p

The results from the previous sections have shown that the presence of a thin sunflower oil layer increased the deep seal depth, y_{ds} and deep seal time, t_{ds} while simultaneously decreased the deep seal velocity, u_{ds} of the sphere. This suggests that the pinch-off depth, y_p shown in Figure 39 in Chapter 6.2 must have also been increased by the presence of the aforementioned sunflower oil layer. However, y_p was not quantitatively considered in the present literature relevant to the discussion in the previous sections. Howbeit y_p was measured for the purpose of a consistency check. The data for y_p was non-dimensionalised similarly as y_{ds} in Chapter 6.4, forming the dimensionless pinch-off depth, $y_p^* = y_p/D$. This dimensionless quantity is shown in Figure 50 in comparison to the data interpolations for the deep seal depth, y_{ds} discussed in connection to Figure 46.

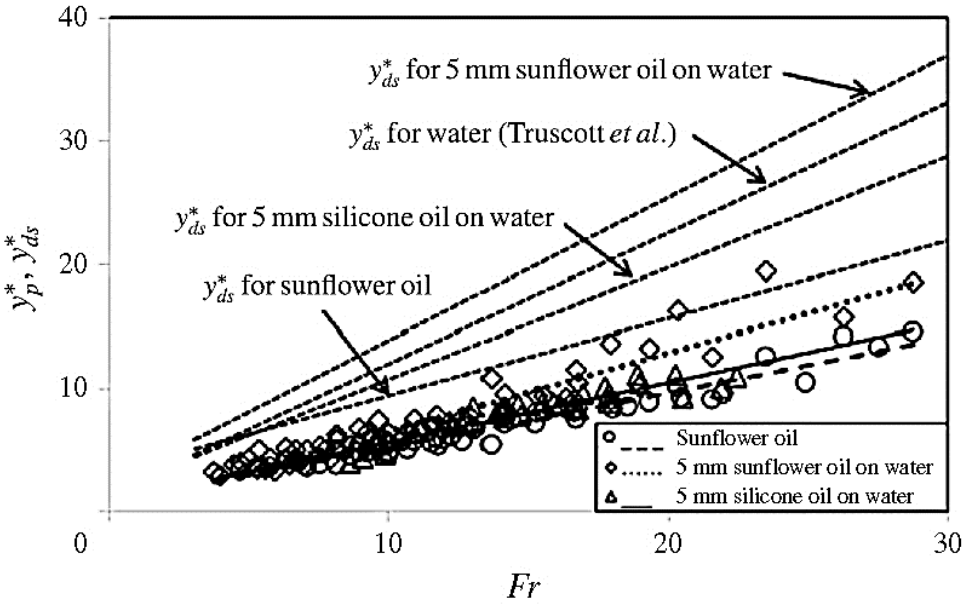

Figure 50: Dimensionless pinch-off depth, y_p* as a function of the Froude number and comparison to the data interpolations for the dimensionless deep seal depth, y_{ds}* discussed in Chapter 6.4. Figure from Tan *et al.* [7], reprinted with permission. © Cambridge University Press 2016.

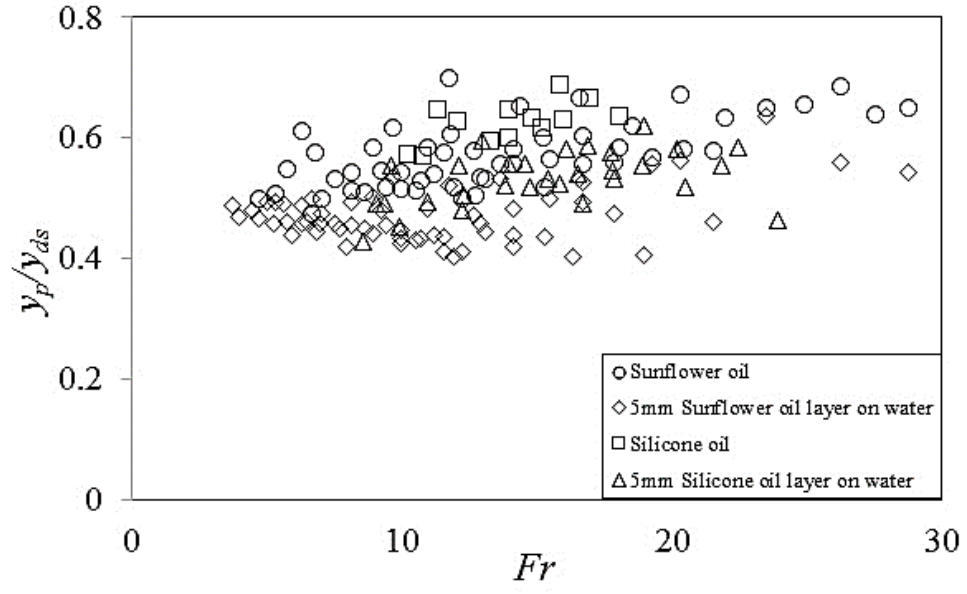

Figure 51: The ratio y_p/y_{ds} of pinch-off depth to deep seal depth as a function of the Froude number, *Fr*. Figure from Tan *et al.* [7], reprinted with permission. © Cambridge University Press 2016.

The data points in Figure 50 are consistent with the results from the discussion of Figure 46 as they show y_p increasing with the Froude number, *Fr*. The data also reveal that the rate of increase of y_p was comparable to the corresponding increase rates for y_{ds}. Moreover, a comparison between the three sets of data points for y_p in Figure 50 shows the existence of a small but consistent trend for the data for the two-layer systems to be slightly higher than the data for the homogeneous sunflower oil.

Figure 51 displays the experimental data for the ratio of pinch-off depth to deep seal depth, y_p/y_{ds} as a function of the Froude number, *Fr*. The figure presents all data lying within the range $0.4 < y_p/y_{ds} < 0.7$ and independent of *Fr*. Their mean values, $\langle y_p/y_{ds} \rangle$, associated standard deviation, *s* and the gradients *m* for the least-squares interpolations $y_p/y_{ds} = m\,Fr$ are summarised in Figure 52.

Fluid	$\langle y_p/y_{ds} \rangle$ +/- *s*	*m*
Sunflower oil	0.57 +/- 0.06	0.002
5mm Sunflower oil on water	0.47 +/- 0.04	0.006
Silicone oil	0.64 +/- 0.05	0.009
5mm Silicone oil on water	0.53 +/- 0.05	0.005
Mean	0.53 +/- 0.07	0.006

Figure 52: A summary of $\langle y_p/y_{ds} \rangle$, *s* and *m* computed for the various fluids in the present study.

The mean values of $\langle y_p/y_{ds} \rangle$ presented in Figure 52 for the various fluids used in the present study support the theoretical result $1/3 < y_p/y_{ds} < 1/2$ from Duclaux *et al.*[30]. In addition, they are also very similar to those obtained by Marston *et al.* [40] for their experiments involving Leidenfrost spheres.

6.8. Discussion

Truscott & Techet [15] commented that the non-dimensional deep seal time as defined and used in their paper was '*a less than ideal scaling parameter*' because the '*initial impact velocity dominates for both the x- and y-axes*'. Thereafter they related and expressed their main results to the alternative non-dimensional time, $\tau = t_{ds}(2g/D)^{0.5}$ as defined by Glasheen *et al.* [36].

In Chapter 6.3, the same definition, $t_{ds}^* = u_i\, t_{ds}/D$ documented in Truscott & Techet [15] was being used to provide direct comparisons of Figures 41, 43 and 44 with the relevant parts of Figure 13 in their paper. In addition, the overall conclusions were not affected since the associated values for τ were obtained from the gradients k of all straight lines, $t_{ds}^* = k\, Fr$ in Figures 41, 42 and 44 by $\tau = k\,\sqrt{2}$. However, the issue of the proper non-dimensionalisation for the deep seal time, t_{ds} which were neither expressed in Truscott & Techet [15] nor in Glasheen *et al.* [36] will be further discussed.

The results $t_{ds}^* = 1.25\, Fr$ of Truscott & Techet [15] or more generally the observation that t_{ds}^* is directly proportional to Fr in Figure 41, shows that the deep seal time, $t_{ds} = 1.25\,(D/g)^{0.5}$. This relationship demonstrates that t_{ds} is independent of the impact velocity, u_i of the spheres. Hence the timescale $(D/g)^{0.5}$ or $(D/2g)^{0.5}$ as used in Glasheen *et al.* [36] would naturally be a more suitable choice for non-dimensionalising t_{ds} as compared to using u_i/D. In addition, this option of non-dimensionalisation can indeed also be justified on the basis of physical arguments.

It is reasonable to expect that the collapse dynamics of the cavity behind the sphere are not affected by the impact velocity, u_i if it is much higher than the velocity

scale associated with the cavity collapse itself. This is the case for the impacts considered in the present experiments and also in Truscott & Techet [15]. The common timescale associated with cavity collapse is $(D/g)^{0.5}$ which apart from the factor $\sqrt{(1/2)}$, is the same timescale used by Glasheen *et al.* [36]. The velocity scale associated with cavity collapse is $u_c = D\ (D/g)^{-0.5} = (Dg)^{0.5}$ which for the present experiments, had values of u_c = 0.3m/s for spheres with diameters in the order of millimetres and u_i between 1.4m/s and 6m/s. Meanwhile, the data of Truscott & Techet [15] were obtained using steel spheres with a diameter, D = 1'' (25.4mm) where u_c = 0.5m/s at u_i between 1.9m/s and 9.9m/s. Therefore, in both studies $u_c < u_i$, supporting the option $(D/g)^{0.5}$ as the timescale for the non-dimensionalisation of t_{ds} in future studies. In the opposite limit where $u_i << u_c$ or equivalently when the release height of the sphere approaches zero, splashing and cavity formation would stop fully. However it is possible that some unobserved phenomena may exist near $u_i \approx u_c$ when the Weber number is small and surface tension effects are important.

Replacing $t_{ds}^* = u_i\ t_{ds}/D$ by the alternative choice of $\tau = t_{ds}\ (D/g)^{-0.5}$ would, however, also necessitate to remove u_i from the non-dimensionalisation process. The new appropriate scaling would be provided by $Re_c = D\ u_c/\nu$ instead of Fr, representing a Reynolds number associated with the cavity collapse which for the present experiments had values between 400 and 5200. These relatively high values of Re_c would probably be the reason that the dimensionless deep seal time t_{ds}^* for the homogeneous liquids was independent of their viscosity as shown in Figure 41. The deep seal time only increased slightly with the liquid viscosity as is expressed by the very slightly increasing values of the fitting gradient a discussed in connection with the figure.

Chapter 7: Sphere dynamics

''I can do all things through Christ which strengtheneth me.''

------ Philippians 4:13, KJV

7.1. Introduction

Following its entry into water, a rigid sphere will experience resistance forces such as drag, surface tension and buoyancy forces as it continues its downward motion under the influence of gravity. The movement of the sphere results in the displacement of water and as the sphere accelerates, a certain mass of water will also appear to be accelerated. This phenomenon introduces an added mass (or alternatively known as virtual mass) component that is being described in the present literature, for instance, May [9].

Taking downwards as positive, the balance of forces experienced by a rigid sphere moving in water can be expressed as follows:

$$(m_s + m_a)\, a_s = F_g - F_B - F_D - F_T \qquad (7a)$$

In equation (7a) above, m_s and a_s represent the mass and acceleration of the sphere while m_a is the added mass. Meanwhile, F_B, F_D, F_T and F_g are buoyancy, drag, surface tension force and the weight of the sphere respectively. The surface tension force, F_T is neglected in the following calculations as it accounts for approximately less than 5% of the drag, F_D in the present experiments, making its impact insignificant and negligible in the present study.

For reasons of convenience and simplicity, the sphere is assumed to be completely immersed in the water in the subsequent calculations. Hence the buoyancy, F_B as defined by Archimedes' principle will be $F_B = F_g\ (\rho_w/\rho_s)$ where ρ_w and ρ_s are the densities of water and the steel sphere used in the present study respectively. Hence the mass of the water displaced, $m_w = m_s\ (\rho_w/\rho_s)$. Despite the generation of cavities will vary F_B, the assumption is still used in all subsequent calculations for reasons of convenience. Meanwhile, the added mass for a sphere as defined by the present literature [17] is $m_a = 0.5\ m_w$. Therefore, equation (7a) can be simplified as follows:

$$\left(1 + \frac{\rho_w}{2\ \rho_s}\right)\ m_s\ a_s = \left(1 - \frac{\rho_w}{\rho_s}\right) m_s\ g - \frac{1}{2}\ \rho_w\ C_D\ A\ u^2$$

In the above equation, g, C_D, A and u represent the gravitational acceleration, drag coefficient, area and instantaneous velocity respectively. The terms are rearranged to make a_s the subject as follows:

$$a_s = \frac{1 - \frac{\rho_w}{\rho_s}\ g}{1 + \frac{\rho_w}{2\ \rho_s}} - \frac{\rho_w\ C_D\ A\ u^2}{2\ m_s\ (1 + \frac{\rho_w}{2\ \rho_s})}$$

Substituting $m_s = (1/6)\ \pi\ D^3 \rho_s$ and $A = (1/4)\ \pi\ D^2$ where D is the sphere diameter, the equation becomes:

$$a_s = \frac{1 - \frac{\rho_w}{\rho_s}\ g}{1 + \frac{\rho_w}{2\ \rho_s}} - \left(\frac{3}{4\ D}\right)\left(\frac{\frac{\rho_w}{\rho_s}\ C_D\ u^2}{1 + \frac{\rho_w}{2\ \rho_s}}\right)$$

Substituting the relevant values for densities of water and steel and simplifying the equation, the acceleration, a_s of steel spheres moving in water in the present study can be written as:

$$a_s = 0.819\, g - \frac{0.0904\, C_D\, u^2}{D} \qquad (7b)$$

As the spheres generated cavities at their wakes, not all their surfaces had physical contact with water. Therefore, the drag, F_D they experienced and their drag coefficient, C_D would consequently be reduced. Such phenomenon is reminiscent of the production of bubbles under the hulls of ships and the supercavitation of underwater missiles that reduce energy loss resulting from drag. The reduction of C_D will be measured and discussed in Chapter 7.2.

Equation (7b) shows that the instantaneous acceleration of the sphere, a_s is dependent on both its diameter, D and instantaneous velocity, u. The inverse relationship between acceleration and diameter is best demonstrated in Figure 49 in Chapter 6.6. It can be observed from that figure that the larger sphere (D = 14.3mm) travelled a larger displacement as compared to the smaller sphere (D = 5mm) at any given time despite having the same impact velocity.

Meanwhile, the instantaneous velocity of the sphere, u_{n+1} at time t_{n+1} where $\delta t = (t_{n+1} - t_n)$ can be calculated using simple kinematics as shown:

$$u_{n+1} = u_n + a_n\, \delta t$$

From here, one can calculate the instantaneous displacement, y_{n+1} at time t_{n+1} by using a simple kinematics equation as follows:

$$y_{n+1} = y_n + 0.5\,(u_n + u_{n+1})\,\delta t \qquad (7c)$$

7.2. Drag coefficients of the spheres, C_D

A theoretical displacement-time graph can be computed using equation (7c) when one substitutes an appropriate value for the drag coefficient, C_D into equation (7b). Assuming the value of C_D to remain constant, C_D can be found by 'trial and error' when one endeavours fitting the theoretical displacement-time graph to the displacement-time graph obtained by experiments. An example of this method is shown in Figure 53.

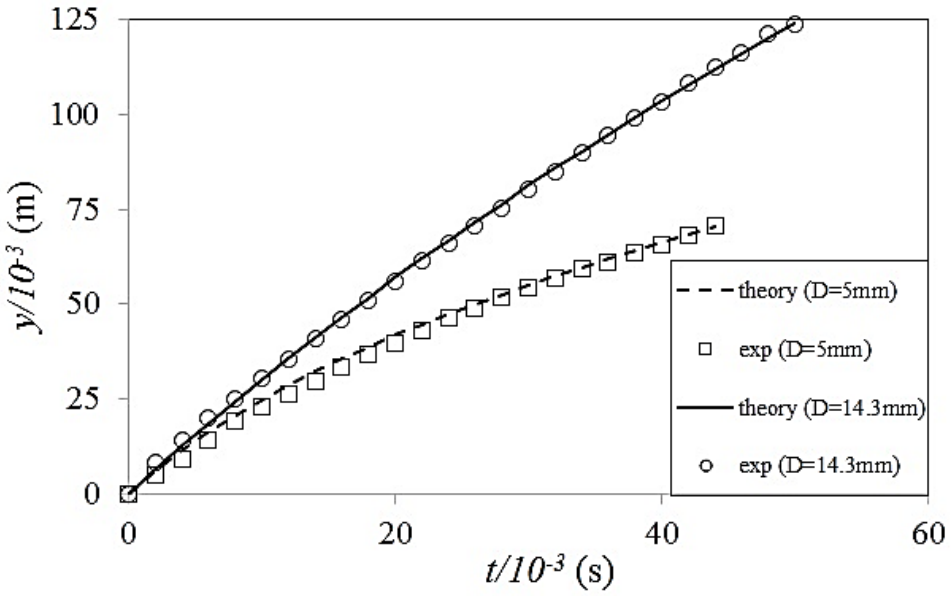

Figure 53: The fitting of the theoretical displacement-time graph to the experimental data taken from Figure 49.

Figure 53 presents data for the entries of steel spheres into a two-layer, oil-water system that consisted of a 5mm layer of silicone oil (ν_o = 1000mm^2/s) resting on water. The experimental data are the corresponding data taken from Figure 49 in Chapter 6.6 where the spheres had diameters, D of 5mm and 14.3mm and common

impact velocity, u_i = 3.2m/s. By fitting theoretical data points to the figure, the drag coefficient is found to be C_D = 1.05 and C_D = 0.79 for the 5mm and 14.3mm spheres respectively.

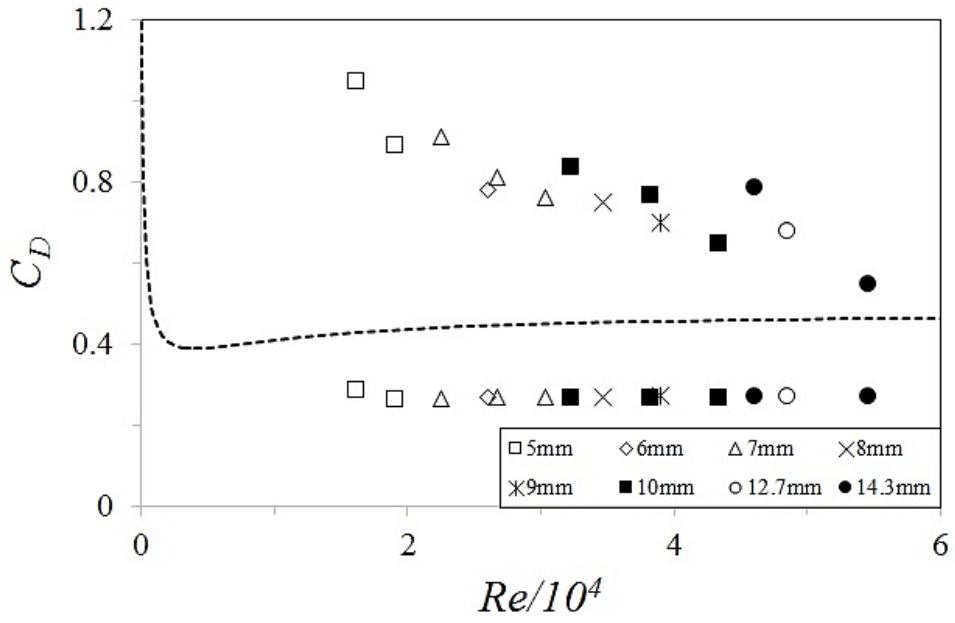

Figure 54: Drag coefficient, C_D as a function of the impact Reynolds number, $Re = u_i D/\nu_w$ where ν_w is the kinematic viscosity of water. The dashed line represents the standard drag coefficient of a sphere in a homogeneous liquid calculated using equation (19) in Brown & Lawler [49]. The data points below the dashed line represents data for spheres in water with cavities at their wakes while the data points above the dashed line are those for spheres that had passed through a 5mm layer of high viscosity silicone oil (ν_o = 1000mm^2/s) prior to entering water also with cavities at their wakes. Figure from Tan *et al.* [7], reprinted with permission. © Cambridge University Press 2016.

Figure 54 presents a summary of all available data from experiments for the drag coefficients of spheres entering into water directly and those that passed through a 5mm silicone oil layer (ν_o = 1000mm^2/s) prior to entering into the water directly underneath. These data are compared with the standard drag data for spheres in a

homogeneous liquid calculated using equation (19) of Brown & Lawler [49] where $C_D = (24/Re)\,(1 + 0.15\,Re^{0.681}) + [0.407/(1 + 8710/Re)]$. Using the impact velocity, u_i and the kinematic viscosity of water ($\nu_w = 1\text{mm}^2/\text{s}$) for calculations, the Reynolds number, $Re = u_i D/\nu_w$ would be between 15,000 and 55,000 for the present experiments. Hence for this range of Reynolds number, one expects the corresponding drag coefficients to be between 0.4 and 0.5 as represented by the dashed line.

The data points below the dashed line are those for spheres that entered into water directly but generated cavities at their wakes. It can be observed that they are in the range of $0.25 < C_D < 0.3$, showing a reduction of 30% to 40% of drag experienced by spheres that do not generate a cavity. The drag, F_D and therefore, the drag coefficient, C_D are dependent on the amount of surface area of the spheres that are in contact with the liquid and given that the cavity dynamics are similar [30], it is estimated that the air cavities covered about 30% to 40% of the sphere surfaces.

Meanwhile, the data points above the dashed line are for spheres entering into a two-layer, oil-water system that consisted of a thin 5mm layer of silicone oil ($\nu_o = 1000\text{mm}^2/\text{s}$) resting on the water. However, it should be noted that the spheres in these cases also generated cavities at their wakes. As a consequence of their passages through the oil layer, the spheres and their cavities would have been coated with a thin oil film.

It can be interpreted from the figure that the larger the sphere, the less influence the oil layer and oil coating have on its motion. On the other hand, for a given sphere diameter, a higher impact velocity will also result in a lower C_D. This observation can be explained that at higher impact velocities, the spheres spend less time passing through the oil layer and consequently acquiring thinner oil coatings, resulting in lower

amount of drag being added by the oil. Therefore, with Reynolds number being a function of both the sphere diameter and impact velocity, it is reasonable that an increase in Reynolds number will lead to a decrease in drag coefficient as shown in Figure 54.

Note that the deceleration of the spheres between their impact with the liquid surface and the instant of deep seal, suggests that the data for deep seal time and deep seal depth in Chapter 6 cannot scale with the Froude number alone. Due to the observed deceleration there must exist an additional scaling with the ratio of sphere density, ρ_b to liquid density, ρ_l, which only vanishes in the limit $\rho_b/\rho_l \rightarrow \infty$. This issue is also addressed in Bergmann *et al.* [39] who used impactors rigidly mounted to a motor-actuated mechanism to enforce a constant, controllable speed in their experiments investigating the impact of a disk on a water surface.

7.3. Dynamics during 'interface-trapped'

As described in Chapter 4.2, 'interface-trapped' is the phenomenon where the sphere settles along the oil-water interface as shown graphically in Figure 55.

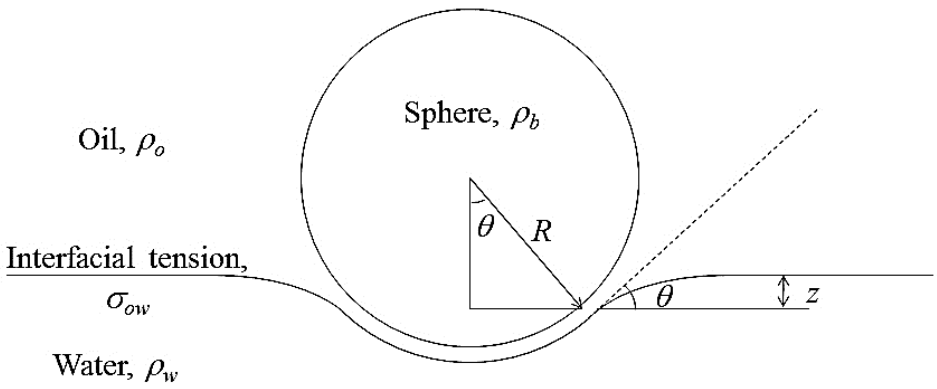

Figure 55: A rigid sphere at a dynamic equilibrium position at an oil-water interface.

A force balance on the rigid sphere of density, ρ_b and radius, R shown in Figure 55 can hence be expressed as follows:

$$(\rho_b - \rho_o)\left(\frac{4\,\pi\,R^3}{3} - V_{sc}\right) g + (\rho_b - \rho_w)\, V_{sc}\, g$$

$$= 2\,\pi\,R\,\sigma_{ow}\sin^2\theta + (\rho_w - \rho_o)\, g\, z\, R^2 \sin^2\theta$$

Where V_{sc} is the volume of the spherical cap which can be calculated as follows:

$$V_{sc} = \frac{\pi}{6}\,(R - R\cos\theta)\,(3R^2\sin^2\theta + \{R - R\cos\theta\}^2)$$

Which upon simplification becomes:

$$V_{sc} = \left(\frac{\pi\,R^3}{3}\right)(2 - 3\cos\theta + \cos^3\theta)$$

For 'interface-trapped' to occur, the weight of the sphere, F_g must not exceed the maximum combined force of buoyancy, F_B and interfacial tension, F_T. Hence by balancing $F_g = F_B + F_T$ (where $F_B = (1/6)\,\pi\,D^3\rho_w\,g$ and $F_T = \pi\,D\,\sigma_{ow}$) and rearranging the terms, the maximum diameter a steel sphere can have while generating 'interface-trapped' can be simplified and expressed as follows:

$$D = \sqrt{\frac{6\,\sigma_{ow}}{(\rho_s - \rho_w)g}}$$

Upon substituting the appropriate values and σ_{ow} = 0.0429N/m (interfacial tension between silicone oil and water), it is found that $D \approx$ 2mm. As the smallest steel sphere used in the experiments had diameter, D = 2.9mm, it is reasonable that

'interface-trapped' was not observed with steel spheres in the present study as documented in Chapter 4.5.

7.4. Dynamics during 'tailing' and 'transition'

As described in Chapters 4.2 and 4.4, both the 'tailing' and 'transition' phenomena involve the sphere dragging an 'oil tail' into water subsequent to it passing through the upper oil layer and the oil-water interface. The two phenomena can be distinguished by the presence of a relatively small cavity that attaches to the sphere during 'transition'. Examples of the 'tailing' and 'transition' phenomena are shown in Figures 12 and 17 respectively.

Meanwhile, the terminal velocity, u_t of the sphere moving in a liquid can be theoretically determined by balancing its weight by the buoyancy force and steady-state drag it experiences. This will result in no net force and consequently $a_s = 0$. Hence the theoretical terminal velocity can be expressed and calculated as follows:

$$u_t = \sqrt{\frac{\left(\frac{4}{3}\right)\left(\frac{\rho_{sphere}}{\rho_{liquid}} - 1\right) g\ D}{C_D}}$$

Figures 56 presents the non-dimensional velocity, u/u_i as a function of non-dimensional depth, y/D relative to the oil-water interface for a sphere that experienced 'tailing'. The two-layer, oil-water system consisted of a 12.5mm layer of silicone oil (ν_o = 1000mm^2/s) resting on the surface of a deep pool of water. After determining the relevant Reynolds numbers, the corresponding drag coefficients, C_D obtained from equation (19) of Brown & Lawler [49] were used to calculate the theoretical terminal velocity, u_t. Therefore, the dashed line and solid line in the figure represent the

theoretical terminal velocities of the sphere should it move in pure silicone oil and water, respectively.

It can be observed from Figure 56 that the sphere decelerated rapidly before reaching a terminal velocity that was lower than its theoretical terminal velocity in water (solid line) but higher than its theoretical terminal velocity in silicone oil (dashed line). As the sphere was covered with a silicone oil film that had a density lower than itself, its apparent density was lower than its true density. Therefore, the sphere reached a lower terminal velocity as compared to the scenario where it moved in water without first passing through an oil layer.

Meanwhile, Figure 57 presents a corresponding graph for a slightly larger sphere that experienced 'transition' after entering into the same two-layer, silicone oil-water system with the same impact velocity, u_i as in Figure 56. It can be observed that the terminal velocity reached by the sphere in Figure 57 was closer to its theoretical terminal velocity in water (solid line), demonstrating the oil layer had less influenced on the sphere dynamics as compared to in Figure 56. This can be attributed to the reduction of drag by higher inertia (higher Re and lower C_D according to the drag coefficient curve) and the presence of a cavity.

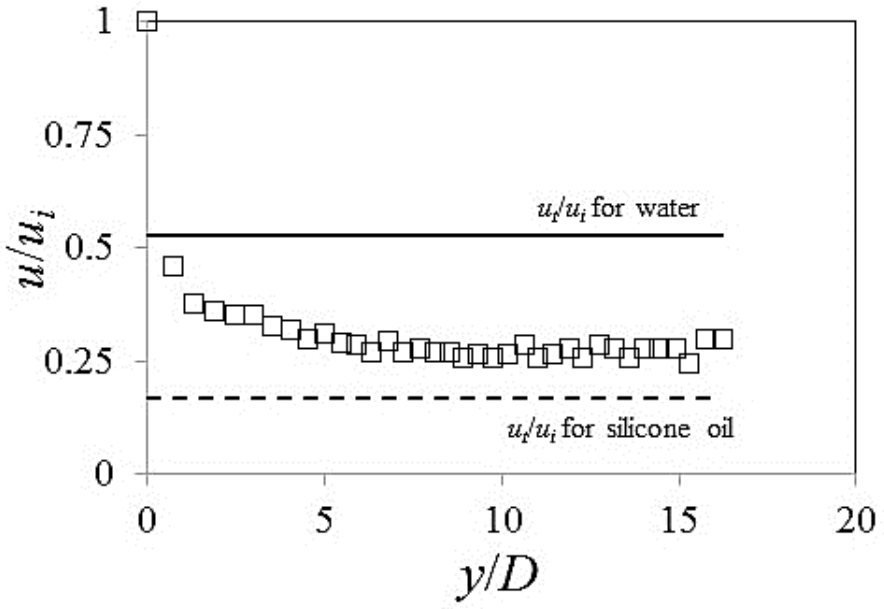

Figure 56: Non-dimensional velocity of a sphere as a function of its non-dimensional depth relative to the oil-water interface for a sphere experiencing the 'tailing' phenomenon. The sphere had diameter, D = 5mm and impact velocity, u_i = 1.98m/s.

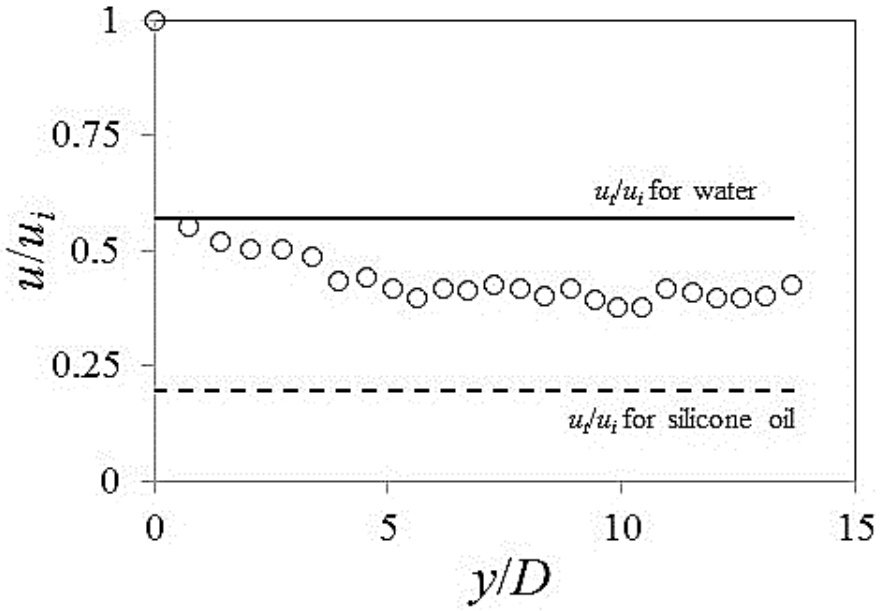

Figure 57: Non-dimensional velocity of a sphere as a function of its non-dimensional depth relative to the oil-water interface for a sphere experiencing the 'transition' phenomenon. The sphere had diameter, D = 6mm and impact velocity, u_i = 1.98m/s.

7.5. Discussion

The ‘trial and error’ method of fitting the theoretical displacement-time graph to the one obtained by experiments as described in Chapter 7.2 has its limitations while determining the values of the drag coefficients, C_D.

Firstly, the method assumes C_D to be constant. As the sphere velocity and the Reynolds number, *Re* changes, C_D will also consequently change. This change is not significant for experiments involving spheres that enter into water directly without first passing through an oil layer. However, for a sphere that enters into the two-layer, oil-water system, the increase in drag is a consequence of the oil film coating it acquired while passing through the oil layer. As the sphere moves further into the water, the oil film coating will naturally become thinner in the process, reducing the amount of drag it adds to the sphere which in turn, results in a decrease in C_D. Moreover, the volume of the air cavity and the surface area of the sphere that have physical contact with the sphere also changes with respect to time, further varying and adding uncertainty to the value of C_D.

Secondly, due to the limitations of the high-speed camera, it was only possible to accurately measure the displacements of the spheres for up to about 100ms following their liquid entries. Hence the displacement-time graphs generated from these measurements for the ‘trial and error’ fitting can only provide a general understanding of the motions of the spheres subsequent to their entries into the liquids studied. Consequently, the C_D derived from the fittings represent the average C_D of the spheres immediately after their liquid entries. As discussed above, for spheres entering the two-layer, liquid system, C_D will gradually decrease as their oil coatings become thinner.

Thirdly, the buoyancy, F_B component in the formula used to compute C_D involves the assumption that the sphere be completely immersed in the water for reasons of convenience. However, in reality, cavities were often being generated and the value of F_B would have varied slightly, which in turn would also have resulted in a variation of the value of C_D.

Meanwhile, there also exists a clear connection between the generation of cavities and the reduction of C_D as drag is dependent on the amount of surface area of the spheres that have physical contact with the liquids involved. Hence C_D for spheres that have cavities at their wakes are 30% to 40% lower than that for spheres that do not have a cavity. It should be noted that in the present study, all spheres entering into the two-layer, oil-water system generated cavities at their wakes. It is not exactly clear at the point of writing, the extent the presence of the thin oil layer and the oil film coatings acquired by the spheres have on the generation of cavities. Therefore, it will be difficult to quantify the exact amount of drag added by the oil film coatings on the spheres that generated cavities behind them.

Chapter 8: Ripple dynamics

''Praise ye the LORD: for it is good to sing praises unto our God; for it is pleasant; and praise is comely.''

------ Psalm 147:1, KJV

8.1. Introduction

The formation of wave-like structures (referred to as ripples) along the otherwise smooth cavity walls found at the wakes of rigid spheres that enter into two-layer, oil-water systems is a major discovery documented in the thesis. These ripples are the defining features of the 'transition' and 'rippling' phenomena described in Chapter 4 and are shown again in Figure 58.

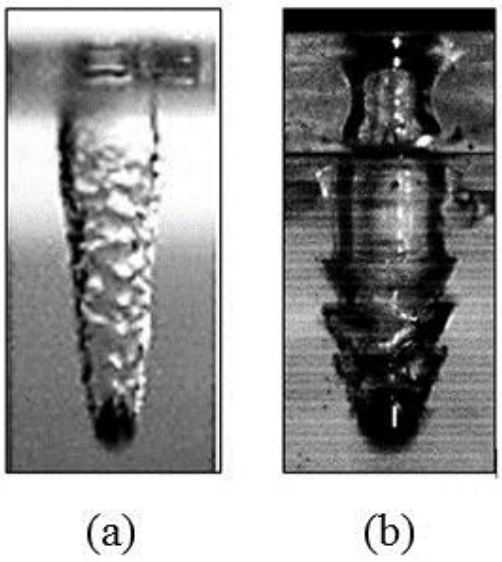

Figure 58: The wave-like structures or ripples observed forming along cavity walls subsequent to spheres entering into two-layer, oil-water systems: (a): sunflower oil (ν_o = 54.4mm^2/s) - water, (b): silicone oil (ν_o = 1000mm^2/s) – water.

As documented in Chapter 4.3 and shown in Figure 58, the ripples were more obvious, well-defined and quantifiable when a liquid of higher viscosity was being used as the upper layer. This is the main reason the more viscous silicone oil shown in (b) was used to 'create' the ripples that were to be quantified and analysed later in this chapter. Moreover, it can also be observed that the ripples would only begin forming at a certain depth under the oil-water interface and above which, the cavity walls remained smooth.

8.2. The origins of the ripples

''*What causes the ripples?*'' is a common question one would ask after seeing pictures of the ripples. Hence in an attempt to provide a hypothesis for the origins of the ripples, several additional experiments were performed and the resulting observations analysed.

8.2.1. Entry into mixture of miscible liquids

In order to verify that the formation of ripples only occurred in two-layer systems of immiscible liquids, experiments involving the same steel spheres entering into a mixture of methanol (CH_3OH) and water were performed. Prior to the release of the spheres, the methanol was dyed blue to make it visible to the eye, after which it was spread evenly so that it formed a clear and uniform 5mm layer resting on the water surface.

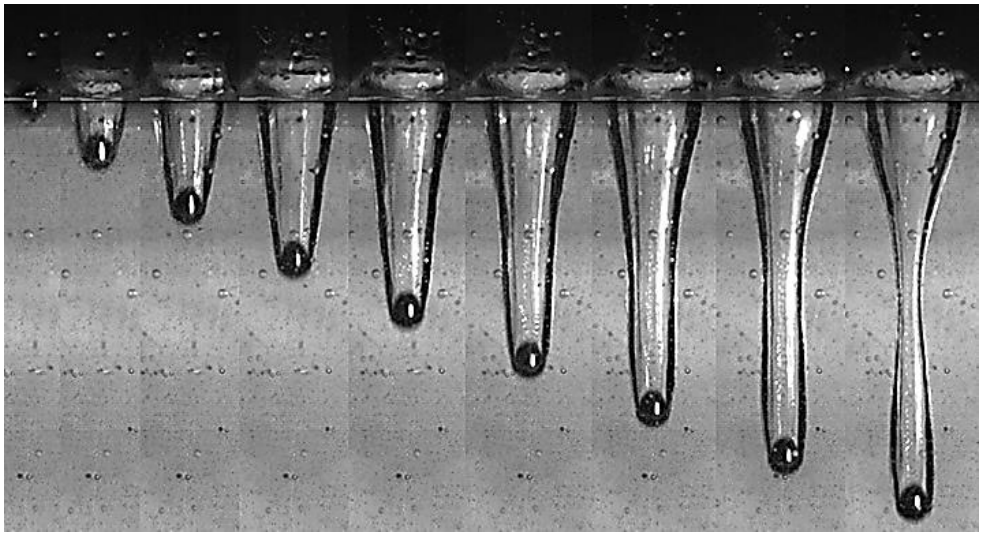

Figure 59: Cavity formation following the entry of a steel sphere (D = 10mm and u_i = 3.13m/s) into water that had a 5mm layer of methanol resting on its surface. The cavity was identical to that formed after a sphere enters into a single-phase, homogeneous liquid. Due to the colour settings of the camera, the blue methanol layer is not visible in the pictures. The time difference between each successive image is 5ms.

Figure 59 presents the cavity formation subsequent to a steel sphere entering into a mixture of miscible liquids that comprised of a 5mm methanol layer resting on the surface of a deep pool of water. Due to the colour settings of the camera, the blue methanol layer is not visible in the figure.

The appearance and growth of the cavity were almost identical to that generated by spheres entering into single-phase, homogeneous liquids. Meanwhile, cavity sealing phenomena such as deep seal and surface seal also occurred. Most significantly, it can be observed from the figure that the cavity walls remained smooth throughout the images. Hence it can be concluded that the ripples do not occur in entries involving mixtures of miscible liquids.

8.2.2. Entry into water with and without oil film coating

The next investigation was to verify the influence the oil films coating the spheres would have on ripple formations. Therefore, experiments involving entries into water by steel spheres with and without an oil film coating were performed. These spheres had the same diameter, D = 8mm and were released from the same height, h = 0.8m thus ensuring equal impact velocity, u_i = 3.96m/s and Froude number, Fr = 14.1.

In the first experiment, the sphere was immersed in silicone oil before being briefly cleaned by a tissue paper. Therefore, it had a greasy surface but without any obvious or significant oil film. In order to avoid confusion, this sphere is referred to as the ‘greasy sphere’.

Meanwhile, similar to the first experiment, the preparation for the second experiment also involved immersing the sphere into the same silicone oil. However, in contrast to the first experiment, the sphere was not cleaned by a tissue paper. Therefore, the same sphere had a significant oil film coating it and is referred to as the ‘oil-layered sphere’.

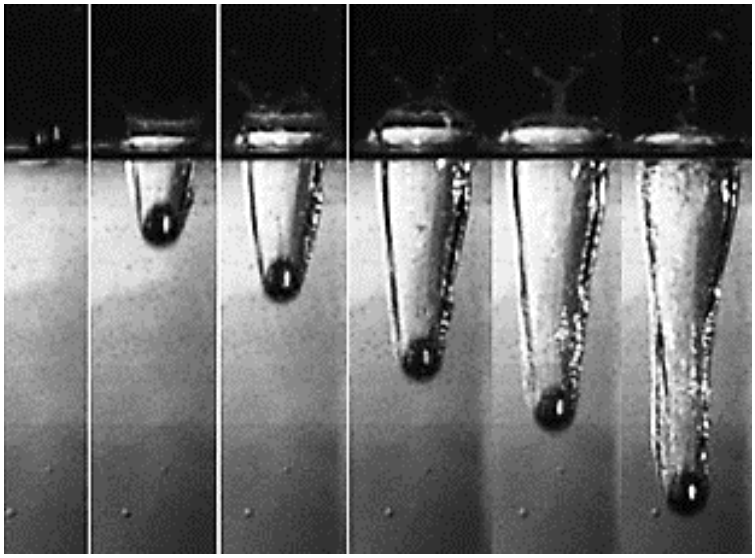

Figure 60: Cavity formation by a 'greasy sphere' following its entry into water. The cavity walls were relatively smooth, reminiscent of water entry by a hydrophobic sphere. The time difference between each successive image is 5ms. Figure from Tan *et al.* [7], reprinted with permission. © Cambridge University Press 2016.

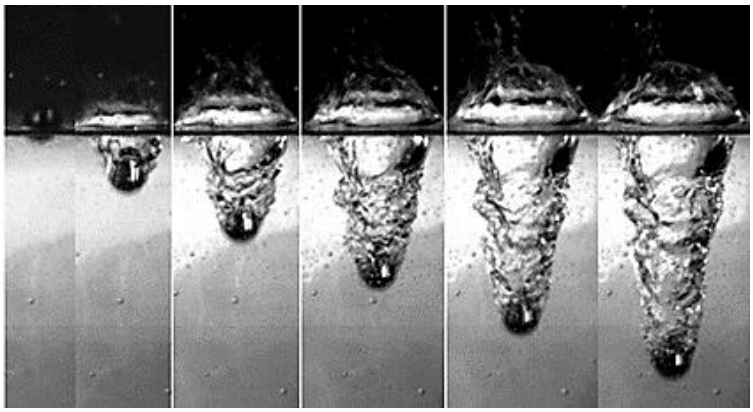

Figure 61: Cavity formation by an ‘oil-layered sphere' following its entry into water. Wave-like instability can be observed forming along the cavity walls. Interestingly, the wave-like instability was also observed to form below a depth under the surface of water, above which the cavity walls remained smooth. The time difference between each successive image is 5ms. Figure from Tan *et al.* [7], reprinted with permission. © Cambridge University Press 2016.

Figures 60 and 61 present pictures of cavity formation by a ‘greasy sphere’ and an ‘oil-layered sphere’ respectively. It can be observed from the figures that a stark difference existed between the appearances of the two cavities.

In Figure 60, the walls of the cavity generated at the wake of the ‘greasy sphere’ was observed to be almost smooth, reminiscent of the pictures of cavities generated by hydrophobic spheres found in the present literature.

However, in contrast to the ‘greasy sphere’, Figure 61 shows that the cavity generated by the ‘oil-layered sphere’ displayed wave-like structures. These structures resembled the ripples observed following entries of spheres into two-layer, oil-water systems described earlier in this chapter and also in Chapter 4. Similar to those ripples, the wave-like structures observed in Figure 61 also only began forming below a certain depth under the surface of water, above which the cavity walls remained smooth.

Therefore, from these experiments and comparisons, it can be concluded that the thin oil film coatings acquired by the spheres and their cavities as they pass through the oil layer, will have a significant influence on ripple formation.

8.2.3. Laser-induced fluorescence (LIF)

A laser-induced fluorescence (LIF) experiment was performed to further verify that the spheres and their cavities were indeed coated with thin oil films following their passages through the oil layer. In the LIF experiment, the silicone oil layer was being dyed with a fluorescent dye. A vertical laser light sheet was subsequently aligned to coincide with the impact plane of the sphere, allowing the illumination of the oil film.

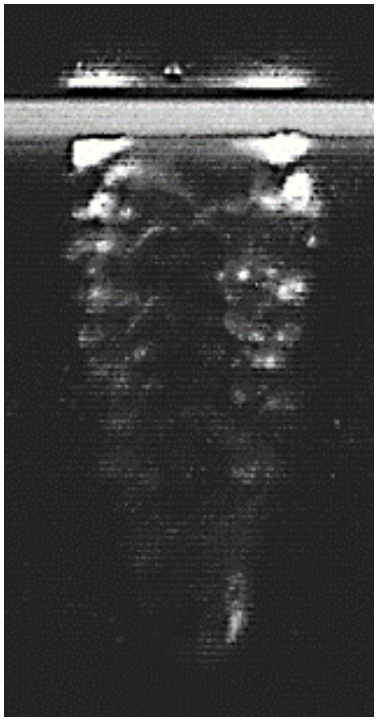

Figure 62: Laser-induced fluorescence (LIF) visualisation of the cavity behind the steel sphere. The bright illuminated areas on the cavity walls originate from the dyed silicone oil film coating the sphere acquired as a result of its passage through the oil layer which is being shown as a bright horizontal line. Hence this picture supports the hypothesis that the formation of ripples is influenced by the acquired oil film coating. Figure from Tan *et al.* [7], reprinted with permission.

Figure 62 presents a LIF visualisation of the cavity generated at the wake of a steel sphere after the sphere had passed through the oil layer. The bright thick horizontal line near the top of the figure is the dyed silicone oil layer that was resting on the water surface. The existence of an oil film around the cavity with wave-like instability can be clearly seen from the figure. Therefore, the same figure further supports the hypothesis that the ripple formations were a consequence of the spheres and their cavities acquiring an oil film coating after passing through the oil layer that was resting on the water surface.

8.3. Definitions of the characteristic quantities associated with 'rippling'

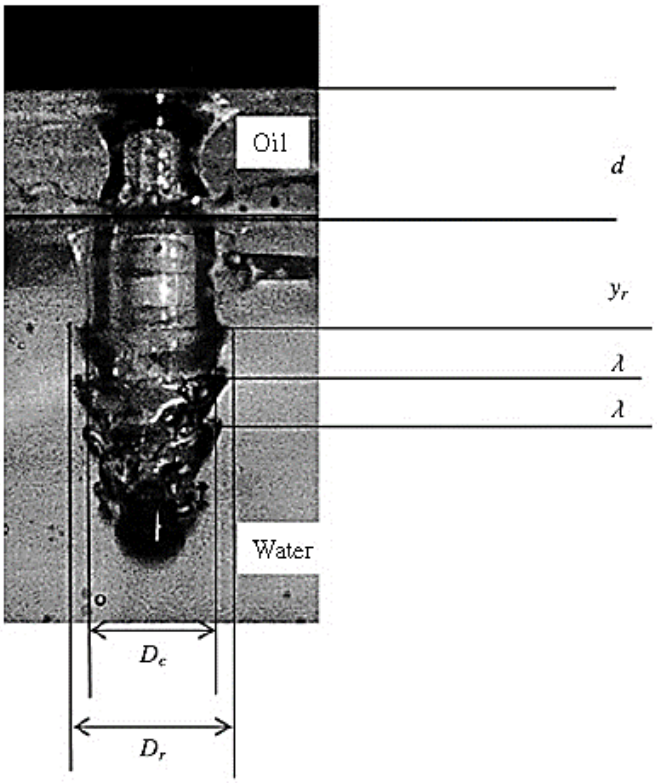

Figure 63: The characteristic quantities associated with 'rippling' studied in this chapter. The picture shows a steel sphere (D = 8mm and u_i = 3.43m/s) entering into water that had a d = 12.5mm layer of silicone oil (ν_o = 1000mm^2/s) resting on its surface. Figure from Tan *et al.* [7], reprinted with permission. © Cambridge University Press 2016.

Figure 63 presents the physical qualities associated with the 'rippling' phenomenon that will be studied in this chapter. From the figure, λ represent the ripple wavelength, y_r the ripple appearance depth, d the oil layer thickness while D_r and D_c are the diameters of the cavity with and without the ripple respectively. For reason of simplicity, D_r and D_c will henceforth be referred to as the 'diameter of the cavity-ripple' and the 'diameter of the cavity' respectively. In order to ensure consistency, D_r

and D_c were measured from the first formed ripple and along the same horizontal plane.

The ripple amplitude, γ while not presented in the figure can be calculated by $\gamma = (D_r - D_c)/2$ and from here, the ripple growth rate will be estimated. As shown in Figure 64, the ripples became less well-defined when the sphere moved further into the water. Hence it was usually only possible to obtain reliable data from the first three to five well-developed ripples.

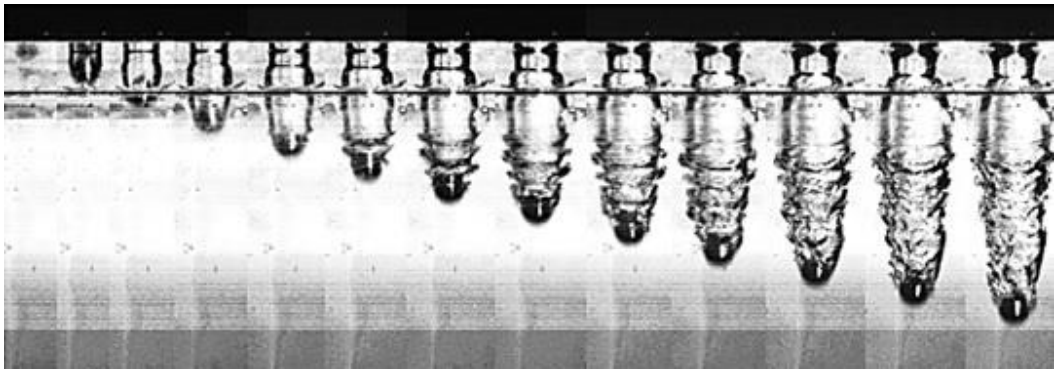

Figure 64: Cavity formation following sphere (D = 9mm and u_i = 4.2m/s) entering into water that had a 12.5mm layer of silicone oil (ν_o = 1000mm^2/s) resting on its surface. It can be observed that the ripples formed subsequent to the first three ripples were less well-defined. The time difference between each successive image is 2ms.

It should be noted that for all experiments documented in this chapter from this point onwards, the high viscosity silicone oil (ν_o = 1000mm^2/s) was used as the oil layer for the two-layer, oil-water system and the oil layer thickness was kept at d = 12.5mm.

8.4. Ripple wavelength, λ

The ripple wavelength, λ is defined as the displacement between successive ripples as shown in Figure 63. Measurements of λ revealed that λ between each of the first three to five ripples were consistent and did not display any significant difference. This observation is supported by Figure 62 and other relevant pictures throughout the thesis.

Meanwhile, it can be observed from the relevant pictures in Chapter 4 that the ripples are further apart from one another in the 'transition' phenomenon as compared to the 'rippling' phenomenon. Such observation suggests that the impact velocity of the sphere, u_i may have an influence on λ.

Figure 65 presents the ripple wavelength, λ as a function of the inverse of the impact velocity of the spheres, u_i^{-1}. If the uncertainties in the measurements were to be neglected, the data points appear to collapse into a single straight line. Therefore, it can be concluded that λ is linearly proportional to u_i^{-1} while being independent of both sphere diameter, D and oil layer thickness, d.

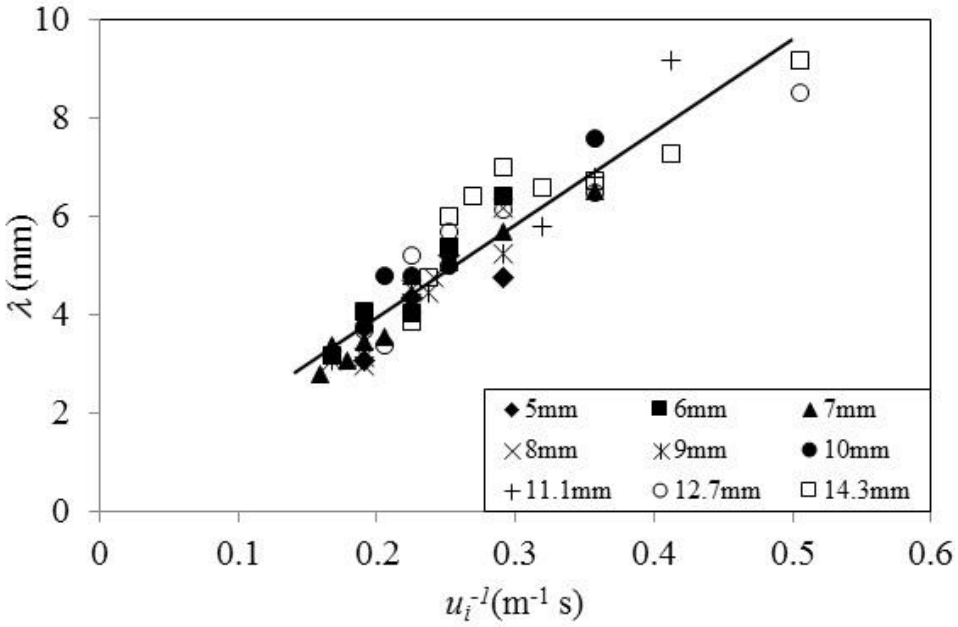

Figure 65: The ripple wavelength, λ as a function of the inverse of impact velocity of the spheres, u_i^{-1}. The data points appear to collapse into a single straight line. Meanwhile, the diameters of the spheres are shown in the legend. Figure from Tan *et al.* [7], reprinted with permission. © Cambridge University Press 2016.

8.5. Ripple appearance depth, y_r

The ripple appearance depth, y_r as shown in Figure 63, is defined as the depth under the oil-water interface where the ripples begin to form on the cavity walls.

Figure 66 presents the ripple appearance depth, y_r as a function of the inverse of the impact velocity of the spheres, u_i^{-1}. If the uncertainties in the measurements were also to be neglected, the data points shown in Figure 66, similar to those in Figure 65 for λ, appear to collapse into a single straight line. Hence this observation suggests that a relationship exists between y_r and u_i^{-1} while simultaneously showing y_r is also independent of both sphere diameter, D and oil layer thickness, d.

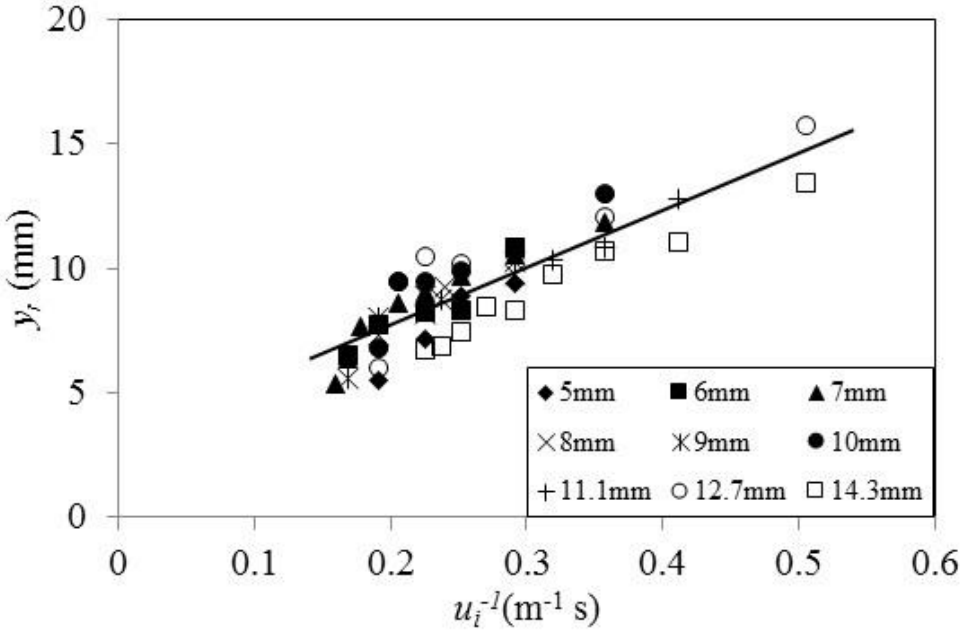

Figure 66: Ripple appearance depth, y_r as a function of the inverse of the impact velocity of the spheres, u_i^{-1}. Similar to Figure 65, the data points appear to collapse into a single straight line. The diameters of the spheres are shown in the legend. Figure from Tan *et al.* [7], reprinted with permission. © Cambridge University Press 2016.

Further extension to the line of best-fit shown in Figure 66 reveal that the line will not pass through the origin, indicating that there will always be parts of cavity walls remaining smooth and free of ripples for all values of u_i. However, further experiments are being recommended to verify such conclusion.

8.6. Ripple generation velocity, u_r

The time interval, t_r between the generation of successive ripples can be measured directly from the video recordings. By taking the inverse value of t_r, one will obtain the frequency of ripple generation, $f_r = 1/t_r$. Individual measurements of t_r for relatively low values of f_r where $f_r < 500$Hz have suggested that t_r is constant for

the generation of the first three to five well-developed ripples that can usually be clearly observed.

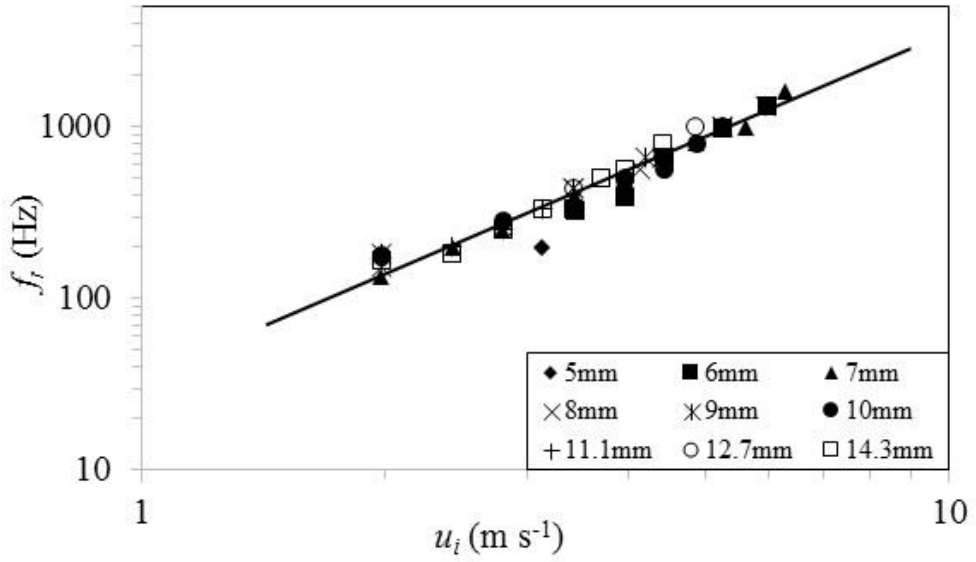

Figure 67: The frequency of ripple generation, f_r as a function of the impact velocity, u_i in a double-logarithmic graph. The diameters of the spheres are shown in the legend. Figure from Tan *et al.* [7], reprinted with permission. © Cambridge University Press 2016.

Figure 67 presents a summary of the data for t_r as a function of impact velocity, u_i in double-logarithmic representations. A calculation of the gradient of the line of best-fit shown in Figure 67 reveals its value to be 2.001, a value that is very close to 2. Hence the gradient appears to demonstrate that f_r is directly proportional to u_i^2. In addition, similar to λ and y_r, f_r is also found to be independent of the sphere diameter, D and oil layer thickness, d.

The ripple generation velocity, u_r is the velocity at which the ripples appear to be travelling upwards relative to the downward-moving sphere and can be calculated by $u_r = f_r \lambda$. Since $\lambda \propto u_i^{-1}$ and $f_r \propto u_i^2$, the relationship $u_r \propto u_i$ is expected to exist.

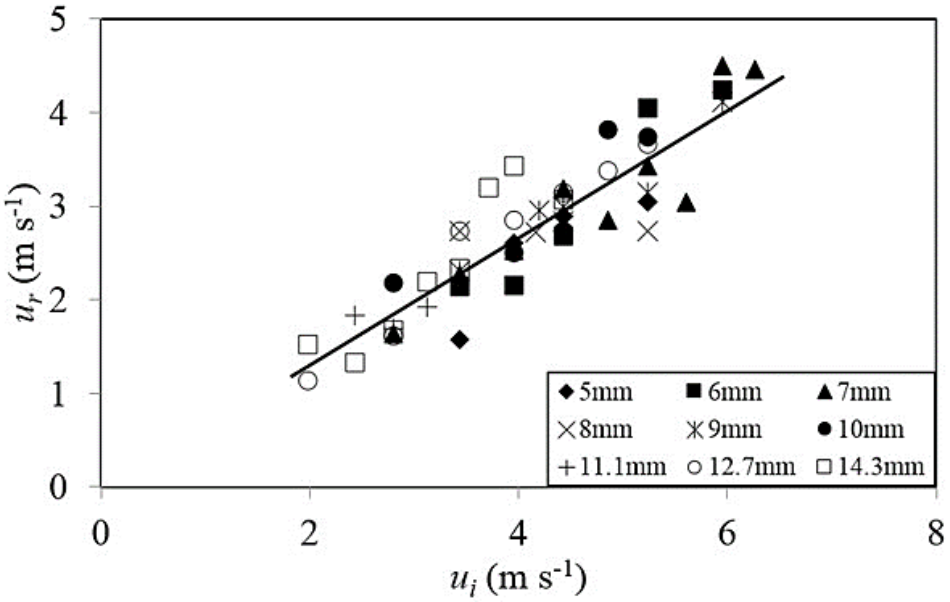

Figure 68: The ripple generation velocity, u_r as a function of the impact velocity of the spheres, u_i. The diameters of the spheres are shown in the legend. Figure from Tan *et al.* [7], reprinted with permission. © Cambridge University Press 2016.

Figure 68 presents the ripple generation velocity, u_r as a function of the impact velocity of the spheres, u_i. A linear least squares interpolation of the data in Figure 68 produces $u_r \approx 0.67\ u_i$.

The independently obtained result from Chapter 6.5 for the mean sphere velocity to the instant of deep seal after entering into a two-layer, silicone oil-water system is $\langle u_{ds} \rangle = 0.59\ u_i$. Since $0.59\ u_i \approx 0.67\ u_i$ and u_r is measured relative to the downward-moving sphere, both velocities will have balanced each other so that the ripples are almost stationary with respect to the vertical plane while showing only a very slight upward drift. This conclusion can be verified by close inspection and comparison of the ripples in successive images shown in Figures 16 and 64. It can be observed that the ripples do not have any obvious change in positions between successive images in these figures.

8.7. The diameter of the cavity-ripple, D_r

The impact velocities, u_i and diameters, D of the spheres were variables in the experiments. Hence in order to provide a clear comparison, two sets of data for D_r are presented, one for spheres that possessed a common u_i while the other for spheres that had the same D.

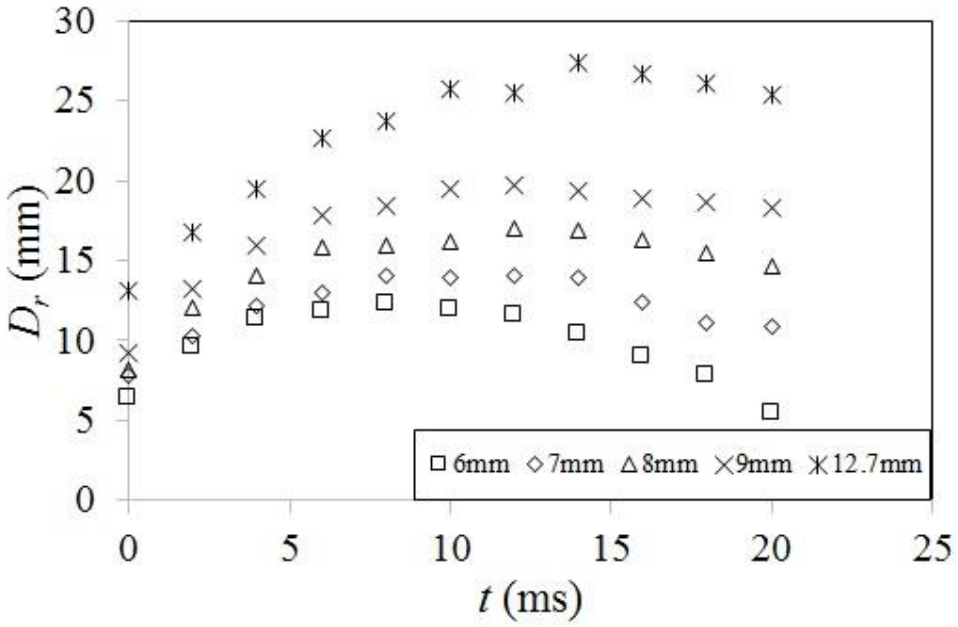

Figure 69: The diameter of the cavity-ripple, D_r with respect to time, t. The spheres had the same impact velocity, u_i = 3.43m/s but different diameters, D as indicated in the legend.

Figure 69 presents the measurements of D_r with respect to time, t from the instant when the first ripple began forming along the cavity walls for spheres that had a common impact velocity, u_i = 3.43m/s but different diameters, D. As both D_r and D_c were measured at the ripple appearance depth, y_r which itself is only dependent on u_i, the data presented in Figure 68 were all taken at the same depth below the oil-water interface. In general, D_r is observed to increase until a 'maximum point' and decrease

thenceforth. Another observation from the figure reveals that D_r for larger spheres will take a longer time to reach their maximum points.

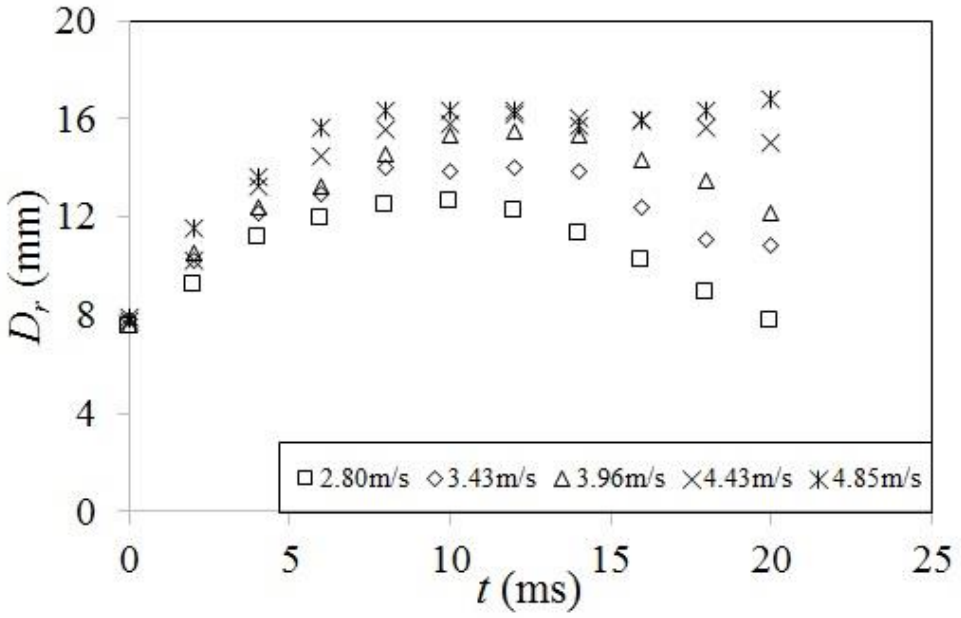

Figure 70: The diameter of the cavity-ripple, D_r with respect of time, t. The spheres had a common diameter, D = 7mm but different impact velocity, u_i as indicated in the legend.

Figure 70 presents the measurements of D_r with respect to time, t from the instant when the first ripple began forming along the cavity walls for spheres that had a common diameter, D = 7mm but different impact velocities, u_i. It can be observed from the figure that at any instant, D_r was greater for spheres that have higher impact velocities. Similar to Figure 69, the data points of D_r generally increase to a maximum value and decrease thenceforth.

Meanwhile, Figure 70 also suggests that the time interval between ripple formation and the instant when the maximum value is reached is independent of u_i. As interpreted from the same figure, that time interval for spheres of diameter, D = 7mm is approximately t = 10ms.

The reader may also have noticed that the data points of D_r for u_i = 4.85m/s begin increasing again from about t = 15ms. The reason for such observation is that the diameter of the cavity, D_c continues to increase despite D_r has already begun decreasing. Hence there will be an instant when D_r merges with D_c and henceforth D_r = D_c. Therefore for spheres of impact velocity, u_i = 4.85m/s, the data points after approximately t = 15ms are actually those of the increasing D_c shown in Figure 73.

8.8. The diameter of the cavity, D_c

Similar to the comparisons done in Chapter 8.7 above, two sets of data for D_c are presented, one for spheres that possessed a common impact velocity, u_i while the other for spheres that had a common sphere diameter, D.

Figure 71 presents the measurements of D_c with respect to time, t from the instant when the first ripple began forming along the cavity walls for spheres that had the same impact velocity, u_i = 3.43m/s but different diameters, D. As the measurements were taken at the ripple appearance depth, y_r, the data presented in Figure 71 were all taken at the same depth below the oil-water interface. In general, the data points also appear to increase until a peak value and decrease thenceforth with smaller spheres reaching this peak value earlier than the bigger spheres. It should be noted that this peak value is a completely different quantity to the ‘maximum value’ mentioned in Chapter 8.7.

Meanwhile, as documented in Chapter 6.3, the deep seal time, t_{ds} will be greater for larger spheres as compared to spheres that have smaller diameters. Therefore, it can be understood that the cavities generated by the larger spheres will have more time to expand before reaching the peak value and subsequently contract due to the approaching deep seal.

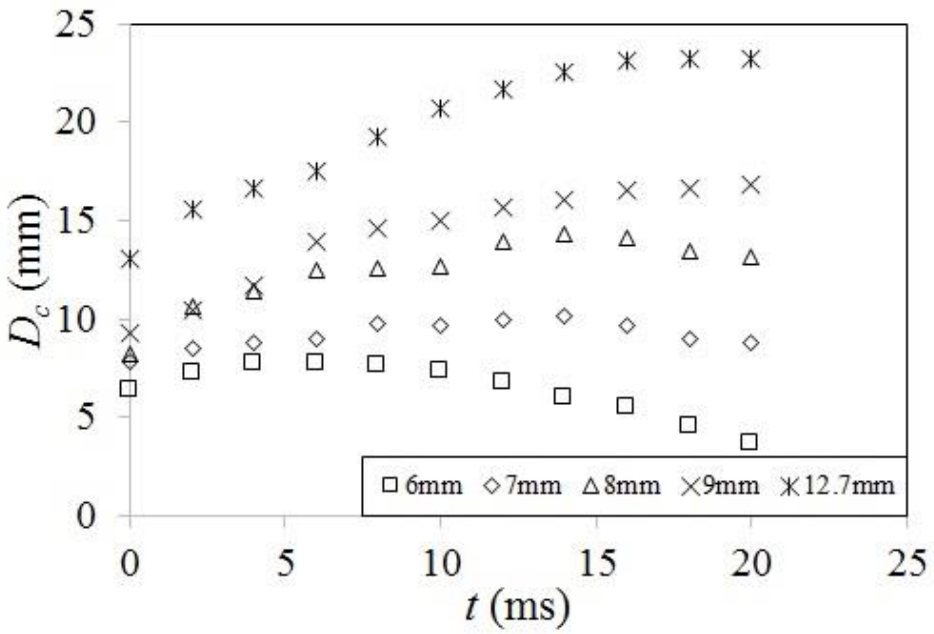

Figure 71: The diameter of the cavity, D_c with respect to time, t. The spheres had the same impact velocity, u_i = 3.43m/s but different diameters, D as indicated in the legend.

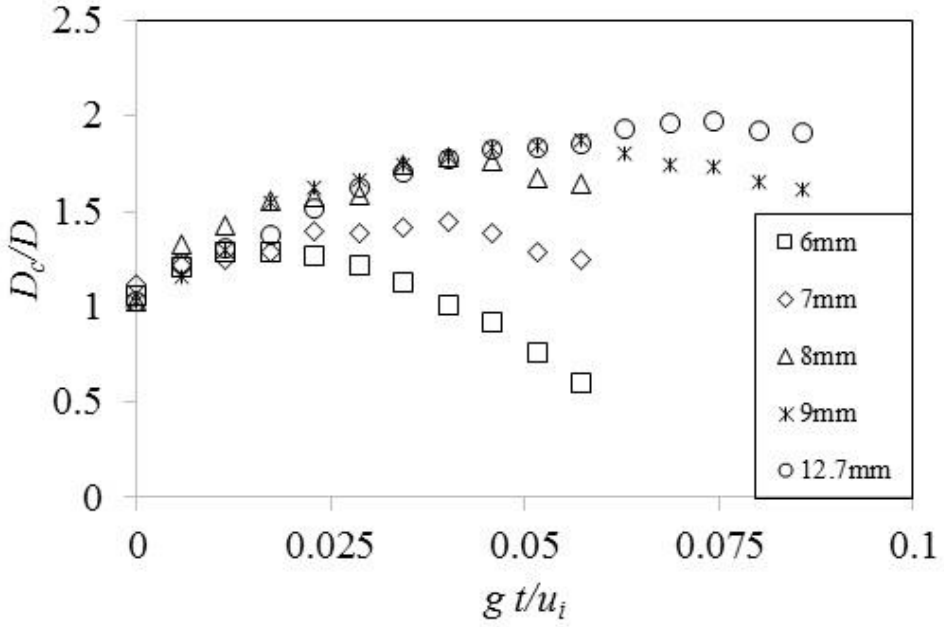

Figure 72: The data from Figure 71 presented in dimensionless form. The sphere diameters are indicated in the legend.

Figure 72 redisplays the data from Figure 71 in dimensionless form. During the non-dimensionalisation process, the initial data points collapse into a single line, demonstrating that the cavity expansion at the same depth for spheres of the same velocity is only dependent on the sphere diameter.

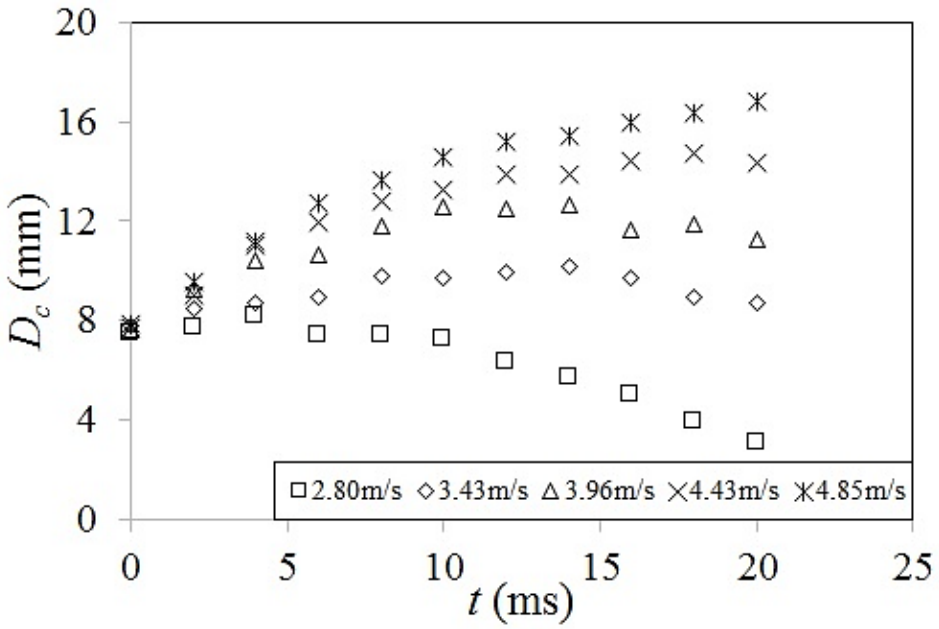

Figure 73: The diameter of the cavity, D_c with respect to time, t. The spheres had the same diameter, D = 7mm but different impact velocities, u_i as indicated in the legend.

Figure 73 presents the measurements of D_c with respect to time, t from the instant when the first ripple began forming along the cavity walls for spheres that had the same diameter, D = 7mm but different impact velocities, u_i. The figure also shows the data points increasing until a peak value and decreasing thenceforth. This peak value is greater and the time taken to reach it is longer for spheres with higher u_i.

The deep seal time, t_{ds} as presented in Chapter 6.3, is independent of u_i and is a constant value for spheres that have the same diameter, D. However, as presented in Chapter 8.5, the ripple appearance depth, y_r has an inverse relationship with u_i, indicating that the D_c measured for spheres with a lower u_i is at a deeper depth relative

to that measured for spheres with a higher u_i. Consequently, D_c for cavities generated by spheres with higher u_i have more time to expand and will reach a greater peak value before contracting due to the approaching deep seal.

Figure 73 also shows that the data points of D_c for the cavity generated by the sphere that had impact velocity, u_i = 4.85m/s continue to increase after t = 15ms. This is the instant when the data points of the already decreasing diameter of the cavity-ripple, D_r for the same cavity merges with the data points of D_c and subsequently $D_r = D_c$. Hence the reader will observe an increase of D_r again after about t = 15ms as shown in Figure 70.

8.9. Ripple amplitude, γ

The ripple amplitude, γ is defined as the difference between the radius of the cavity with the ripple and that of the same cavity without the ripple. Hence with reference to Figure 63 in Chapter 8.3, $\gamma = (D_r - D_c)/2$.

The conclusion that the ripples are almost stationary with respect to the vertical plane will indicate that they only grow or expand horizontally. However, it should be noted that the cavity on which the ripples are formed also expands simultaneously along the same horizontal plane.

Having obtained the data for the diameters of the cavity-ripples, D_r and that of the cavities, D_c, the data for the ripple amplitude, γ will be computed. Similar to Chapters 8.7 and 8.8 above, two sets of data for γ will be presented with respect to time, t from the instant when first ripple began forming along the cavity walls. The first set of data will be for spheres that had the same impact velocity, u_i but different

diameters, D while the second set of data will be for spheres that had a common D but different u_i.

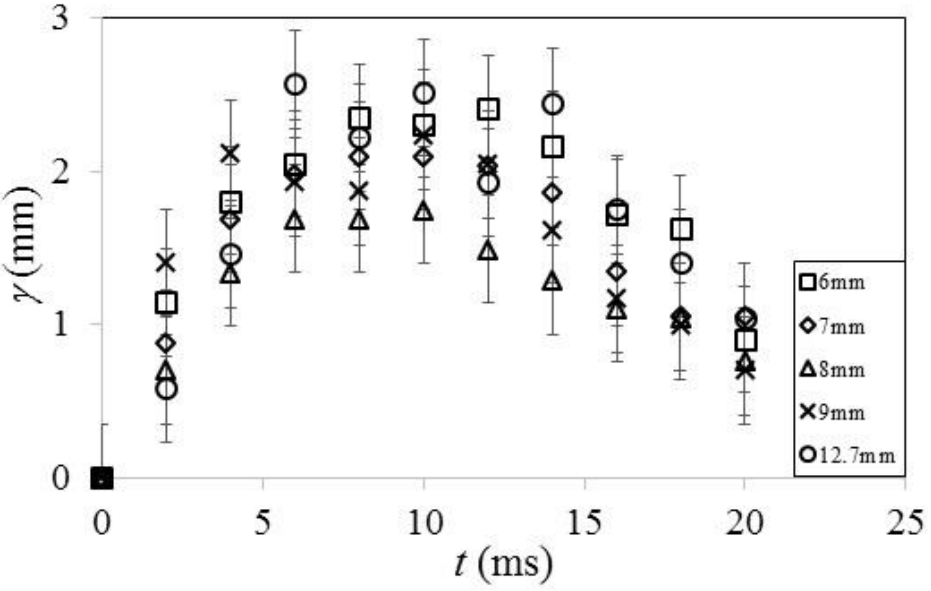

Figure 74: The ripple amplitude, γ with respect of time, t for spheres that had the same impact velocity, u_i = 3.43m/s but different diameters, D as indicated in the legend. The vertical bars represent the uncertainties, E_γ estimated in the measurements. Figure from Tan *et al.* [7], reprinted with permission. © Cambridge University Press 2016.

Figure 74 presents the ripple amplitude, γ with respect to time, t from the instant when the first ripple began forming along the cavity walls for spheres that had a common impact velocity, u_i = 3.43m/s but different diameters, D. The vertical bars represent the uncertainties associated with the determinations of the amplitudes from the video recordings which was estimated to be E_γ = +/- 0.35mm or +/- 17.5%. The reader will observe that the ripples reached their maximum amplitude, $\gamma \approx$ 2mm at approximately 8ms < t < 10ms and disappeared by about t = 25ms. An examination of Figure 74 shows that, within the margin of error represented by the vertical bars, the data do not show a dependence on the sphere diameter, D.

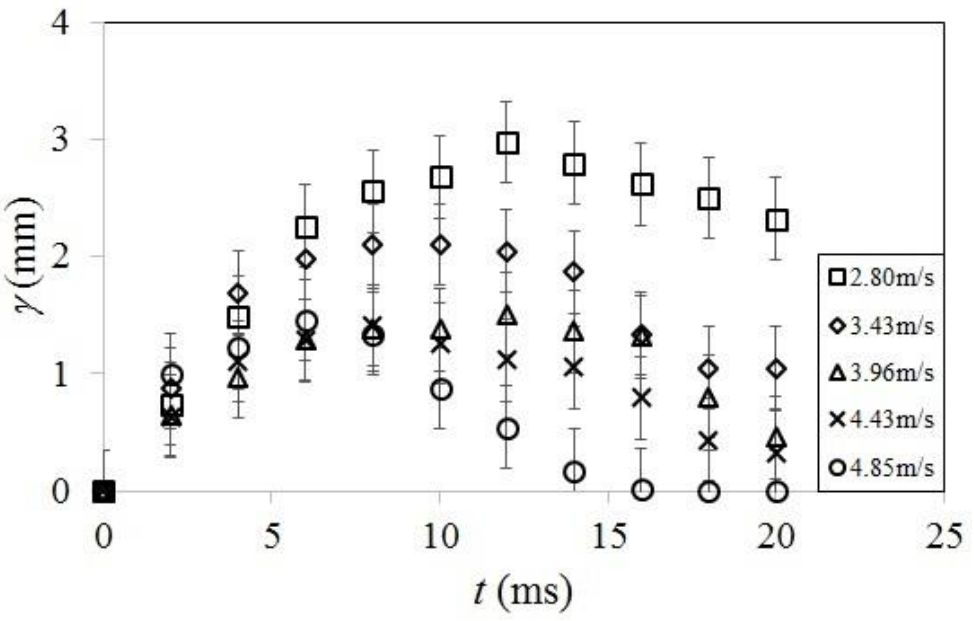

Figure 75: The ripple amplitude, γ with respect to time, t for spheres that had the same diameter, D = 7mm but different impact velocities, u_i as shown in the legend. The vertical bars represent the uncertainties, E_γ in measurements. Figure from Tan *et al.* [7], reprinted with permission. © Cambridge University Press 2016.

Figure 75 presents the ripple amplitude, γ with respect to time, t from the instant when the first ripple began forming along the cavity walls for spheres that had the same diameter, D = 7mm but different impact velocities, u_i. The vertical bars, similar to those shown in Figure 74, again represent the uncertainties estimated in the measurements, E_γ = +/- 0.35mm. It can be concluded from Figure 75 that a clear dependence of the ripple amplitude, γ on the impact velocities, u_i beyond the margin of error did exist.

The reader may also observe a pattern where γ will increase until a maximum amplitude before decreasing to zero at the instant when the diameter of the cavity-ripple, D_r merges with that of the cavity, D_c. In addition, Figure 73 also shows that γ for spheres that had lower u_i would reach a higher amplitude as compared to that for

spheres with higher u_i. This is consistent with experimental observations as the ripples generated at lower u_i especially those generated during the 'transition' phenomenon, were relatively bigger and 'more obvious' due to the cavities on which they formed were expanding at a slower rate.

8.10. Dimensionless ripple amplitude, γ^* and its growth rate, $\dot{\gamma}^*$

Chapter 8.9 presents the observation of the clear dependence of the ripple amplitude, γ on the impact velocity of the sphere, u_i. Hence the variables will be non-dimensionalised in an endeavour to collapse all the data points in Figure 93 into a single line.

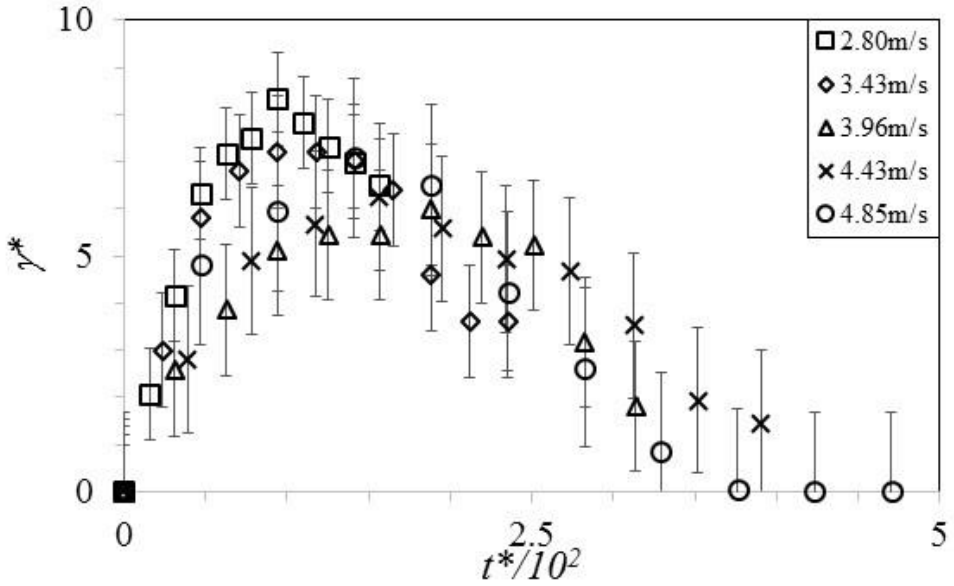

Figure 76: The dimensionless ripple amplitude. $\gamma^* = \gamma u_i / \nu_o$ as a function of the dimensionless time, $t^* = t\, u_i^2 / \nu_o$ where $\nu_o = 1000\text{mm}^2/\text{s}$ is the kinematic viscosity of the silicone oil. The data are for spheres that had the same diameter, D = 7mm but different impact velocities, u_i as indicated in the legend. Figure from Tan *et al.* [7], reprinted with permission. © Cambridge University Press 2016.

Figure 76 redisplays the data of Figure 75 in dimensionless form. The ripple amplitude, γ and time, t were non-dimensionalised to form $\gamma^* = \gamma u_i / \nu_o$ and $t^* = t\, u_i^2 / \nu_o$ respectively. Meanwhile, the extent of the error bars on the same figure is $E_\gamma^* = +/- E_\gamma u_i / \nu_o$. The kinematic viscosity used in the calculations is that of silicone oil, ν_o = 1000mm^2/s. Since the kinematic viscosity in the experiments did not vary, the kinematic viscosity of water may also have been used in the non-dimensionalisation process. However, the value for silicone oil was chosen to minimise the magnitudes of the new dimensionless quantities.

Therefore, it can be observed and concluded from Figure 76 that the non-dimensionalisation of the variables has resulted in the data points from Figure 75 collapsing reasonably into a single line within the error margins.

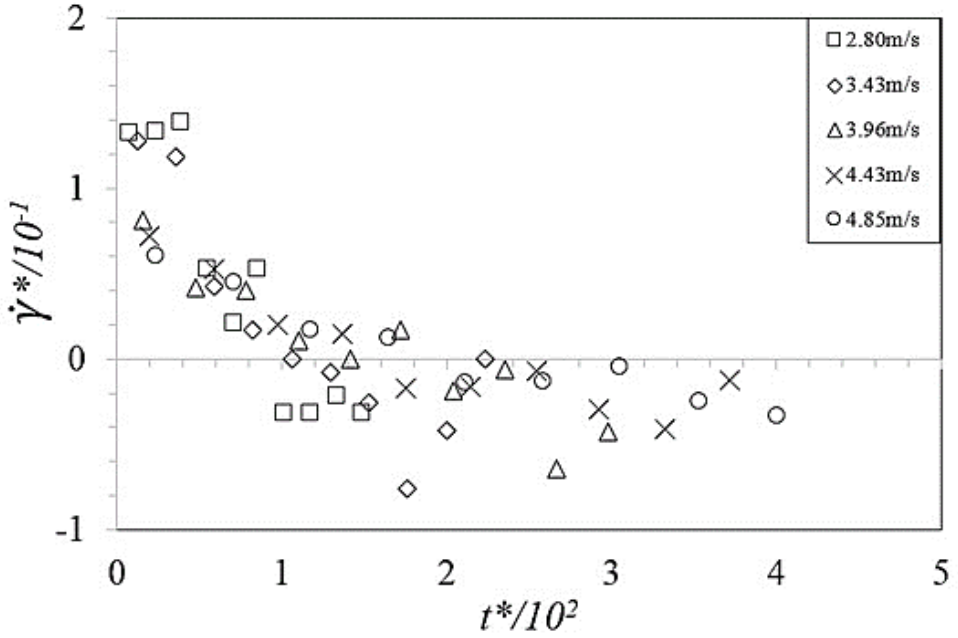

Figure 77: The dimensionless ripple growth rate, $\dot{\gamma}^*$ as a function of the dimensionless time, t^*. The data are for spheres that had the same diameter, D = 7mm but different impact velocities as indicated in the legend. Figure from Tan *et al.* [7], reprinted with permission. © Cambridge University Press 2016.

Figure 77 displays the dimensionless ripple growth rate, $\dot{\gamma}^*$ as a function of the dimensionless time, t^*. The values for $\dot{\gamma}^*$ represent finite-difference approximations obtained for pairs of consecutive data points i and j, with $i < j$, as $\dot{\gamma}^*_{j,i} = (\dot{\gamma}^*_j - \dot{\gamma}^*_i)/(t^*_j - t^*_i)$ which was then associated with time $t^* = \frac{1}{2}(t^*_j + t^*_i)$. The same figure reveals that the dimensionless growth rate at the beginning of ripple formation is of the order of $\dot{\gamma}^* = 0.1$, suggesting that $\dot{\gamma} = 0.1\, u_i$. Hence the ripple growth rate at the instant of ripple formation is about 10% of the impact velocity of the sphere.

8.11. Discussions of the results for the ripple instability

If capillary effects were responsible for the formation of ripples, surface tension and the oil-water interfacial tension forces should be dominant or significant compared to both gravitational and inertial forces, resulting in low Bond, $Bo = \Delta\rho g R^2/\sigma$ and Weber numbers, $We = \rho u^2 R/\sigma$.

In order to make a direct comparison with data from present literature, for instance, Aristoff & Bush [21] and Mansoor *et al.* [50], the minimum and maximum Bond and Weber numbers were estimated using the radius, R of the sphere instead of its diameter, $D = 2R$ that is commonly used throughout this thesis. The ρ and $\Delta\rho$ represent the density of water and the magnitude of the density difference between water and the air filling the cavity respectively and $\Delta\rho \approx \rho = 1000\text{kg/m}^3$. In an endeavour to maximise the influence of surface tension and the oil-water interfacial tension forces in the calculations, the surface tension of water at room temperature, σ_w = 0.0728N/m was used. This is in contrast to the surface tension of the silicone oil, σ_o = 0.0212N/m and the oil-water interfacial tension, σ_{ow} = 0.0429N/m. Hence the Bond

and Weber numbers for the experiments in the present study where the formation of ripples on the cavity walls were observed are in the following range: $0.28 \leq Bo \leq 6.9$ and $39 \leq We \leq 3536$.

Therefore, the above estimations demonstrate that the inertial forces were far more dominant as compared to the surface tension forces. As $\sigma_w > (\sigma_o + \sigma_{ow})$, the Bond and Weber numbers above would be underestimated and consequently in reality, the inertial forces would be far more dominant, making the surface tension and interfacial tension forces even more insignificant. Hence from the above analysis and assumptions, it can be concluded that the ripples were not generated as a result of capillary effects.

The reader may notice the similarities in appearance between the ripples in the present study and those photographed by Grumstrup *et al.* [43]. However, there are fundamental differences between the ripple patterns observed during the present study and those observed by Grumstrup *et al.* [43].

Firstly, in contrast to the present study, Grumstrup *et al.* [43] investigated objects entering water without the presence of any oil layer resting on the water surface. In addition, they wrote that their '*large-amplitude oscillations begin at the moment of deep seal*'. However, in the present study, the ripples were observed forming at a relatively shallow depth, y_r below the oil-water interface.

Secondly, Grumstrup *et al.* [43] wrote about the existence of a linear dependence of the ripple wavelength, λ on the sphere diameter, D in the case of their ripples. However, in Figure 65 of this thesis, the ripple wavelength is shown to be independent of the sphere diameter. Therefore, despite the close similarities in

appearance, it will not be possible that the ripples observed in the present study and those of Grumstrup *et al.* [43] are of the same nature.

Since the appearance of the ripples observed in the present study hypothesizes that the developing patterns may be related to vortex shedding from the impacting sphere, an investigation to verify this hypothesis has also been endeavoured. The data analysis in Chapter 8.6 shows that the ripple generation velocity, $u_r \approx 0.67\ u_i$ and the value $u_r/u_i = f_r\ \lambda\ /\ u_i = 0.67$ represent the Strouhal number, *St* that is commonly associated with vortex shedding from solid bodies. A summary of some classic experimental data for the dependence of the Strouhal number on the Reynolds number for spheres can be seen in Figure 3 of Sakamoto & Hainu [51].

The Reynolds numbers, *Re* associated with the data in the phase diagram shown in Figure 19 of this thesis where the 'rippling' phenomenon occurred had been calculated. For the experiments that used the high viscosity silicone oil (ν_o = 1000mm^2/s) as the upper-layer liquid, the Reynolds number was in the range $16{,}000 \leq Re \leq 67{,}000$ if *Re* is calculated using the kinematic viscosity of water. Meanwhile, were the kinematic viscosity of the silicone oil be used instead, the Reynolds number would be in the range $16 \leq Re \leq 67$. A reference to Figure 3 of Sakamoto & Hainu [51] shows that $Re < 67$ will be too low for the occurrence of vortex shedding. In the other case where $Re > 16{,}000$, the values of *Re* would be greater than the critical value $Re \approx 10{,}000$ for which data points of the high-mode branch exist and show $St \approx 0.2$ on the low-mode branch. The displayed data extrapolation shown for the high-mode branch $16{,}000 \leq Re \leq 67{,}000$ would suggest that the Strouhal number, *St* to be approximately in the region $3 < St < 8$. Since $St = 0.67$ had been obtained for the ripples observed in the present study, it is highly unlikely that the development of these ripple patterns is associated with vortex shedding. According to the data shown in Figure 3

of Sakamoto & Hainu [51], vortex shedding will be a realistic hypothesis for $0.3 < St < 1$ if the corresponding Reynolds number is approximately in the region $1000 < Re < 4000$ which is clearly not the case in the present study.

Grumstrup *et al.* [43] also found that the Strouhal number, $\lambda f / u_i$ for their ripple patterns was also independent of the Reynolds number and they obtained $St = 1.0$ in contrast to the $St = 0.67$ obtained in the present study at similar Reynolds numbers. Moreover, the conclusion that the ripple patterns in the present study are not associated with vortex shedding is consistent with Truscott *et al.* [18] who commented on their own particle image velocimetry measurements and referred to supporting results from Bergmann *et al.* [39], stating that their cavity-forming cases demonstrated very little vorticity in general and no organised vortical structures in the wakes.

Since the ripple patterns observed in the present study were not of the same acoustic origin as those observed by Grumstrup *et al.* [43] and also not associated with vortex shedding, it is hypothesized that the ripple instability was a result of the shear force established between the oil film coating the spheres and the surrounding water. This hypothesis is supported by the collapse of the data for different impact velocities, u_i for the non-dimensional ripple amplitude and growth rate shown in Figures 76 and 77 respectively.

Moreover, as the data for the ripple amplitude, γ has been found to be independent of the sphere diameter, D as shown in Figure 74, the nature of the developing instability appears to be two-dimensional. Hence the instability only depends on the local flow characteristics at the location where the ripples develop and not on the global flow structure and geometry surrounding the sphere. This is supported by the results obtained earlier in this chapter that show the ripple

wavelength, λ, ripple appearance depth, y_r, ripple generation frequency, f_r and the ripple generation velocity, u_r all scaling linearly with the impact velocity, u_i while being independent of the sphere diameter, D.

The hypothesis that the ripple instability arises as a result of the shear force between the oil films coating the spheres and the surrounding water will furthermore be the reason the ripples being most well-developed shortly after the sphere crosses the oil-water interface while plenty of oil is present on the sphere and its surrounding. Likewise, the same hypothesis will be the explanation to the ripples being less well-defined at later stages of the sphere motion when the majority of the oil film coating has already been shed off and left behind in the wake of the sphere.

Chapter 9: Conclusion

''Let us hear the conclusion of the whole matter: Fear God, and keep his commandments: for this is the whole duty of man.''

------ Ecclesiastes 12:13, KJV

The present study involves experimental investigations on the phenomena, cavity formations and dynamics associated with rigid spheres entering into a stratified two-layer system of immiscible liquids. The observations and results presented and discussed in this thesis have shown that the dynamics associated with cavity formation at the wakes of spheres entering and submerging in two-layer, oil-water systems are significantly different from that of corresponding entries into single-phase, homogeneous liquids such as water.

In Chapter 4, four possible phenomena that will potentially occur subsequent to rigid spheres entering into a two-layer, oil-water system have been identified. The occurrence of these phenomena was found to be determined by factors such as the density, diameter and impact velocity of the spheres. The most notable observation is the formation of wave-like structures or commonly referred to as ripples in this thesis, along the otherwise smooth cavity walls during the 'transition' and 'rippling' phenomena. At the point of writing and to the best of the author's knowledge, other than the author's publications, these ripples are not described or mentioned previously.

In Chapter 5, phenomena that are not consistent with present literature and current understanding have been observed subsequent to steel spheres entering and submerging in sunflower oil and the two-layer, sunflower oil-water system. Shallow seal was observed along with deep seal at relatively high impact velocities while

further increases in impact velocities led to the deep seal not occurring completely and the cavity experienced only shallow seal. Therefore, the spheres generated significant cavities at relatively low impact velocities while forming relatively small cavities at higher impact velocities. Further investigations reveal that these phenomena are influenced by the surface conditions of the spheres. Hence the phenomena demonstrate the substantial influence both the surface conditions of a body and the upper layer liquid in a two-layer liquid system can potentially have on cavity dynamics.

In the following chapters, the dynamics of deep seal, the spheres themselves and the wave-like structures or ripples are studied and discussed. As written above, during the 'rippling' phenomenon, the structure of the enclosing liquid boundary of the cavity is significantly modified by the formation of ripples in contrast to the smooth cavity boundary for the well-studied corresponding case of single-phase, homogeneous liquids. The discussion of data for ripple dynamics presented in Chapter 8 suggests that the instabilities resulting in ripple formation are associated with the spheres acquiring oil film coatings while passing through the thin oil layer immediately prior to entering into the water directly underneath. It is highly likely that these instabilities arise as a consequence associated with the shear forces establishing and acting between the oil coating of the spheres and the surrounding water. Additional support for this conclusion is provided by flow visualisations from test runs where spheres were first coated with oil before being released into a deep pool of water that had no oil layer resting on its surface.

Meanwhile, the same data analysis in Chapter 8 reveals that the ripple wavelength, the ripple appearance depth which is the displacement under the oil-water interface where the ripples were first formed, the ripple generation velocity and the growth rate of the ripple amplitudes are all independent of the diameter of the spheres

but scale with their impact velocities. In particular, the growth rate of the ripple amplitude at the instant when the first ripple begins forming has been found to be approximately 10% of the impact velocity. It is argued that the insensitivity of these four quantities to the sphere diameter suggests that the generation of the ripples depends only on local flow conditions at the location of ripple formation and the instability is not affected by the overall, global three-dimensional flow field surrounding the sphere. Therefore, it has been concluded that the nature of the instability is only two-dimensional and axisymmetric. Meanwhile, the ripple patterns from the present study are also being compared with similar patterns observed by Grumstrup *et al.* [43] but further discussions reveal that both structures do not have the same origin should the interpretations and conclusions of Grumstrup *et al.* [43] be correct.

The present study moreover reveals that the phenomenon of deep seal which was previously studied by Truscott & Techet [15] for spheres entering and submerging in a pool of homogeneous water without an oil layer, occurs in a qualitatively similar way for the stratified two-layer system of immiscible liquids. The deep seal time and deep seal depth as defined in Truscott & Techet [15] have also been studied for two-layer, oil-water systems and for other single-phase, homogeneous liquids such as sunflower oil and the more viscous silicone oil in Chapter 6. From these studies, the data for the deep seal time for single-phase sunflower oil and silicone oil are revealed to be in good qualitative agreement with the data for water from Truscott & Techet [15]. However, the results in the present study also show that both deep seal time and deep seal depth for the two-layer, oil-water systems studied in this thesis are significantly modified in comparison with the results from Truscott & Techet [15] for water. These differences are found to arise from increased drag forces acting on the

spheres moving in the two-layer, oil-water systems as a consequence of the spheres acquiring oil film coatings while passing through the oil layer before submerging in the deep pool of water that is directly underneath.

The present study has also laid the foundation for impact studies on two-layer systems of immiscible liquids. Further experiments may include the quantification of the effects on splashing patterns and surface sealing of cavity by the upper-layer liquid following solid entries. It is believed that such studies will have practical engineering applications in areas where the minimisation of splashing is desired.

Bibliography

[1] A. M. Worthington, ‘On Impact with a Liquid Surface’, *Proc. R. Soc. Ser. A* **34**, 217-230 (1882)

[2] A. M. Worthington and R. S. Cole, ‘Impact with a liquid surface studied by the aid of instantaneous photography’, *Phil. Trans. R. Soc. Ser. A* **189**, 137-148 (1897)

[3] A. M. Worthington and R. S. Cole, ‘Impact with a liquid surface studied by the aid of instantaneous photography, Paper II’, *Phil. Trans. R. Soc. Ser. A* **194**, 175-199 (1900)

[4] A. M. Worthington, ‘A Study of Splashes’, *Longmans, Green, and co.*, London, UK (1908)

[5] B. Franklin, W. Brownrigg and Rev. Mr. Farish, ‘Of the Stilling of Waves by means of Oil. Extracted from Sundry Letters between Benjamin Franklin, LL. D. F. R. S. William Brownrigg, M. D. F. R. S. and the Reverend Mr. Farish’, *Phil. Trans.*, **64**, 445-460 (1774)

[6] A. Mallock, ‘Sounds Produced by Drops Falling on Water’, *Proc. R. Soc. Lond. A* **95**, 138-143 (1918)

[7] B. C.-W. Tan, J. H. A. Vlaskamp, P. Denissenko and P. J. Thomas, ‘Cavity formation in the wake of falling spheres submerging into a stratified two-layer system of immiscible liquids’, *J. Fluid Mech.* **790**, 33-56 (2016)

[8] A. May, ‘Effect of Surface Condition of a Sphere on Its Water Entry Cavity’, *J. Appl. Phys.* **22**, 1219-1222 (1951)

[9] A. May and J. C. Woodhull, ‘Virtual Mass of a Sphere Entering Water Vertically’, *J. Appl. Phys.* **21**, 1285-1289 (1950)

[10] A. May, ‘Vertical Entry of Missiles into Water’, *J. Appl. Phys.* **23**, 1362-1372 (1952)

[11] D. Gilbarg and R. A. Anderson, ‘Influence of Atmospheric Pressure on the Phenomena Accompanying the Entry of Spheres into Water’, *J. Appl. Phys.* **19**, 127-139 (1948)

[12] G. Birkhoff and T. E. Caywood, ‘Fluid Flow Patterns’, *J. Appl. Phys.* **20**, 646-659 (1949)

[13] E. G. Richardson, ‘The Impact of a Solid on a Liquid Surface’, *Proc. Phys. Soc.* **61**, 352-367 (1948)

[14] H. I. Abelson, ‘Pressure measurements in the water-entry cavity’, *J. Fluid Mech.* **44**, 129-144 (1970)

[15] T. T. Truscott and A. H. Techet, ‘Water entry of spinning spheres’, *J. Fluid Mech.* **625**, 135-165 (2009)

[16] T. T. Truscott and A. H. Techet, ‘A spin on cavity formation during water entry of hydrophobic and hydrophilic spheres’, *Phys. Fluids* **21**, 121703 (2009)

[17] T. T. Truscott, B. P. Epps and J. Belden, ‘Water Entry of Projectiles’, *Ann. Rev. Fluid Mech.* **46**, 355-378 (2014)

[18] T. T. Truscott, B. P. Epps and A. H. Techet, ‘Unsteady forces on spheres during free-surface water entry’, *J. Fluid Mech.* **704**, 173-210 (2012)

[19] S. T. Thoroddsen, Y. G. Etoh, K. Takehara and Y. Takano, ‘Impact jetting by a solid sphere’, *J. Fluid Mech.* **499**, 139-148 (2004)

[20] S. T. Thoroddsen, ‘The making of a splash’, *J. Fluid Mech.* **690**, 1-4 (2012)

[21] J. M. Aristoff and J. W. M. Bush, ‘Water entry of small hydrophobic spheres’, *J. Fluid Mech.* **619**, 45-79 (2009)

[22] S. D. Howison, J. R. Ockendon and S. K. Wilson, ‘Incompressible water-entry problems at small deadrise angles’, *J. Fluid Mech.* **222**, 215-230 (1991)

[23] M. Lee, R. G. Longoria and D. E. Wilson, ‘Cavity dynamics in high-speed water entry’, *Phys. Fluids* **9**, 540-550 (1997)

[24] S. Gekle and J. M. Gordillo, ‘Compressible air flow through a collapsing liquid cavity’, *Int. J. Numer. Meth. Fluids* **67**, 1456-1469 (2011)

[25] S. Gekle, J. M. Gordillo, D. van der Meer and D. Lohse, 'High-Speed Jet Formation after Solid Object Impact', *Phys. Rev. Lett.* **102**, 034502 (2009)

[26] S. Gekle, I. R. Peters, J. M. Gordillo, D. van der Meer and D. Lohse, 'Supersonic Air Flow due to Solid-Liquid Impact', *Phys. Rev. Lett.* **104**, 024501 (2010)

[27] S. Gekle and J. M. Gordillo, 'Generation and breakup of Worthington jets after cavity collapse. Part 1. Jet formation', *J. Fluid Mech.* **663**, 293-330 (2010)

[28] J. M. Gordillo and S. Gekle, 'Generation and breakup of Worthington jets after cavity collapse. Part 2. Tip breakup of stretched jets', *J. Fluid Mech.* **663**, 331-346 (2010)

[29] I. R. Peters, D. van der Meer and J. M. Gordillo, 'Splash wave and crown breakup after disc impact on a liquid surface', *J. Fluid Mech.* **724**, 553-580 (2013)

[30] V. Duclaux, F. Caille, C. Duez, C. Ybert, L. Bocquet and C. Clanet, 'Dynamics of transient cavities', *J. Fluid Mech.* **591**, 1-19 (2007)

[31] Y. Ueda, M. Tanaka, T. Uemura and M. Iguchi, 'Water entry of a superhydrophobic low-density sphere', *J. Vis.* **13**, 289-292 (2010)

[32] Y. Ueda, T. Uemura and M. Iguchi, 'Entry of inclined hydrophobic and hydrophilic circular cylinders into water', *J. Vis.* **14**, 7-9 (2011)

[33] C. Duez, C. Ybert, C. Clanet and L. Bocquet, 'Making a splash with water repellency', *Nat. Phys.* **3**, 180-183 (2007)

[34] S. T. Thoroddsen and A. Q. Shen, 'Granular jets', *Phys. Fluids* **13**, 4-6 (2001)

[35] D. Lohse, R. Bergmann, R. Millelsen, C. Zeilstra, D. M. van der Meer, M. Versluis, K. van der Weele, M. van der Hoff and H. Kuipers, 'Impact on soft sand: void collapse and jet formation', *Phys. Rev. Lett.* **93**, 198003, 1-4 (2004)

[36] J. W. Glasheen and T. A. McMahon, 'Vertical water entry of disks at low Froude numbers', *Phys. Fluids* **8**, 2078-2083 (1996)

[37] O. R. Enriquez, I. R. Peters, S. Gekle, L. E. Schmidt, D. van der Meer and D. Lohse, 'Non-axisymmetric impact creates pineapple-shaped cavity', *Phys. Fluids* **23**, 091106 (2011)

[38] O. R. Enriquez, I. R. Peters, S. Gekle, L. E. Schmidt, D. Lohse and D. van der Meer, 'Collapse and pinch-off of a non-axisymmetric impact-created air cavity in water', *J. Fluid Mech.* **701**, 40-58 (2012)

[39] R. Bergmann, D. van der Meer, S. Gekle, A. van der Bos and D. Lohse, 'Controlled impact of a disk on a water surface: cavity dynamics', *J. Fluid Mech.* **693**, 381-409 (2009)

[40] J. O. Marston, I. U. Vakarelski and S. T. Thoroddsen, 'Cavity formation by the impact of Leidenfrost spheres', *J. Fluid Mech.* **699**, 465-488 (2012)

[41] A. Le Goff, D. Quere and C. Clanet, 'Viscous cavities', *Phys. Fluids* **25**, 043101 (2013)

[42] B. Akers and A. Belmonte, 'Impact dynamics of a solid sphere falling into a viscoelastic miscellar fluid', *J. Non-Newtonian Fluid Mech.* **135**, 97-108 (2006)

[43] T. Grumstrup, J. B. Keller and A. Belmonte, 'Cavity Ripples Observed during the Impact of Solid Objects into Liquids', *Phys. Rev. Lett.* **99**, 114502 (2007)

[44] S. Hartland, 'The approach of a rigid sphere to a deformable liquid/liquid interface', *J. Colloid Interface Sci.* **26**, 383-394 (1968)

[45] S. Hartland, 'The profile of the draining film between a rigid sphere and a deformable fluid-liquid interface', *Chem. Eng. Sci.* **24**, 987-995 (1969)

[46] S. Hartland and J. D. Robinson, 'The Dynamic Equilibrium of a Rigid Sphere at a Deformable Liquid-Liquid Interface', *J. Colloid Interface Sci.* **35**, 372-378 (1971)

[47] H. C. Maru, D. T. Wasan and R. C. Kintner, 'Behavior of a rigid sphere at a liquid-liquid interface', *Chem. Eng. Sci.* **26**, 1615-1628 (1971)

[48] A. S. Geller, S. H. Lee and L. G. Leal, 'The creeping motion of a spherical particle normal to a deformable interface', *J. Fluid Mech.* **169**, 27-69 (1986)

[49] P. P. Brown and D. F. Lawler, ‘Sphere drag and settling velocity revisited’, *J. Env. Eng.* **129**, 222-231 (2003)

[50] M. M. Mansoor, J. O. Marston, I. U. Vakarelski and S. T. Thoroddsen, ‘Water entry without surface seal: extended cavity formation’, *J. Fluid Mech.* **743**, 295-326 (2014)

[51] H. Sakamoto and H. Hainu, ‘A study on vortex shedding from spheres in a uniform flow’, *Trans. ASME J. Fluids Eng.* **112**, 386-392 (1990)

[52] G. E. Bell, ‘On the Impact of a solid sphere with a fluid surface’, *Phil. Mag. J. Sci.* **48**, 753-765 (1924)